August 2004 • NREL/SR-520-36695

Subcontractor Report

Optimization of Phase-Engineered a-Si:H-Based Multijunction Solar Cells

Second Annual Technical Report
January 2003 – January 2004

C.R. Wronski, R.W. Collins, V. Vlahos,
J.M. Pearce, J. Deng, M. Albert, G.M. Ferreira,
and C. Chen
Pennsylvania State University
University Park, Pennsylvania



National Renewable Energy Laboratory
1617 Cole Boulevard, Golden, Colorado 80401-3393
303-275-3000 • www.nrel.gov

Operated for the U.S. Department of Energy
Office of Energy Efficiency and Renewable Energy
by Midwest Research Institute • Battelle

Contract No. DE-AC36-99-GO10337

August 2004 • NREL/SR-520-36695

Optimization of Phase-Engineered a-Si:H-Based Multijunction Solar Cells

Second Annual Technical Report
January 2003 – January 2004

C.R. Wronski, R.W. Collins, V. Vlahos,
J.M. Pearce, J. Deng, M. Albert, G.M. Ferreira,
and C. Chen
Pennsylvania State University
University Park, Pennsylvania

NREL Technical Monitor: Bolko von Roedern

Prepared under Subcontract No. NDJ-2-30630-01



National Renewable Energy Laboratory
1617 Cole Boulevard, Golden, Colorado 80401-3393
303-275-3000 • www.nrel.gov

Operated for the U.S. Department of Energy
Office of Energy Efficiency and Renewable Energy
by Midwest Research Institute • Battelle

Contract No. DE-AC36-99-GO10337

This publication was reproduced from the best available copy submitted by the subcontractor and received no editorial review at NREL

NOTICE

This report was prepared as an account of work sponsored by an agency of the United States government. Neither the United States government nor any agency thereof, nor any of their employees, makes any warranty, express or implied, or assumes any legal liability or responsibility for the accuracy, completeness, or usefulness of any information, apparatus, product, or process disclosed, or represents that its use would not infringe privately owned rights. Reference herein to any specific commercial product, process, or service by trade name, trademark, manufacturer, or otherwise does not necessarily constitute or imply its endorsement, recommendation, or favoring by the United States government or any agency thereof. The views and opinions of authors expressed herein do not necessarily state or reflect those of the United States government or any agency thereof.

Available electronically at http://www.osti.gov/bridge

Available for a processing fee to U.S. Department of Energy and its contractors, in paper, from:

U.S. Department of Energy
Office of Scientific and Technical Information
P.O. Box 62
Oak Ridge, TN 37831-0062
phone: 865.576.8401
fax: 865.576.5728
email: mailto:reports@adonis.osti.gov

Available for sale to the public, in paper, from:

U.S. Department of Commerce
National Technical Information Service
5285 Port Royal Road
Springfield, VA 22161
phone: 800.553.6847
fax: 703.605.6900
email: orders@ntis.fedworld.gov
online ordering: http://www.ntis.gov/ordering.htm



Printed on paper containing at least 50% wastepaper, including 20% postconsumer waste

Table of Contents

1. Executive Summary vii
   - Task 1 vii
   - Task 2 viii
   - Task 3 ix
   - Task 4 xi
2. Task 1 1
   - n-i-p Solar Cell Structures. 1
   - Comparison of vhf and rf PECVD of a-Si:H at High Pressure: ~ 3.3 Å/s 3
   - Comparison of vhf and rf PECVD of a-Si:H at High Pressure: ~ 6.5 Å/s 4
3. Task 2 14
   - Low Power and Pressure Si:H Depositions: Crystalline Si Wafer Substrates 14
   - Low Power and Pressure Si:H Depositions: R=0 a-Si:H Substrates 15
4. Task 3 23
   - Device Loss Mechanisms 23
   - Potential Barriers in i-layers adjacent to the p,n contacts 24
   - Bulk Recombination Limitations on 1-sun V_{OC} 26
   - Limitations on FF 27
   - Thermal Annealing of SW Defects at 25^{o}C after 1 sun Degradation 28
   - Creation of Defect States in i-layers by Recombination of Carriers under Forward Bias 29
   - Voltage-Dependent Differential Diode Quality Factors n(V) 29
5. Task 4 40
   - Novel Analysis of RTSE applied to Amorphous-to-Microcrystalline Phase Transition Region 40
   - Analysis of the Evolution of (a+μc)-Si:H films 40
   - SWE Studies on Thin Films 42
   - Relaxation of Light Induced Changes at 25^{o}C after 1 sun Illumination 45
6. APPENDIX A 56
   - Theoretical Considerations 56
7. List of Publications 63

List of Figures

Figure 1: The J_D-V characteristics for p-a-SiC:H n-i-p cells with different i/p interface regions ...6
Figure 2: J_D-V characteristics of the best protocrystalline p-Si:H and p a-SiC:H cells.....6
Figure 3a: 1 sun light I-V characteristics of p-SiC:H n-i-p solar cells with and without a vacuum break between the deposition of the i- and p-layers.....7
Figure 3b:. 1 sun light I-V characteristics of protocrystalline-p n-i-p solar cells with and without a vacuum break between the deposition of the i- and p-layers.....7
Figure 4: Deposition rate versus H_2-dilution ratio R for Si:H film growth by rf (13.56 Hz) and vhf (60.0 MHz) PECVD under elevated power and high pressure (p = 4.0 Torr) conditions that yield moderate deposition rates (~3.3 Å/s) just below the a→(a+μc) transition (R=60) ...8
Figure 5: Surface roughness layer thickness versus bulk layer thickness for films prepared by rf (13.56MHz) PECVD at low pressure (0.4 Torr) and by rf and vhf (60 MHz) PECVD at high pressure (4 Torr). R was maximized while ensuring a-Si:H deposition throughout the thickness, and the power density was selected for similar rates (2.8 - 3.4 Å/s).....8
Figure 6: Phase diagrams for Si:H film depositions on c-Si substrates at 200°C by rf (13.56 MHz) PECVD under elevated power conditions using low and high total gas pressures, including (P=0.83 W/cm^2, p_{tot}<0.5 Torr) (squares), and (P=0.34 W/cm^2, p_{tot}=4.0 Torr) (circles) 9
Figure 7: Comparison of the deposition rates for vhf (60 MHz) and rf (13.56 MHz) Si:H film growth as a function of R at elevated power and a high pressure of 3 Torr. Power levels are chosen to yield similarly high deposition rates (~6.5 Å/s) just below the a→(a+μc) transition (R=60).....10
Figure 8: Surface roughness layer thickness (d_s) versus bulk layer thickness (d_b) for deposition of a-Si:H films by rf PECVD using H_2-dilution levels of R=15, 20, 40, and 60 at a plasma power of 0.72 W/cm^2 and a total pressure of 3.0 Torr on (native oxide)/c-Si substrates.....10
Figure 9: Surface roughness layer thickness (d_s) versus bulk layer thickness (d_b) for deposition of Si:H films by rf PECVD using H_2-dilution levels of R=70, 80, and 100 at a power level of 0.72 W/cm^2 and a total pressure of 3.0 Torr on (native oxide)/c-Si substrates. 11
Figure 10: Surface roughness layer thickness (d_s) versus bulk layer thickness (d_b) for vhf (60 MHz) PECVD of Si:H films using H_2-dilution levels of R=20, 40, 60, 70, and 80 at a power level of 0.53 W/cm^2 and a total pressure of 3.0 Torr on (native oxide)/c-Si substrates.....11
Figure 11(a): Superimposed phase diagrams for two series of PECVD Si:H films deposited on native oxide covered c-Si substrates using plasma frequencies of 13.56 and 60 MHz, at elevated plasma power levels of 0.72 W/cm^2 (rf) and 0.53 W/cm^2 (vhf) and at 3 Torr total pressure 12
Figure 11(b): Superimposed phase diagrams for two series of PECVD Si:H films deposited on native oxide-covered c-Si substrates.....13
Figure 12: Comparison of the deposition rates for rf (13.56 MHz) and vhf (60 MHz) PECVD as a function of R under low power (0.08 W/cm^2) and low pressure (< 0.5 Torr) conditions.....17
Figure 13: Surface roughness layer thickness (d_s) versus bulk layer thickness (d_b) for growth of single phase amorphous Si:H films by vhf (60.0 MHz) PECVD using H_2-dilution levels of R=0, 2, 6, and 8 in the low power (0.08 mW/cm^2) and low pressure (< 0.5 Torr) process on smooth (nat. oxide)/c-Si substrates 17

Figure 14: Surface roughness layer thickness (d_s) versus bulk layer thickness (d_b) for growth of Si:H films by vhf (60.0 MHz) PECVD using H_2-dilution levels of R=10, 12.5, 15, 20, and 30 in the low power (0.08 mW/cm^2) and low pressure (< 0.5 Torr) process on smooth (nat. oxide)/c-Si substrates....18
Figure 15: Superimposed phase diagrams for two series of PECVD Si:H films deposited on native oxide covered c-Si substrates using rf (13.56 MHz) and vhf (60 MHz) plasma frequencies at low power (0.08 mW/cm^2) and low pressure (< 0.5 Torr)....19
Figure 16: Surface roughness layer thickness versus bulk thickness for a series of R=10 films prepared by rf (13.56 MHz) PECVD at different plasma power levels, and for an R=10 film prepared by vhf (60 MHz) deposition at the lowest plasma power (0.08 W/cm^2)....20
Figure 17(a): The a→a roughening transition thickness as a function of H_2-dilution ratio for three deposition series at low pressure (<0.5 Torr): (i) rf PECVD with minimum plasma power (0.08 W/cm^2, yielding 1.2 Å/s at R=0 and 0.5 Å/s at R=10); (ii) rf PECVD with high plasma power (0.8 W/cm^2; yielding 8.0 Å/s at R=0 and 3.5 Å/s at R=10); and (iii) vhf PECVD with minimum power (0.08 W/cm^2, yielding 3.1 Å/s at R=0 and 1.9 Å/s at R=10)....20
Figure 17(b): Surface roughness layer thickness (d_s) versus bulk layer thickness (d_b) for deposition of Si:H films by vhf (60.0 MHz) PECVD with H_2-dilution levels of R=15, 20, 30, 40 and 60 at low power (0.08 mW/cm^2) and low pressure (< 0.5 Torr) on R=0 a-Si:H substrates....21
Figure 17(c): Simple phase diagrams, including only the a→(a+μc) transition thickness, for vhf (60.0 MHz) PECVD at low power (0.08 mW/cm^2) and low pressure (< 0.5 Torr) on c-Si wafer and R=0 a-Si:H film substrates....21
Figure 17(d): Superimposed phase diagrams comparing Si:H depositions using rf (13.56 MHz; squares) and vhf (60 MHz; circles) plasma excitation on R=0 a-Si:H substrate films....22
Figure 18: J_D-V characteristics for R=10 a-Si:H cells with two different thickness i-layers....33
Figure 19: J_D-V characteristics for R=10 cells with and without a p/i interface layer and the predicted result for a R=10 cell structure in which the p/i recombination is negligible....33
Figure 20: J_D-V characteristics for R=0 cells with and without a p/i interface layer and the predicted result for a R=0 cell structure in which the p/i recombination is negligible
Figure 21: J_D-V characteristics for two p-i-n solar cells having the identical cell structures except one with a-Si:H n-layer and the other with mc-Si:H n-layer....34
Figure 21: J_D-V characteristics for two p-i-n solar cells having the identical cell structures except one with a-Si:H n-layer and the other with mc-Si:H n-layer....34
Figure 22: J_D-V characteristics of p-i-n solar cells having R=0 i-layer with different thickness of 0.4mm, 0.8mm, and 1.5mm, respectively....35
Figure 23: Light induced degradation kinetics of the 1-sun V_{OC} for the cell with 0.4mm thick R=0 i-layer and 200 Å thick R=40 at the p/i interface....35
Figure 24: Variation of fill-factors as illumination levels change for the cells in Figure 1....36
Figure 25: Relaxation in J_D (0.4V) at 25^{o}C and 50^{o}C after 1 sun illumination for 30 minutes at the same temperature....36
Figure 26: J_D-V characteristics of the p-i-n cell with 0.4μm R=10 bulk i-layer and R=40 p/i interface layer at different degradation times obtained through 1-sun illumination as well as equivalent forward bias current....37
Figure 27:. n(V) characteristics of p-i-n cells with 0.4um R=10 i-layers but having different p/I interface layers....37

Figure 28:. n(V) characteristics of p-i-n cells with 0.4 um R=10 i-layer and 200 Å R=40 i-layer but having different n layers 38
Figure 29: n(V) characteristics of p-i-n cells in their annealed state with R=40 p/i interface layer but having different bulk i-layers....38
Figure 30: n(V) characteristics of p-i-n cells in their degraded state with R=40 p/i interface layer but having different bulk i-layers....39
Figure 31: (a) Real and (b) imaginary parts of the dielectric functions of the pure phases for an R=20 Si:H deposition on c-Si. The solid lines are fits using analytical models for the dielectric functions....48
Figure 32: Depth profile in the volume fraction of the microcrystalline phase throughout the mixed-phase (a+μc)-Si:H growth regime for the R=20 Si:H deposition on c-Si from Fig. 27 (points). In order to extract the volume fraction of μc-Si:H, the dielectric function of the top-most growing material was tracked throughout the film deposition....49
Figure 33: (a) Surface roughness thickness versus bulk layer thickness for the R=20 Si:H deposition of Figs. 31 and 32; (b) schematic of the cone growth model used to estimate the microcrystallite nuclei density and cone angle 50
Figure 34: Cone angle □ (top panel) and nucleation density N_d (bottom panel) versus the $a \rightarrow (a+\mu c)$ transition thickness $d_{b,trans}$ for Si:H films deposited under different conditions on both c-Si wafers and R=0 a-Si:H 51
Figure 35: Dual beam photoconductivity (DBP) measurement system used to measure α(E) and μτ products....52
Figure 36: kN(E), hυ*dα/dE, and α(hυ) for an R=10 0.8μm a-Si:H thin film in the annealed state 53
Figure 37: Photocurrent kinetics of degradation for 100 hours and recovery for one hour of an 0.8μm R=10 film at 25°C 53
Figure 38: Normalized photocurrent vs. room temperature relaxation time in minutes for a R=10 film degraded under 1 sun illumination at 25°C for 1minute, 2hours, and 24 hours.....54
Figure 39: Photocurrent normalized to the 1 sun 25˚C degraded state after 2 hours....54
Figure 40: The dark current at 0.4V relaxation at 25°C after 30 minutes of 1sun illumination at 25°C of a p-i-n solar cell with a 200Å R=40 p/i interface and 3,800Å R=10 i-layer on the right axis....55
Figure A.1: Schematic band diagram for i-layer of p-i-n cells under forward bias in the dark.....62
Figure A.2: Schematic band diagram for i-layer of p-i-n cells under forward bias and illumination 62

Executive Summary

The restructuring in the program brought about by the move of co-PI Rob Collins to the University of Toledo is proceeding smoothly. Two of his graduate students are continuing their work at Penn State. One will be graduating in the summer and the other will move to Toledo together with the real time spectroscopic ellipsometry single chamber system. A graduate student is and will continue to work on the RTSE multi-chamber system for in-situ studies on the growth of a-Si:H, a-SiGe:H materials and high performance solar cells. The RTSE multi-chamber is near completion and trial depositions with a-Si:H will begin shortly. Construction of the new Dual Beam Photoconductivity (DBP) apparatus has been completed and the new capabilities are being utilized in studies on a-Si:H thin films.

A new apparatus is being constructed for in-depth studies on the mechanisms limiting the performance of a-Si:H solar cells and the two track studies (cells and films) of SWE. The capabilities include the ability to integrate the cell characteristics including the Q.E., at different temperatures on both p-i-n and n-i-p solar cells. The scope of the work under this subcontract entails investigation of engineering improvements in the performance and stability of solar cells in a *systematic* way. It consists of the following four tasks.

Task 1. Materials research and device development
Task 2. Process improvement directed by real time diagnostics
Task 3. Device loss mechanisms
Task 4. Characterization strategies for advanced materials

Not unexpectedly in the work performed there is extensive overlap among the tasks, but in this report it is summarized using these categories.

Task 1.

In Task 1, we continued to understand and improve n-i-p (substrate) solar cells and address their apparent inherent differences from p-i-n (superstrate) cell structures. The phase diagrams developed using real time spectroscopic ellipsometry (RTSE) to characterize thin film growth and microstructure have been successful in explaining the nature of p-Si:H films doped with BF_3 and guiding the development of high V_{OC} in n-i-p solar cells. The results show that in order to maximize V_{OC}, it is necessary to deposit the p-layers at the maximum R values that allow the desirable thickness to be obtained without crossing the transition into the mixed-phase growth regime.

The possible mechanisms responsible for the differences in 1 sun V_{OC} obtained with the different p-Si:H layers were explored. Carrier recombination in cell structures was characterized with J_D-V measurements, and the recombination in their p/i and i/p interface regions was identified and quantified. The systematic studies clearly established that the lowest p/i interface recombination is obtained with *protocrystalline a-Si:H* and not with layers containing any *microcrystalline* phase (whose V_{OC} is also significantly lower than that achieved with the optimum a-SiC:H structure). The significantly lower i/p interface recombination in the

protocrystalline p-Si:H cells is attributed in large part to the subsurface modification of the intrinsic layer during the deposition of the p-contact. Evidence is found that the high concentrations of atomic hydrogen present during the deposition of the protocrystalline p-Si:H layer are responsible for this beneficial effect. In addition, unlike a-SiC:H, it allows the protocrystalline p-layer to be used in fabricating solar cell structures without any adverse effect of exposing the i-layers to air.

The optimization of rf and vhf PECVD materials for high rate i-layers of Si:H solar cells based on the deposition phase diagram was also investigated. It is found that under H_2 deficient dilution conditions, vhf (60 MHz) PECVD provides significant advantages over rf (13.56 MHz) PECVD in the fabrication of higher quality a-Si:H at high rates. Under optimum conditions, however, with the H_2-dilution ratio set just below the a→(a+μc) transition for the desired film thickness, vhf PECVD provides no significant advantage over rf PECVD when identical high deposition rates are compared. It was also found that in a high plasma power, high pressure (3 Torr) rf PECVD process for a-Si:H film growth, the amorphous phase roughening transition thickness remains above 1000 Å just below the a→(a+μc) boundary where the rate is 6.5 Å/s. This transition thickness is a factor of two higher than that observed under low pressure deposition conditions with almost a factor of two lower deposition rate for the a-Si:H. In fact, three manifestations of enhanced precursor surface diffusion are found with increasing H_2-dilution ratio R under all conditions of a-Si:H deposition explored: (i) increased surface smoothening (both rate and amplitude) associated with the coalescence of initial nuclei in the first 100 Å of deposition; (ii) reduced surface roughness layer thickness at the stable surface value; and (iii) increased surface stability as measured by the thickness of the a→a roughening transition. The presence of all three effects provide clear signatures of improved-device quality materials based on the monolayer level processes detected at the film surface. As a result, we can conclude that the appropriate combination of high R [at the a→(a+μc) transition for the desired film thickness], high power, and high pressure give rise to reasonable device performance at rates > 6 Å/s, without resorting to unconventional deposition methods.

Task 2.

In Task 2, we continued to apply real time spectroscopic ellipsometry to develop deposition phase diagrams for guiding the fabrication of hydrogenated silicon (Si:H) thin films at low temperatures (<300°C) for high performance solar cells. Phase diagrams have been extended to include the thickness at which a roughening transition is detected in the amorphous film growth regime. The three surface microstructural and phase transitions, including the a→a roughening transition, the a→(a+μc) roughening transition, and the (a+μc)→μc smoothening transition have been incorporated into an extended deposition phase diagram. Correlations of such phase diagrams for intrinsic Si:H layers with the corresponding electronic properties and p-i-n device performance demonstrate that the optimum i-layers are obtained at the maximum possible R value for the desired thickness without crossing the a→(a+μc) boundary of the phase diagram into the mixed-phase growth regime. Because the R value at this phase boundary depends on both the nature of the substrate and the i-layer thickness, these aspects of the materials or device structure must be specified in order to identify the optimum conditions for i-layers deposited on amorphous film substrates (such as the p or n-layers of p-i-n or n-i-p solar cells). The optimum a-Si:H i-layer material has been described as *protocrystallin*e Si:H which ultimately evolves into

(a+μc)-Si:H if the film is allowed to grow beyond the desired thickness for which the deposition process was optimized.

Because the a→(a+μc) transition decreases in thickness with increasing R, two-step and even multi-step i-layer processes can be designed on the basis of the phase diagram in order to optimize solar cells. Optimization of rf and vhf PECVD materials for high rate i-layers of a-Si:H solar cells based on the deposition phase diagram have been further explored. The similarities of the phase diagrams for both rf and vhf PECVD of Si:H on R=0 a-Si:H substrate films demonstrate that the two-step optimization procedure developed for the rf PECVD protocrystalline i-layers of a-Si:H-based p-i-n and n-i-p cells would also apply for vhf PECVD i-layers as well.

Task 3.

The work carried out under Task 3 continued to address the mechanisms and defects determining a-Si:H solar cell characteristics that have not yet been clearly resolved. The studies on a-Si:H based solar cells have been further refined with analysis using a theoretical treatment based on first principles. This treatment takes into account: (i) Shockley-Reed-Hall diffusion/recombination of injected carriers in the bulk and at the p/i interface; (ii) the drift driven transport of photogenerated carriers; (iii) the homogeneous densities of defects across the i-layers with continuous distributions of states in the gap; and (iv) potential barriers V_n, V_p due to the high concentration of carriers at the n, p contacts. The results on a wide variety of solar cell structures have been interpreted self-consistently with this model, described in Appendix A, thus allowing solar cell operation to be addressed systematically and a number of misconceptions to be rectified. In obtaining reproducible results for the J_D-V characteristics the contribution of external contact resistance was taken into account by using a three-probe technique for measuring the currents. In addition the measurements were carried out using a thermoelectric heating/cooling stage with which the temperature of the samples could be controlled to within 0.1^oC.

It is found that distinctly different regimes in the dark forward bias current-voltage, J_D-V, characteristics in "state-of-the-art" a-Si:H cells offer novel powerful probes, not only for investigating these mechanisms, but also for characterizing the defect states in intrinsic a-Si:H materials when the i-layers, p/i interface regions, and p, n contacts are changed in systematic and controlled ways. The dependence of the bulk recombination currents on the thickness and densities of defects in the i-layers has been established. It is found that the "effective diode quality factors" of these currents do not exhibit a constant n, as has been generally considered. The characteristics exhibit voltage dependent "differential diode quality factor" n(V) equal to the inverse of $[kT/q][d(\ln J_D)/dV]$. This result is consistent with the model that predicts such n(V) values as a consequence of a continuous distribution of the states in the gap. The changes in the n(V) characteristics expected from the introduction of light induced defects and from differences in i-layer materials have also been observed, and the analysis of these J_D-V characteristics has been undertaken.

The magnitudes of the currents corresponding to the recombination at the p/i interfaces have been directly correlated with the nature of these regions. Their n(V) characteristics are as predicted by the model, independent of voltage with values very close to one. The systematic decreases of p/i recombination have allowed, for the first time, observation of the direct

dependence of 1 sun V_{OC} on the thickness of the i-layers. The nature of the limitations on the carrier injection over the potential barriers V_n, V_p and their effects on the 1 sun fill factors have been explored and found to be consistent with the predictions of the model.

The transport and recombination of carriers generated by illumination in the i-layers was also investigated. Superposition between J_{SC}-V_{OC} and J_D-V characteristics is obtained over a wide range of currents and voltages. These results, as well as the nature of the separations obtained at voltages approaching 1 sun $V_{OC,}$ are together consistent with the recombination of carriers and the contributions of V_n, V_p predicted by the model. Such potential barriers can have a large effect on carrier transport at voltages approaching 1 sun V_{OC} and hence the FF, even though the barriers are much smaller than those commonly postulated as being due to large densities of defects.

In the last quarter of this phase the differential diode quality factors, n(V), extracted from the J_D-V characteristics from the wide range of a-Si:H solar cell structures studied, were investigated. The contributions of recombination in the bulk of the i-layers and p/i interface regions as well as the carrier injection have been clearly identified and related to the model in Appendix A. The n(V) characteristics obtained for bulk recombination clearly illustrate the potential for characterizing the defect state distributions in the a-Si:H layers, and their difference in the annealed states of the R=10 and R=0 materials was directly and reliably identified. The n(V) characteristics were also applied in the studies on the creation of 1 sun light induced defects and the energy distribution of their gap states to results on both materials. Again distinct differences in the distributions can be clearly identified.

The n(V) spectra for the bulk i-layers of R=10 and R=0 materials in the annealed state were identified from results such as just described, as well as from those on cells with different i-layer thickness. These results are consistent with the model discussed in Appendix A. As predicted the values of n are between 1 and 2 which are different for the R=10 and R=0 layers. However a striking feature of these n(V) spectra is that they are distinctly different as is expected for different distributions of gap states in these materials. Although more complex analysis is needed, they clearly indicate that in the R=0 material the distribution near midgap is broader than in the R=10. Characterizing the n(V) spectra after the introduction of light induced defects in the i-layer materials not only changes both of these spectra but also shows that the densities of state distributions in the R=10 and R=0 materials are also distinctly different.

In the course of the studies on the light induced changes of the i-layers a new phenomenon in SWE was observed – **the thermal relaxation of defect states at 25^{0}C created by 1 sun illumination**. This relaxation which is readily observed at low forward biases exhibits a very large dependence on the voltage at which it is characterized. This clearly shows that it is due to the states located close to the midgap. Large decreases in this relaxation are also observed when the quasi-Fermi splitting and thus carrier recombination, are increased with higher bias, and are erased at values which occur under 1 sun illumination. In addition it is found that, as expected, it changes with temperature but in a way that cannot be readily characterized by any simple activation energy. The results, which have initiated *careful* studies on corresponding films and discussed in Task 4, confirm this relaxation which gives a new wrinkle to SWE whose effects have not been recognized in either room temperature studies or the models for creation of SW defects.

Because of the developed ability to characterize the defect states in the i-layers of solar cells, the potential of using the recombination under far forward bias to generate defects in studies of SWE was investigated. It was found that in cell structures, where the recombination in

the p/i interface regions is very much less than that in the bulk, equivalence is present in the kinetics of the changes in the J_D-V characteristics under 1 sun illumination and those for far forward bias currents equal to J_{SC}. Such a method of creating SW defects is now also being used, adding flexibility to the conditions for the creation, annealing and relaxation of their defect studies.

Task 4.

In Task 4, work was carried out to identify and quantify the development of crystallinity across the amorphous-to-microcrystalline transition from the evolution of the optical properties during growth. Quantification of the crystalline Si fraction from the evolution of the RTSE data collected during growth across the amorphous-to-[mixed-phase (amorphous+microcrystalline)] boundary requires a new analysis method, since the conventional two layer model (bulk/roughness) used to analyze uniform a-Si:H films is no longer correct once the film traverses this boundary. A self-consistent method based on a virtual interface approach was develop to interpret the RTSE measurements for Si:H films that undergo the a→(a+μc) transition. This method provides the continuous evolution of the μc-Si:H volume fraction ($f_{\mu c}$), and hence the depth profile of $f_{\mu c}$, along with the evolution of the surface roughness layer thickness (d_s) in the mixed phase (a+μc)-Si:H regime. In addition, the optical properties of the Si:H film in the a-Si:H, mixed phase (a+μc)-Si:H, and single phase μc-Si:H regimes can be deduced in the new analysis method. Finally, the depth profile in $f_{\mu c}$ can provide basic geometrical information on the mixed-phase microcrystalline (a+μc)-Si:H growth regime including the nucleation density and cone angle characterizing the evolution of the Si microcrystallites. In fact, the geometric information correlates well with that from ex situ structural and device performance studies. This new and powerful RTSE analysis method allows one to identify and quantify the microstructure of "microcrystalline/ nanocrystalline" solar cells in order to understand the mechanisms limiting their performance.

In the SWE studies on thin films a new approach was developed for the interpretation of subgap absorption, α(hυ), by addressing the contributions of multiple defects with the analysis of the entire spectra rather than just their magnitude. In the interpretation account is taken of α(hυ) being determined by N(E), the densities of electron occupied states and **not** the total defect density, N_{def}. Despite the complexities, information can be obtained about the light induced defect states from $kN(E) = (h\upsilon)d[\alpha(h\upsilon)]/dE - \alpha(h\upsilon)$,where k is related to the matrix elements for transitions from the localized to extended states. The evolution of the light-induced defect states has been characterized by normalizing kN(E) after degradation, $N_{DS}(E)$, to that in the annealed state, $N_{AS}(E)$, which gives $P(E) = kN_{DS}(E)/kN_{AS}(E)$. Such P(E) spectra provided a clear fingerprint of where the largest changes occur in the electron occupied states. P(E) spectra were obtained which for the *first time* identified two distinctly different light induced gap states at and below midgap. They also showed that the kinetics of their evolution was not only different but also dependent on the microstructure of the a-Si:H material. A clearer picture in the evolution in the different gap states is being developed from $Z(E) = k[N_{DS}(E)-N_{AS}(E)]$ which is a more direct method of evaluating the actual increases in the densities of the electron occupied states. However to characterize Z(E) in any meaningful way it is critical to obtain α(E) spectra with both high accuracy and spectral resolution. Both of these have been achieved with the new DBP

measurement apparatus and Z(E) spectra are being investigated on both diluted and undiluted a-Si:H thin films.

The presence of the thermal annealing of light induced defect states at room temperature after 1 sun illumination discovered in the studies on solar cells, triggered a corresponding careful study on a-Si:H thin films. Results were obtained on the kinetics of photocurrent recoveries, which are in excellent agreement with those on cells. These results represent the first direct observation of such room temperature annealing in thin films of a-Si:H. They also further confirm the ability to directly correlate results on cells with those on films. The kinetics of this relaxation are found to depend on the "history" of the 1 sun exposure. It is also found that the relaxation can be very rapidly erased with illuminations much smaller than 1 sun, where the results are in agreement with earlier results that defect states created faster also anneal out faster. This newly discovered relaxation in the light induced defect states located near midgap in thin films has important implications not only in understanding the nature of these states but also on the results reported in the extensive studies carried out on SWE at 25^{o}C. In the α(E) studies being carried out on the light induced defects, room temperature relaxation in the light induced changes has been taken into account. This and other studies on light induced defects are being carried out in close collaboration with the University of Utah. Results have been obtained where this annealing out of defects is observed and is being carefully investigated.

Task 1

n-i-p Solar Cell Structures.

The mechanisms responsible for the differences in the 1 sun open circuit voltage (V_{OC}) values reported for n-i-p cells having p-a-SiC:H and highly diluted p-Si:H layers[2,3] have been investigated. In the work on n-i-p solar cells having identical bulk intrinsic layers with both p-a-SiC:H and highly diluted p-Si:H layers the contributions of p/i interface recombination to their J_D-V characteristics were clearly identified and quantified. Results were obtained on cell structures having identical i-layers where the recombination in the p/i interface regions was quantified and their limitation on 1 sun V_{OC} identified for the p-a-SiC:H and protocrystalline p-a-Si:H contacts. It is found that the lowest p/i interface recombination is obtained with *protocrystalline* and not *microcrystalline* layers which lead to the highest 1 sun V_{OC}. The systematic changes of recombination obtained with the different p-a-Si:H layers are discussed in terms of their properties as well as those of the corresponding p/i interface region. Evidence was also found for the importance of the subsurface modification in the intrinsic layer due to the high hydrogen dilution and power used in depositing the p-layers.

The n-i-p structures in this study were deposited by plasma enhanced chemical vapor deposition (PECVD) at substrate temperatures of 200^{o}C with bulk R=10 intrinsic layers under conditions previously described[1]. The p-a-SiC:H cell structures consisted of glass / Cr / n a-Si:H (350 Å) / i a-Si:H (4000 Å) / p-a-SiC:H (250 Å) / ITO, where the p-layer was deposited with a constant doping ratio D=[$B(CH_3)_3$]/[SiH_4]=0.005 and with Z=[CH_4]/{[SiH_4]+[CH_4]}= 0.5. A two-step i-layer process utilized in these structures to change the p/i interface region in a controlled way was obtained by terminating the last 200 Å of the i-layer with R values of 0 and 40. The p-Si:H cell structures consisted of glass / Cr / n μc-Si:H (350 Å) / i a-Si:H (4000 Å) / p-Si:H (~200Å) / ITO, where the p-layers were deposited with R varying from 100 to 200, and with a doping ratio D=[BF_3]/[H_2]=0.2. The ITO top contact layers were sputter-deposited at 170^{o}C. The structures tested had areas of 0.02 cm^2 for the p-a-SiC:H and 0.05cm^2 for the p-Si:H cells. The cells were characterized using J_D-V as well as light I-V measurements under 1 sun illumination conditions. Both of these measurements were performed at 25^{o}C using a four-point probe technique in order to eliminate any extraneous series resistance effects which then allow the J_D-V characteristics to be accurately characterized at high forward bias.

In the n-i-p solar cell structures with different p/i interfaces, but identical p- and bulk i-layers, the respective contributions to carrier recombination could be identified and quantified from their J_D-V characteristics. The beneficial effects of incorporating a thin protocrystalline region prior to the deposition of the a-SiC:H p-layer is in agreement with the results reported for p-i-n structures[2]. Fig. 1 shows the forward J_D-V characteristics of two a-SiC:H n-i-p structures with different p/i interface regions, where the recombination at the p/i interface can be identified. The bandgaps (α_{2000}) of the R=10 and R=40 p/i interface regions incorporated in these cells are 1.86 and 1.95 eV respectively.

---

[1] R.J. Koval, C. Chen, G.M. Ferreira, A.S. Ferlauto, J.M. Pearce, P.I. Rovira, C.R. Wronski and R.W. Collins, *Mater. Res. Soc. Proc.* **715**, A6.1 (2002).

[2] J. Koh, Y. Lee, H. Fujiwara, C.R. Wronski and R.W. Collins, *Appl. Phys. Lett,* **73**, 1526 (1998).

From the two regimes in the J_D-V characteristics in Fig. 1 the carrier recombination in forward bias currents that occurs in the bulk and at the p/i interface can be clearly separated as in the case of corresponding p-i-n cell structures[3,4]. At the lower voltages there is a diode quality factor of m=1.4 which then decreases to values closer to 1 at the higher voltages. The regimes where m=1.4 correspond to bulk recombination and as expected there is overlap in the currents over an extended voltage region. As the p/i interface is improved by introducing the R=40 p/i layer, the bulk recombination regime extends to a higher bias and the currents corresponding to the p/i interface recombination become lower. The key role played by this recombination in the p/i interface regions in determining the 1 sun V_{OC} is reflected in their systematic decrease as R at the p/i interface is increased from 0 to 10 to 40 the corresponding 1 sun V_{OC} increases from 0.86 to 0.90 to 0.92 V.

Insight into the carrier recombination that may be limiting these 1 sun V_{OC} values was obtained from the J_D-V characteristics of the different cell structures where the lowest p/i recombination was obtained with the optimized protocrystalline p-Si:H layers which consequently gave the highest 1 sun $V_{OC.}$ The low recombination that is obtained at the p/i interface with the R=150 protocrystalline p-layer is significantly smaller than that for the R=40 buffer layer in the a-SiC:H n-i-p cells which was the lowest achieved for those cells. This is illustrated in Fig. 2 which shows the J_D-V characteristics between 0.6 and 1.0 V, where also as a consequence of this low p/i interface recombination in the protocrystalline p-Si:H cell the bulk recombination regime extends to higher voltages. It also explains why the 1 sun V_{OC} increases from 0.92 to 0.96 V and suggests that in the latter case it could now actually be limited by bulk recombination in the i-layer. In comparing the recombination at the p/i interfaces in these two cell structures it is important to note the difference in the way they are formed. In the case of the a-SiC:H cell the top 200 Å of the i-layer is modified by increasing R from and subsequently depositing the p-layer. The deposition conditions under which the protocrystalline p-layer is grown are such that there are modifications in the subsurface region of the i-layer as discussed earlier. These are attributed to the very large concentrations of atomic hydrogen which is generated by the very high R and power levels utilized for the deposition of the p-layer. A consequence of such concentration of atomic hydrogen is that the p/i interface region become far less sensitive to the presence of a barrier layer on the intrinsic a-Si:H than in the case of n-i-p a-SiC:H cell structures. This is illustrated in Fig. 3 where the light I-V characteristics are shown for the two types of cells with and without exposure of the i-layer to air for 24 hours before the p-layer deposition. It can be seen in Fig. 3a that the air exposure introduced to the p-a-SiC:H n-i-p cell has a drastic effect on its performance by significantly lowering the V_{OC} and FF values as compared to an identical cell completed without an air-gap. Exposure of the sensitive p/i interface region to air leads to the formation of a thin native oxide whose effect is *not* eliminated by the subsequent deposition of a-SiC:H . On the other hand, virtually the same p/i interface regions are obtained in the protocrystalline cells with and without the exposure to air as is indicated by the identical light I-V characteristics, as shown in Fig. 3b.

---

[3] J. Deng, J.M. Pearce, V. Vlahos, R.W. Collins and C.R. Wronski, *Mater. Res. Soc. Proc.* **762**, A3.4.1 (2003).

[4] J. Deng, J.M. Pearce, R.J. Koval, V. Vlahos, R.W. Collins and C.R. Wronski, *Appl. Phys. Lett.* **82**, 3023 (2003).

Comparison of vhf and rf PECVD of a-Si:H at High Pressure: ~ 3.3 Å/s

It is generally recognized that although the highest quality materials can be prepared by rf PECVD at very low rates (0.5 Å/s) by combining the lowest possible power with low gas pressure (<0.5 Torr), this process fails to provide high quality materials at higher rate simply by elevating the plasma power. At the lowest power, ion bombardment may exert a beneficial influence by promoting dehydrogenation reactions within the top monolayer of the growing surface. At higher power levels, energetic bombardment is likely to cause damage to the near-surface region of the film below the topmost monolayer which is then frozen in as the film accumulates. A straightforward approach to eliminate this damage is to operate the deposition at higher pressures. Operation of the plasma at higher pressures is also known to shift the a→(a+μc) transition to high R values presumably due to the depletion of atomic H from the plasma via reaction with SiH_4. Figure 4 shows the deposition rate as a function of R for rf and vhf PECVD of Si:H under conditions of elevated power (rf: 0.34 W/cm^2; vhf: 0.53 W/cm^2) and high pressure (fixed at 4 Torr), leading to moderate deposition rates (~3.3 Å/s) just below the a→(a+μc) boundary for a thick film. Results are shown for rf PECVD with R spanning from 10 to 80, and for vhf PECVD with R spanning a narrower range from 40 to 80, since vhf PECVD at 4 Torr exhibited a narrower range of plasma stability. Figure 5 shows the microstructural evolution of three Si:H films prepared at moderates rates (2.8-3.4 Å/s) just below the a→(a+μc) transition for a thick layer. The two moderate rate a-Si:H films that exhibit the largest a→a roughening transition thickness, ~ 3000 Å, and hence the highest quality, are those prepared under high pressure conditions (4 Torr), including both rf and vhf depositions. In contrast, the film with the poorer surface stability with an a→a transition of ~1500 Å -- in spite of the fact that its rate is somewhat lower than those of the high pressure depositions -- is the one prepared under low pressure conditions (0.4 Torr) by rf PECVD. The lower rate may be a factor in this case (and thus the ~1500 Å transition is an optimistic upper limit) since the a→a roughening transition shifts rapidly to lower thickness with increasing rate under low pressure conditions (see Fig. 6). The apparent small improvement in vhf vs. rf for the two high pressure depositions may also be attributed at least in part to its lower rate.

Figure 6 summarizes the conclusions associated with Fig. 5 through a depiction of phase diagrams for low pressure and high pressure depositions that lead to 3.2-3.5 Å/s rates at an R value just below the a→(a+μc) transition for a thick layer. Most of the results here are from rf depositions presented in earlier reports. The poor plasma stability at 4 Torr for vhf PECVD has prevented the collection of an extensive data set in this case. However, the available data (triangles) suggest similar results for both rf and vhf at high pressures and at optimized R values just below the a→(a+μc) transition for a thick layer (R=60). Thus, in the depositions performed thus far, including those at low rates and low pressures as well as moderate rates and high pressures, *there is no significant advantage in adopting vhf PECVD over rf PECVD when optimum R values are employed for both.*

Comparison of vhf and rf PECVD of a-Si:H at High Pressure: ~ 6.5 Å/s

In order to explore further the final conclusion of the previous section, we employ rf and vhf conditions that (i) yield essentially identical deposition rates just below the a→(a+μc) transition for a thick film and (ii) provide higher vhf plasma stability, in particular lower pressure conditions. Thus, a third comparison of rf and vhf depositions was performed in which the deposition rate was fixed at 6.5 Å/s just below the a→(a+μc) transition for a thick film.

Figure 7 shows the deposition rates as a function of the H_2-dilution ratio for rf and vhf depositions at high pressure (3 Torr) and elevated power levels (rf: 0.72 W/cm^2; vhf: 0.53 W/cm^2) selected for a deposition rate of 6.5 Å/s just below the a→(a+μc) transition for a thick film.

Figure 8 shows the microstructural evolution, specifically the surface roughness layer thickness (d_s) versus the bulk layer thickness (d_b) for the growth of rf (13.56 MHz) PECVD Si:H films that remain amorphous throughout the bulk thickness evolution. These films were prepared using different hydrogen dilution levels (R=15, 20, 40, and 60) at high power (0.72 W/cm^2) and pressure (3 Torr) on native oxide-covered c-Si substrates. As shown in Fig. 7, the deposition rates for these films range from 18 Å/s at R=15 to 6.5 Å/s for R=60, just below the a→(a+μc) transition. In this figure, the three manifestations of improved material quality are clearly evident with increasing R: (i) increased surface smoothening (both rates and amplitudes) associated with the coalescence of initial nuclei in the first 100 Å of deposition; (ii) reduced surface roughness layer thickness at the stable surface value; and (iii) increased thickness of the a→a roughening transition.

Figure 9 shows the microstructural evolution of rf PECVD Si:H films deposited using H_2-dilution levels of R= 70, 80, and 100 under otherwise identical conditions as those in Fig. 8. Each of these films crosses the a→(a+μc) transition during the growth, at a transition thickness that decreases with increasing R. Only the deposition with R=100 also crosses the (a+μc)→μc transition during growth, at a thickness of ~700 Å in this case.

The combined results are summarized in Fig. 10 for the microstructural evolution during Si:H film growth by vhf PECVD using H_2-dilution ratios R=20, 40, 60, 70, and 80 at elevated plasma power (0.53 W/cm^2) and 3 Torr pressure. In this case, similar trends occur as in the case of rf, but in Fig. 10 it is important to distinguish the a→a roughening transitions that occur for R≤60 from the a→(a+μc) transitions that occur for R≥70. As usual, this can be done on the basis of the optical functions which are deduced for the Si:H film at the end of the deposition.

Figure 11(a) shows the superimposed phase diagrams comparing the rf (13.56 MHz) and vhf (60 MHz) processes that yield identical deposition rates of 6.5 Å/s at R=60 just below the a→(a+μc) transition (see Fig. 7). The key conclusion of these two sets of depositions is the observation that both rf and vhf PECVD a-Si:H films exhibit identical a→a roughening transition thicknesses at the optimum R value of 60 just before the a→(a+μc) transition. On the basis of this observation, we can conclude that both R=60 depositions exhibit similar material quality, and that vhf PECVD provides no significant

advantage over rf PECVD when high rate deposition conditions are optimized and identical deposition rates are compared.

In addition to this key conclusion, additional characteristics are evident in Fig. 11(a) that are consistent with previous observations. First, at the lowest value of R (R=20) accessible to vhf PECVD, the a→a roughening transition thickness for vhf deposition is significantly higher than that for rf deposition, suggesting that under non-optimal conditions, in particular insufficient H_2-dilution level, the vhf process does provide an improvement over the corresponding rf process. This conclusion was also reached in consideration of the low power, low pressure rf-vhf deposition comparison. Second, at the highest value of R (R=80) accessible to vhf PECVD, the a→(a+μc) occurs at a lower thickness for vhf PECVD than for rf suggesting a more rapid development of stress-induced crystallinity. Although such observations were noted earlier in comparing vhf and rf processes at low power and low pressure, the differences were not found to be of significance for devices. In particular when R=0 a-Si:H substrates are used, such differences tend to be suppressed or eliminated. Finally, it is of interest to compare the deposition phase diagrams for the two rf deposition processes at high pressure, one yielding a rate of 3.4 Å/s just before the a→(a+μc) transition, and the other yielding a rate of 6.5 Å/s under the corresponding conditions. These results are shown in Fig. 11(b) wherein the lower rate is obtained with power and pressure values of 0.34 W/cm^2 and 4 Torr and the higher rate is obtained with corresponding values of 0.72 W/cm^2 and 3 Torr. Two key observations are evident here that are consistent with many previous investigations. First and most importantly, the entire a→a roughening transition thickness is shifted to decreasing thickness at the higher rate, a trend that clearly reveals deteriorating material properties with increasing deposition rates. However, the a→a roughening transition thickness just below the a→(a+μc) boundary remains above 1000 Å, which is still a factor of two higher than that observed under the low pressure deposition conditions with almost a factor of two lower rate. As a result, we suggest that the high power, high pressure conditions may give rise to reasonable device performance at rates > 6 Å/s, without resorting to unconventional deposition methods.

In future work, these strategies in rf PECVD will be applied in the fabrication of p-i-n and n-i-p solar cell devices with i-layers prepared first at 3 Å/s and then at 6 Å/s. In addition, the strategies will be considered for possible application in higher rate amorphous silicon-germanium deposition. Currently, we are setting up the gas lines for the fabrication of these alloys.

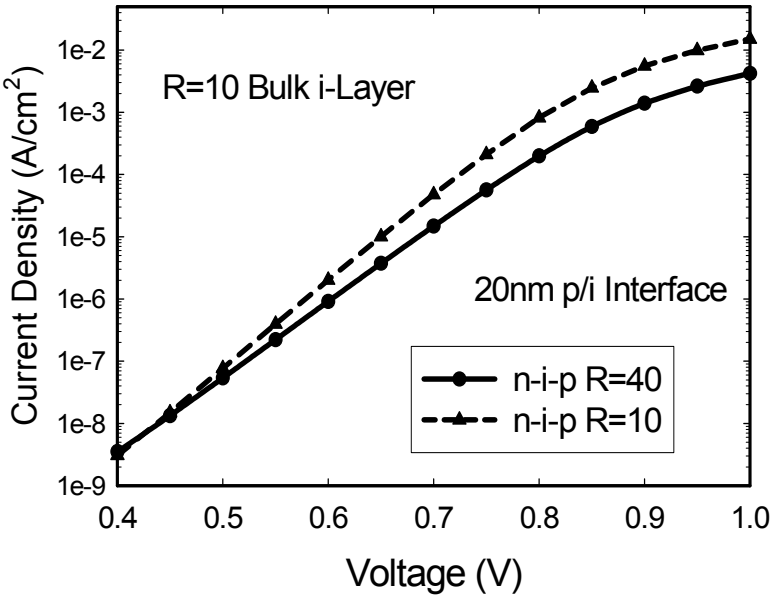


Figure 1: The J_D-V characteristics for p-a-SiC:H n-i-p cells with different i/p interface regions.

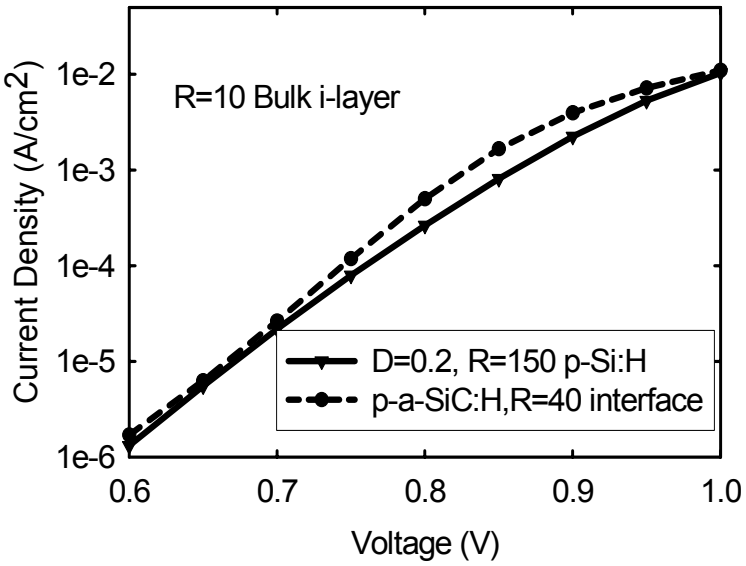


Figure 2: J_D-V characteristics of the best protocrystalline p-Si:H and p a-SiC:H cells.

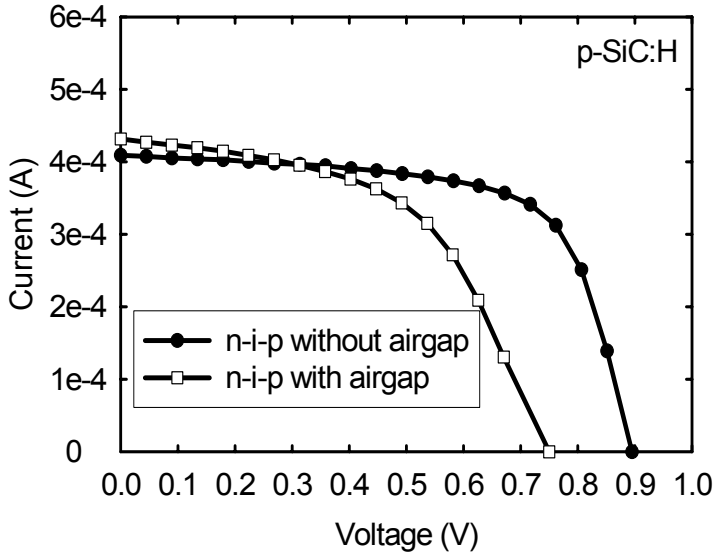


Figure 3a: 1 sun light I-V characteristics of p-SiC:H n-i-p solar cells with and without a vacuum break between the deposition of the i- and p-layers.

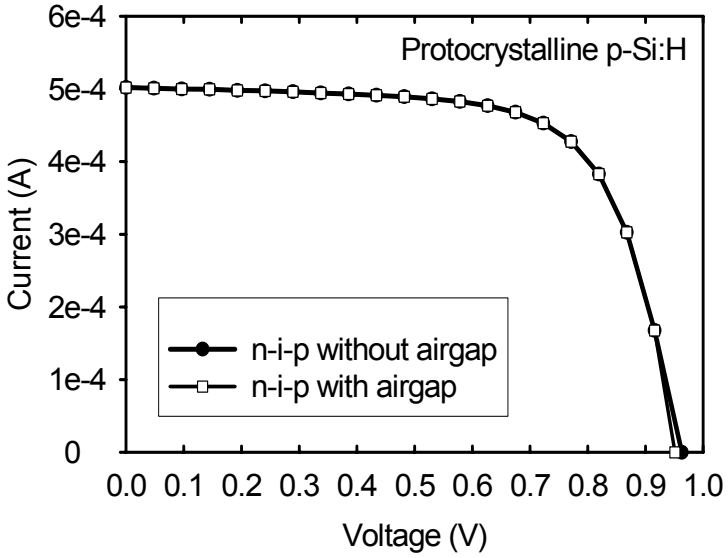


Figure 3b: 1 sun light I-V characteristics of protocrystalline-p n-i-p solar cells with and without a vacuum break between the deposition of the i- and p-layers.

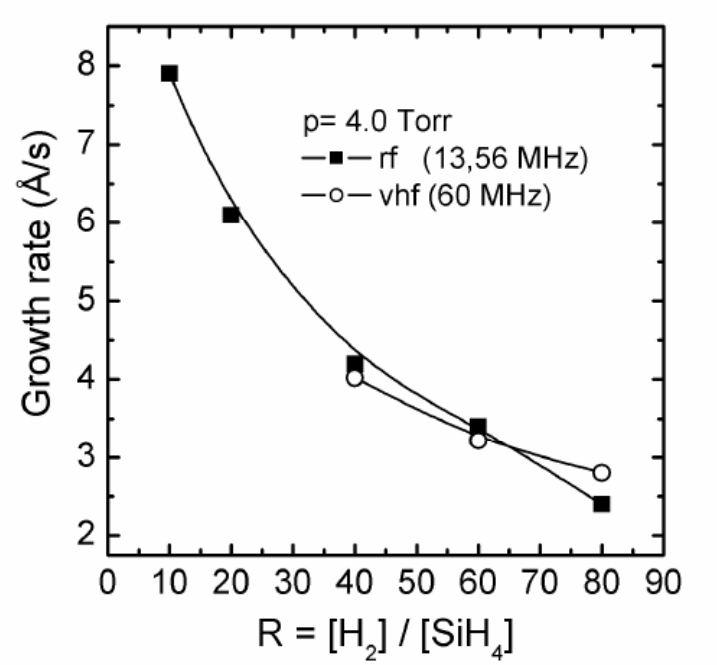


Figure 4: Deposition rate versus H_2-dilution ratio R for Si:H film growth by rf (13.56 Hz) and vhf (60.0 MHz) PECVD under elevated power and high pressure (p = 4.0 Torr) conditions that yield moderate deposition rates (~3.3 Å/s) just below the a→(a+μc) transition (R=60).

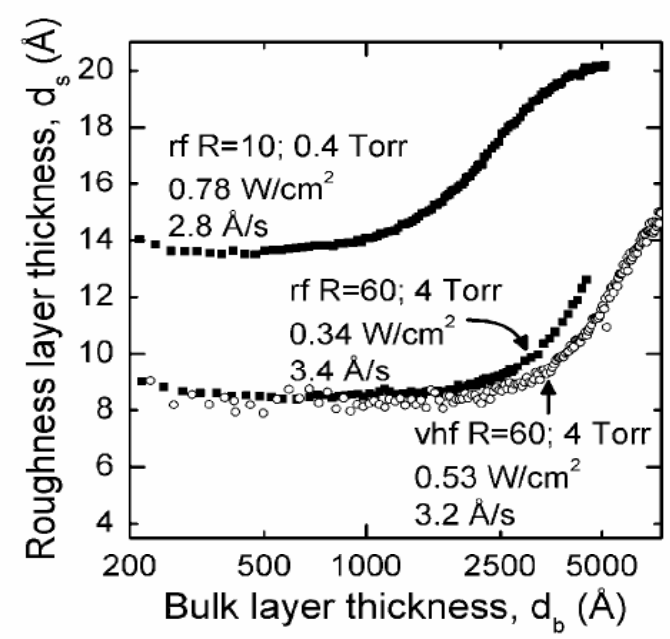


Figure 5: Surface roughness layer thickness versus bulk layer thickness for films prepared by rf (13.56MHz) PECVD at low pressure (0.4 Torr) and by rf and vhf (60 MHz) PECVD at high pressure (4 Torr). R was maximized while ensuring a-Si:H deposition throughout the thickness, and the power density was selected for similar rates (2.8 - 3.4 Å/s).

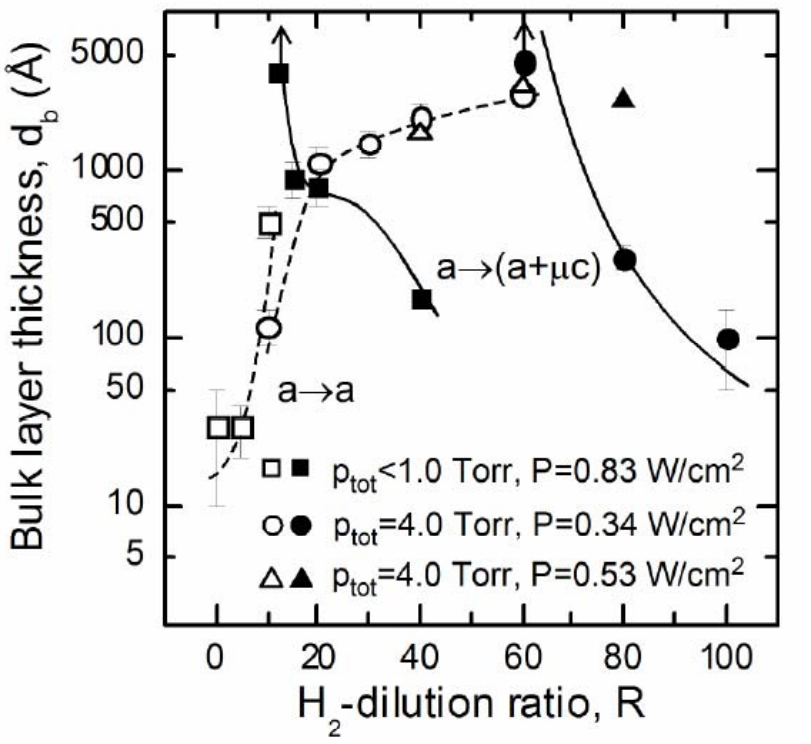


Figure 6: Phase diagrams for Si:H film depositions on c-Si substrates at 200°C by rf (13.56 MHz) PECVD under elevated power conditions using low and high total gas pressures, including (P=0.83 W/cm^2, p_{tot}<0.5 Torr) (squares), and (P=0.34 W/cm^2, p_{tot}=4.0 Torr) (circles). The open symbols and broken lines indicate a→a transitions and the closed symbols and solid lines indicate a→(a+μc) transitions. The points indicated by **triangles** represent results obtained by **vhf** (60 MHz) **PECVD** under elevated power and high pressure conditions (P=0.53 W/cm^2, p_{tot}=4.0 Torr) over a narrower range of R where the plasma is stable. The up arrows indicate that the transition occurs above the identified thickness values.

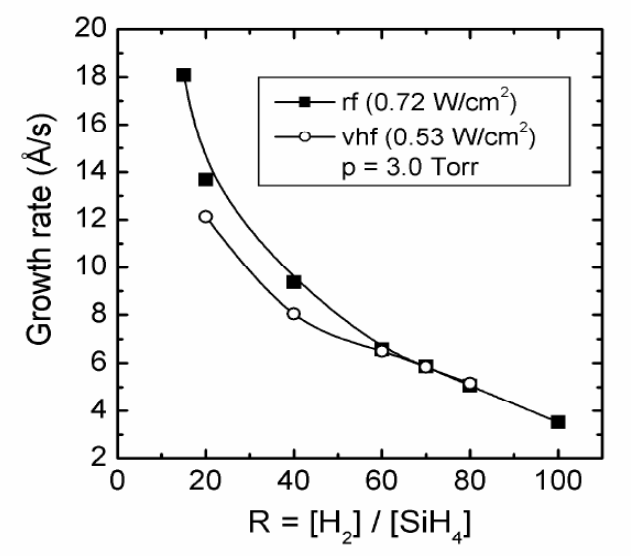


Figure 7: Comparison of the deposition rates for vhf (60 MHz) and rf (13.56 MHz) Si:H film growth as a function of R at elevated power and a high pressure of 3 Torr. Power levels are chosen to yield similarly high deposition rates (~6.5 Å/s) just below the a→(a+μc) transition (R=60).

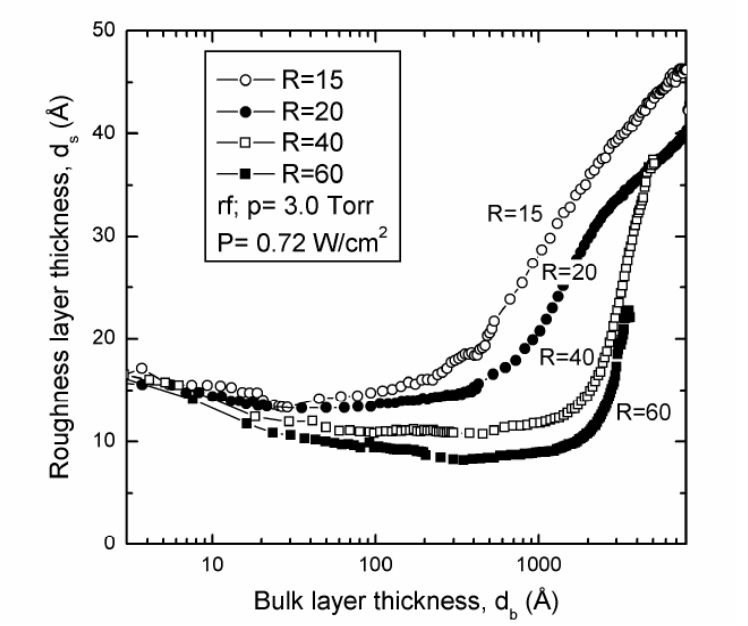


Figure 8: Surface roughness layer thickness (d_s) versus bulk layer thickness (d_b) for deposition of a-Si:H films by rf PECVD using H_2-dilution levels of R=15, 20, 40, and 60 at a plasma power of 0.72 W/cm^2 and a total pressure of 3.0 Torr on (native oxide)/c-Si substrates.

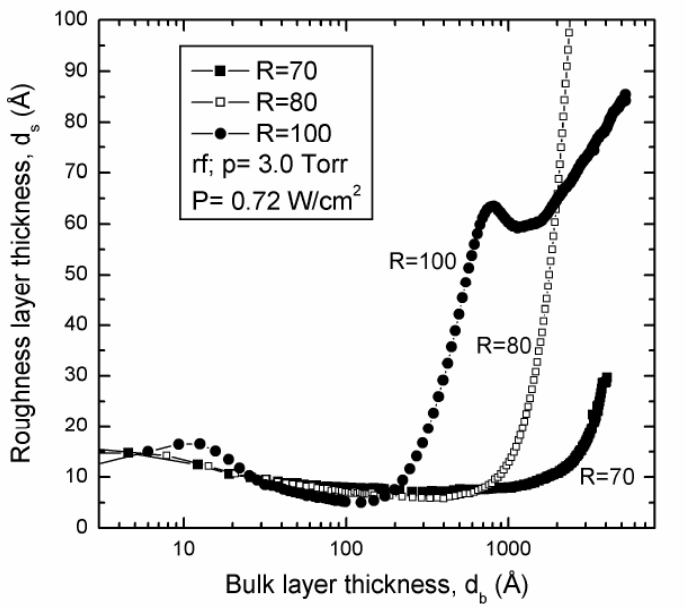


Figure 9: Surface roughness layer thickness (d_s) versus bulk layer thickness (d_b) for deposition of Si:H films by rf PECVD using H_2-dilution levels of R=70, 80, and 100 at a power level of 0.72 W/cm^2 and a total pressure of 3.0 Torr on (native oxide)/c-Si substrates.

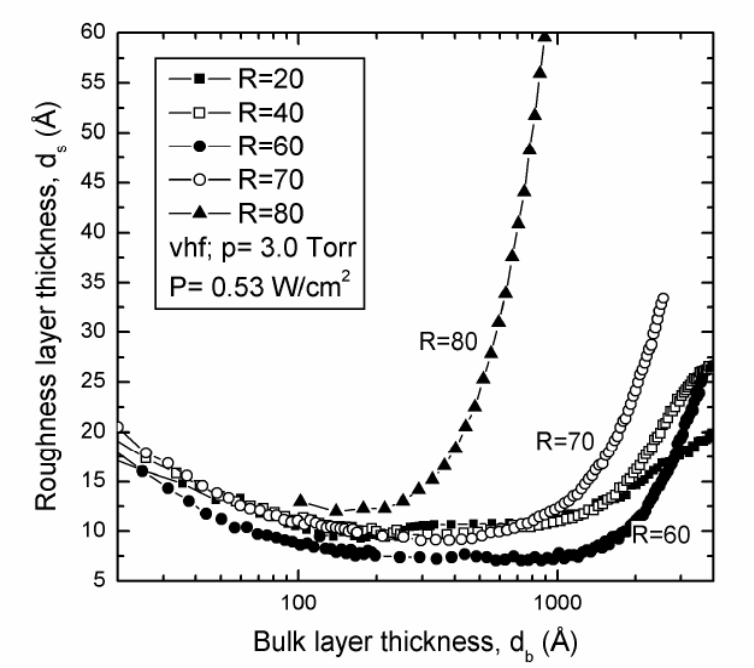


Figure 10: Surface roughness layer thickness (d_s) versus bulk layer thickness (d_b) for vhf (60 MHz) PECVD of Si:H films using H_2-dilution levels of R=20, 40, 60, 70, and 80 at a power level of 0.53 W/cm^2 and a total pressure of 3.0 Torr on (native oxide)/c-Si substrates.

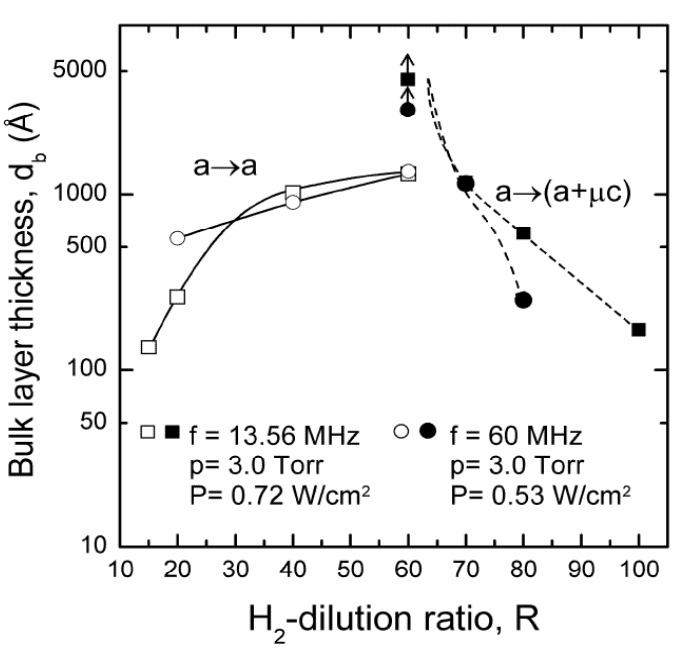


Figure 11(a): Superimposed phase diagrams for two series of PECVD Si:H films deposited on native oxide covered c-Si substrates using plasma frequencies of 13.56 and 60 MHz, at elevated plasma power levels of 0.72 W/cm^2 (rf) and 0.53 W/cm^2 (vhf) and at 3 Torr total pressure.

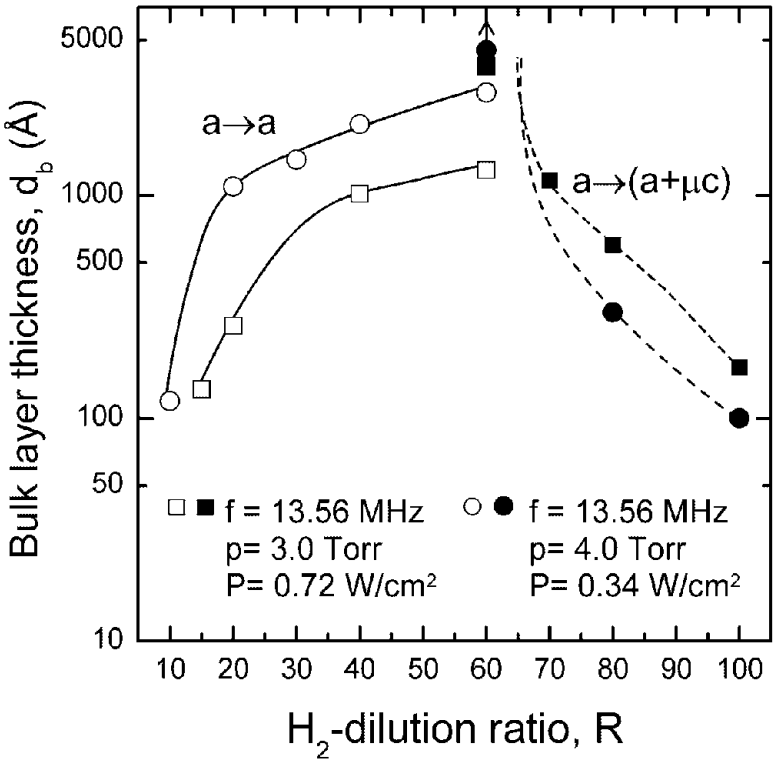


Figure 11(b): Superimposed phase diagrams for two series of PECVD Si:H films deposited on native oxide-covered c-Si substrates. Both series apply rf plasma excitation (13.56 MHz) under high pressure conditions, one with a power level of 0.34 W/cm^2, yielding a rate of 3.4 Å/s just before the a→(α+μc) transition and the other with a power level of 0.72 W/cm^2, yielding a rate of 6.5 Å/s just before the a→(a+μc) transition.

Task 2

Low Power and Pressure Si:H Depositions: Crystalline Si Wafer Substrates

Figure 12 shows deposition rates as a function of R for Si:H films prepared by rf (13.56 MHz) and vhf (60 MHz) PECVD at the minimum plasma power (0.08 W/cm^2) and low pressures (< 0.5 Torr, total). For both deposition series in Fig. 12, the films were prepared in a PECVD reactor having a parallel-plate electrode configuration with an electrode spacing of 1.9 cm, and the substrate temperature was fixed at 200°C. The partial pressure of SiH_4 was fixed at ~0.05 Torr, while the total $[SiH_4]+[H_2]$ pressure increased from 0.07 to 0.5 Torr with the increase in R.

Figures 13 and 14 depict the microstructural evolution, i.e., the surface roughness layer thickness versus the bulk layer thickness as deduced by RTSE for the vhf PECVD Si:H films of this series prepared at different hydrogen dilution levels $R=[H_2]/[SiH_4]$ on smooth, native oxide-covered c-Si substrates. The series versus R for $0 \leq R \leq 8$ in Fig. 13 depicts films that remain amorphous throughout growth and thus exhibit the weak a→a roughening transitions, whereas the films in Fig. 14 for R>10 exhibit abrupt a→(a+μc) roughening transitions as well as abrupt (a+μc)→μc smoothening transitions during growth. (Note the difference in the vertical roughness scales between the two figures.)

Figure 15 shows the phase diagram for this series of vhf (60 MHz) PECVD Si:H films superimposed on the corresponding data for the rf (13.56 MHz) PECVD Si:H films also obtained at minimum power and low pressure. For clarity only the a→a and the a→(a+μc) transitions are depicted in Fig. 15 as these are most relevant for the optimization of a-Si:H i-layers for solar cells. The boundaries for vhf (60 MHz) PECVD show two differences compared with those for rf (13.56 MHz) PECVD. First, the a→a roughening transition for the vhf series shifts more gradually to greater thickness with increasing R. As a result, just before the a→(a+μc) transition, the a→a roughening transition occurs at a much larger thickness for the lower rate (0.5 Å/s) rf deposition. Second, in the narrow range 10<R<20, the a→(a+μc) transition thickness is shifted to lower values at the higher (vhf) frequency. This latter difference suggests a much higher density of microcrystallites nucleating from the amorphous phase for vhf compared to rf frequencies. As will be seen shortly, such a strong effect is specific to the growth process on c-Si substrates, and therefore is not particularly device-relevant.

Next we will discuss in greater detail the differences in the a→a roughening transition thickness observed between a-Si:H films prepared by vhf and rf PECVD. Previous extensive correlations have shown that a-Si:H material with the largest a→a transition thickness provides the best performance when incorporated as the i-layer of an a-Si:H-based solar cell. Based on these correlations, two conclusions can be made regarding the comparison of the a→a roughening transition in Fig. 15.

First, similar transition thicknesses for rf and vhf PECVD are obtained at R=0 even though the vhf process provides a factor of ~2.5 higher rate (3.1 Å/s vs. 1.2 Å/s; see Fig. 12). This result suggests that at R=0 the deposition rate of a-Si:H films can be increased without loss of material quality by increasing the plasma frequency from rf (13.56 MHz) to vhf (60 MHz). As R is increased to its optimum value, however, the a→a roughening transition increases much more rapidly for the lower rate rf depositions. In

fact at R=10, the a→a roughening transition thickness is > 4000 Å for rf deposition at 0.5 Å/s versus ~1300 Å for vhf deposition at 1.3 Å/s. A comparison of the R=10 vhf (60 MHz) a-Si:H deposition in Fig. 14 with a series of rf (13.56 MHz) depositions performed at elevated rates simply by increasing the plasma power demonstrates that the vhf a-Si:H roughening characteristic is very similar to the rf a-Si:H roughening characteristic for the same deposition rate. This result is shown in Fig. 16, where the surface roughness evolution for the R=10 vhf deposition is superimposed upon the corresponding rf results, the latter data sets obtained at different rates by elevating the plasma power under otherwise identical low pressure conditions.

Finally Fig. 17(a) shows a comparison of the a→a roughening transition thicknesses for three low pressure processes (i) rf PECVD with minimum plasma power (0.08 W/cm^2, yielding **0.5 Å/s** at R=10); (ii) rf PECVD with high power (0.8 W/cm^2; yielding **3.5 Å/s** at R=10); and (iii) vhf PECVD with minimum power (0.08 W/cm^2, yielding **1.9 Å/s** at R=10). In all cases R=10 lies just below the a→(a+μc) boundary for a thick film. It is clear that the results for vhf PECVD trend from the low power toward the high power rf series with increasing R. Thus, it is clear that the increase in rate without loss of material quality possible with vhf over rf at R=0 is not sustained as R is increase to its optimum value of R=10 just below the a→(a+μc) boundary.

In summary, we are forced to conclude that under the optimum conditions, i.e., for depositions just below the a→(a+μc) boundary, there is no advantage to using vhf over rf deposition, the latter performed at elevated power to ensure the same rates.

Low Power and Pressure Si:H Depositions: R=0 a-Si:H Substrates

Figure 17(b) shows the microstructural evolution for Si:H films prepared by vhf (60 MHz) PECVD at the minimum plasma power (0.08 W/cm^2) and low pressure (< 0.5 Torr) on underlying R=0 a-Si:H films. These results can be compared with the corresponding ones in Fig. 14 for crystalline Si wafer substrates. This comparison is shown in Fig. 17(c) where the simple phase diagrams, including only the a→(a+μc) transition thickness, for vhf deposition on the two substrates are superimposed for comparison. As in the case of rf PECVD reported earlier, it is evident that the phase boundary in vhf PECVD shifts to much higher R when R=0 amorphous Si:H substrates are used instead of standard Si wafers. For example, at R=40 the single-phase μc-Si:H nucleates immediately on native-oxide/c-Si, whereas an optimum 200 Å thick interface i-layer can be obtained on R=0 a-Si:H (or more importantly, on the R=0 p-layer of the p-i-n solar cell). This result shows clearly that the phase of the deposited material is controlled by the substrate in the *protocrystalline* Si:H growth regime.

A comparison of phase diagrams for rf and vhf PECVD both prepared on the R=0 a-Si:H substrate films is shown in Fig. 17(d). In this figure, the results for vhf (60 MHz) PECVD are depicted as the circles and the results for rf (13.56 MHz) PECVD by the squares. Overall, the thicknesses of the a→(a+μc) and (a+μc)→μc transitions for the two different frequencies are in close agreement. The only significant difference in Fig. 17(d) occurs with R=15 in which case the a→(a+μc) transition is shifted to lower thickness for

the vhf deposition, an effect similar to that observed in Fig. 15, but not as strong. This effect may suggest that the stress in the vhf PECVD films builds up more rapidly with thickness than that in the rf films, however the origin of this behavior is unclear. Perhaps the most important consequence of the close similarities of the results in Fig. 17(d) is that the two-step optimization procedure developed for the rf PECVD i-layers of a-Si:H p-i-n and n-i-p cells would apply equally well for vhf PECVD i-layers.

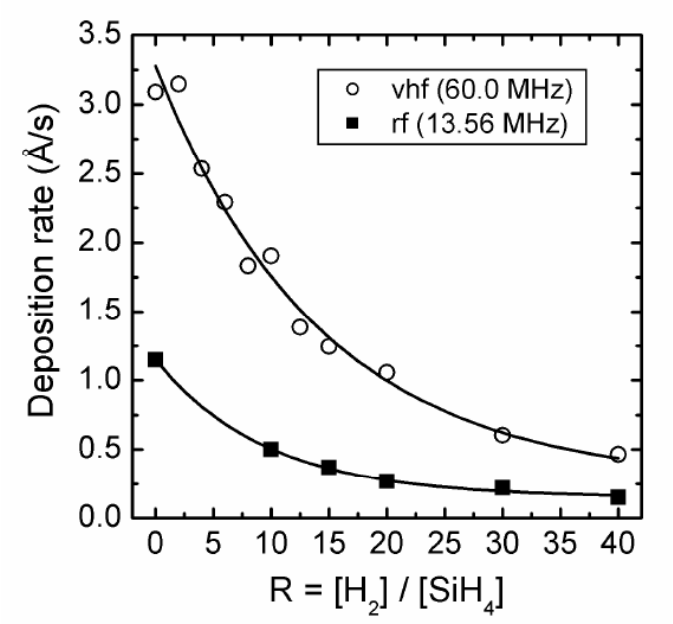


Figure 12: Comparison of the deposition rates for rf (13.56 MHz) and vhf (60 MHz) PECVD as a function of R under low power (0.08 W/cm^2) and low pressure (< 0.5 Torr) conditions.

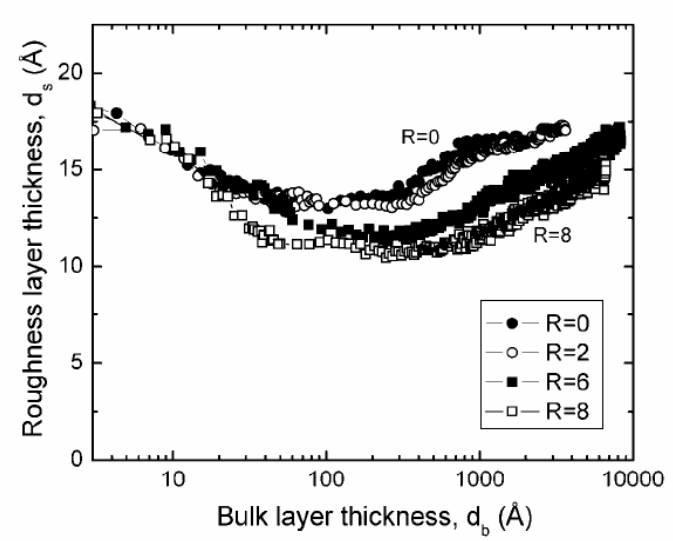


Figure 13: Surface roughness layer thickness (d_s) versus bulk layer thickness (d_b) for growth of single phase amorphous Si:H films by vhf (60.0 MHz) PECVD using H_2-dilution levels of R=0, 2, 6, and 8 in the low power (0.08 mW/cm^2) and low pressure (< 0.5 Torr) process on smooth (nat. oxide)/c-Si substrates.

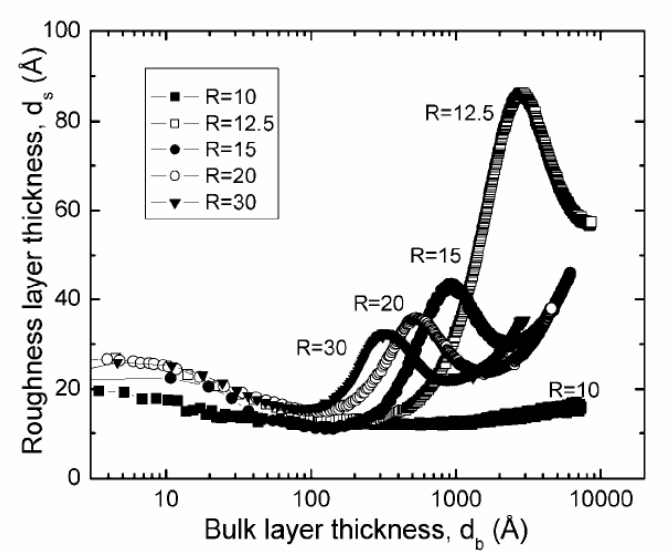


Figure 14: Surface roughness layer thickness (d_s) versus bulk layer thickness (d_b) for growth of Si:H films by vhf (60.0 MHz) PECVD using H_2-dilution levels of R=10, 12.5, 15, 20, and 30 in the low power (0.08 mW/cm^2) and low pressure (< 0.5 Torr) process on smooth (nat. oxide)/c-Si substrates. All films except the one with R=10 exhibit a→(a+μc) roughening as well as (a+μc)→μc smoothening transitions during growth.

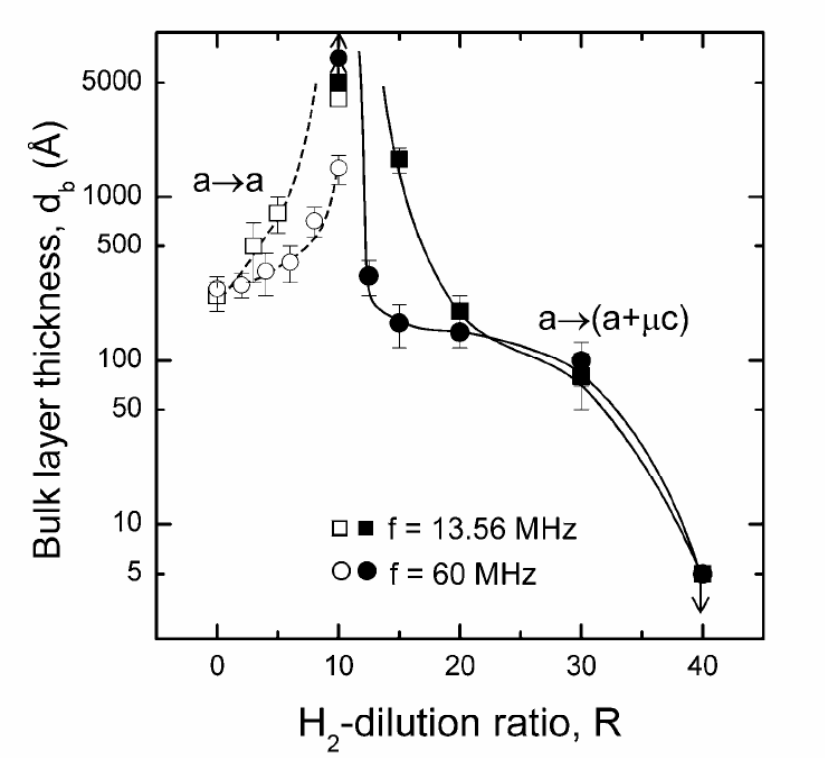


Figure 15: Superimposed phase diagrams for two series of PECVD Si:H films deposited on native oxide covered c-Si substrates using rf (13.56 MHz) and vhf (60 MHz) plasma frequencies at low power (0.08 mW/cm^2) and low pressure (< 0.5 Torr). The (up, down) arrows indicate that the transition occurs (above, below) the designated values.

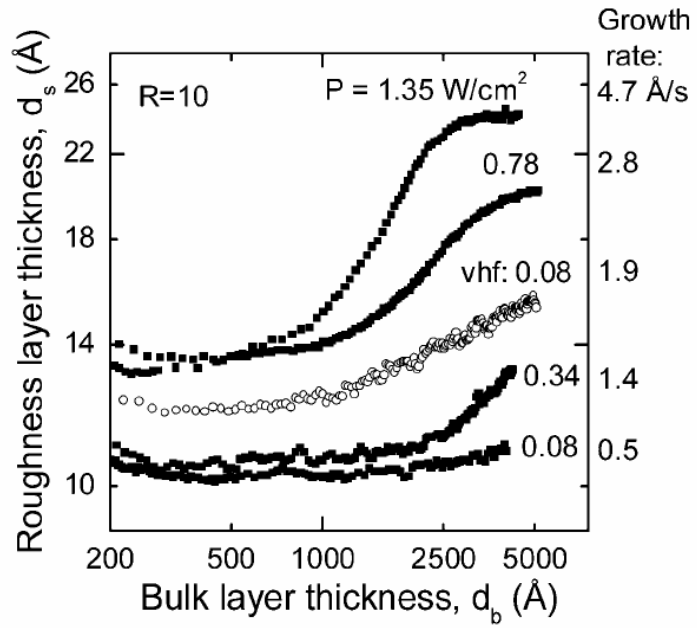


Figure 16: Surface roughness layer thickness versus bulk thickness for a series of R=10 films prepared by rf (13.56 MHz) PECVD at different plasma power levels, and for an R=10 film prepared by vhf (60 MHz) deposition at the lowest plasma power (0.08 W/cm^2). A low total pressure (0.4 Torr) was used throughout.

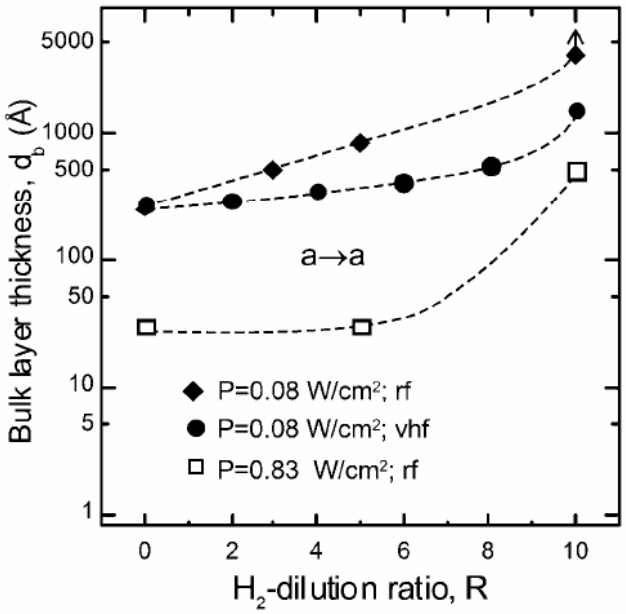


Figure 17(a): The a→a roughening transition thickness as a function of H_2-dilution ratio for three deposition series at low pressure (<0.5 Torr): (i) rf PECVD with minimum plasma power (0.08 W/cm^2, yielding 1.2 Å/s at R=0 and **0.5 Å/s** at R=10); (ii) rf PECVD with high plasma power (0.8 W/cm^2; yielding 8.0 Å/s at R=0 and **3.5 Å/s** at R=10); and (iii) vhf PECVD with minimum power (0.08 W/cm^2, yielding 3.1 Å/s at R=0 and **1.9 Å/s** at R=10).

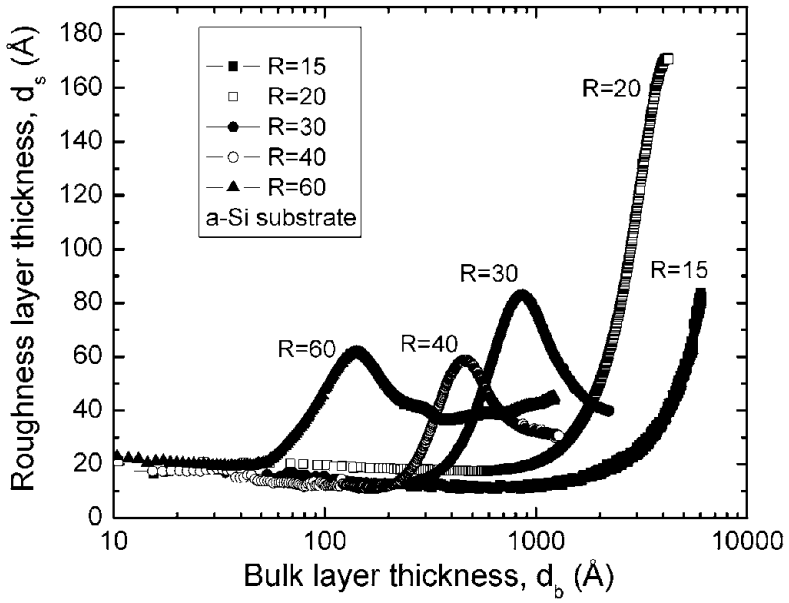


Figure 17(b): Surface roughness layer thickness (d_s) versus bulk layer thickness (d_b) for deposition of Si:H films by vhf (60.0 MHz) PECVD with H_2-dilution levels of R=15, 20, 30, 40 and 60 at low power (0.08 mW/cm^2) and low pressure (< 0.5 Torr) on R=0 a-Si:H substrates. All films exhibit a→(a+μc) roughening transitions, whereas only the films with R≥30 exhibit clear (a+μc)→μc smoothening transitions (peaks).

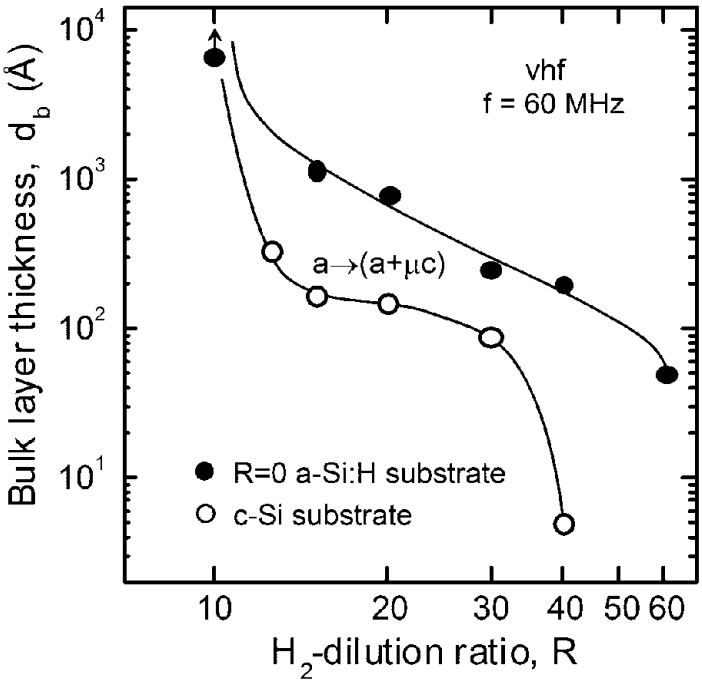


Figure 17(c): Simple phase diagrams, including only the a→(a+μc) transition thickness, for vhf (60.0 MHz) PECVD at low power (0.08 mW/cm^2) and low pressure (< 0.5 Torr) on c-Si wafer and R=0 a-Si:H film substrates.

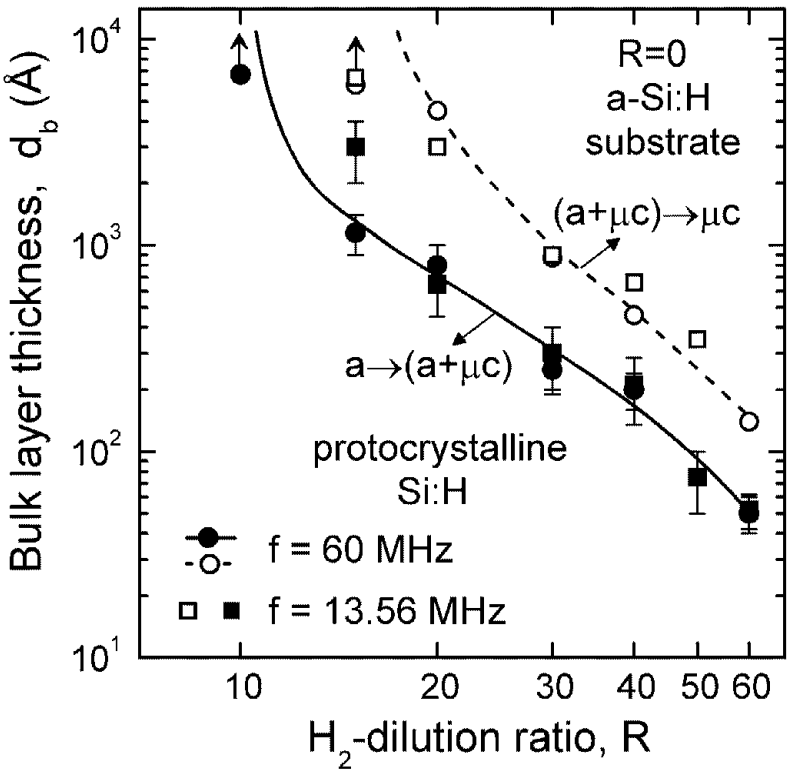


Figure 17(d): Superimposed phase diagrams comparing Si:H depositions using rf (13.56 MHz; squares) and vhf (60 MHz; circles) plasma excitation on R=0 a-Si:H substrate films. Both series of depositions were performed at low power (0.08 mW/cm^2) and pressure (< 0.5 Torr) under otherwise identical conditions.

Task 3

Device Loss Mechanisms

During the current phase additional confirmation to that reported in April 2003 Report was obtained for the presence of essentially homogeneous distributions of defects across the i-layers of a-Si:H solar cells without the large densities of defects in the vicinity of the p- and n-contacts predicted by the defect pool model. This was obtained from further studies carried out on the types of different cell structures with controlled p/i interface regions and different n, p contacts. These studies also established that dark forward bias current-voltage characteristics offer not only a novel, reliable probe for identifying and characterizing the mechanisms limiting different cell characteristics but also for characterizing the gap states in their i-layers. To further quantify the p/i recombination and to establish the range of voltages in the J_D-V characteristics over which bulk recombination dominates, studies were carried out on J_DV characteristics of cells having R=0 and R=10 intrinsic layers with different thicknesses. It is found that, even in cells in which the p/i interface regions have not been fully optimized, their J_D-V characteristics still exhibit a thickness dependence over a wide range of voltage.

This thickness dependence is illustrated in Figure 18 where the results on J_D-V characteristics are shown for two p-i-n cells with 0.4μm and 0.8μm R=10 "straight" i-layers, in which the p/i interface regions have not been modified, e.g., by introducing 200Å of a-Si:H having different R. Because the two cells have identical p/I interface regions, their p/i interface recombination is the same, whereas the bulk recombination is controlled by the change in the thickness of the i-layers. From such results it is possible first to separate and then to evaluate the contributions at the p/I interfaces and those of the bulk, the latter being proportional to the i-layer thickness. As a consequence it is possible to extract the J_D-V characteristic expected for a cell structure in which the p/i interface contribution to carrier recombination is negligible compared to that of the bulk. This is obtained from the results in Figure 18 by directly subtracting the J_D-V characteristic of the cell with 0.4μm i-layer from that of the cell with 0.8μm i-layer. In this way the recombination at the p/i interface is cancelled out. The resulting J_D-V characteristics thus corresponds to that of a cell structure having an i-layer thickness of 0.8 – 0.4 = 0.4μm with negligible contribution from any recombination in the p/i interface region.

Such a J_D-V characteristic is shown in Figure 19 along with the experimental results obtained for a p-i-n cell with a 0.4μm R=10 bulk i-layer and a 200Å R=40 i-layer at the p/i interface. Also included in this figure are the characteristics of the cells in Figure 18. It can be seen in Figure 19 that there is excellent overlap between the J_D-V characteristic extracted from the results in Figure 18 and that of the cell structure in which the p/i interface recombination has been reduced with an R=40 p/i interface region. There is a clear indication that p/i interface recombination can be virtually eliminated by the insertion of a high band gap, high quality protocrystalline material (such as that obtained with R=40) at the p/i interface. It can be seen in Figure 19 that divergence between the J_D-V characteristics of the cells with and without p/i interface layer occurs around 0.55V at which point the contributions of the p/i interface recombination of the non-optimized cell structure begin to appear. For voltages smaller than this, the p/I interface contributions are negligible compared to the recombination in the bulk. It is

important to point out here that at the higher voltages even though the p/i interface recombination becomes more and more significant it can be still smaller than that of the bulk over extended regions of voltage. In fact, it can be seen in Figure 19 that the thickness dependence of the J_D-V characteristics is still present at the higher voltages, even up to the values of open circuit voltage (~0.89 V) under 1 sun illumination. This bulk contribution is reflected in the thickness dependence of the values of 1-sun V_{OC} for the cells in Figure 18, which exhibit a difference of about 15 mV. The results on the thickness dependence obtained here show that even in the R=10 "straight" cells without the R=40 p/i interface layer, the recombination currents are not determined solely by p/I interface recombination even at the high voltages corresponding to 1-sun V_{OC} values. This allows the light induced changes in these V_{OC}'s to be used in probing the gap states limiting V_{OC} and is discussed later in this section.

Results were also obtained for R=0 "straight" cells with 0.4μm and 0.8μm thick i-layers as shown in Figure 20. Again excellent agreement is obtained between the characteristic corrected for p/i interface recombination and that of the cell with a R=40 p/I interface region. It can be seen in the figure that the presence of the R=40 layer at the p/I interface again eliminates contributions to the J_D-V characteristics due to recombination there. For the results on the R=0 cells, with and without the R=40 p/i interface region, the divergence between their J_D-V characteristics now occurs at around 0.35 V, a value smaller than that for the R=10 cells in Figure 20 (0.55 V). This reflects the higher p/i interface recombination in the R=0 straight cells than in the R=10 straight cell as would be expected from the lower band gap as well as the absence of protocrystallinity in the R=0 i-layers. That this is indeed the case is reflected in the virtual absence of any thickness dependence in 1 sun V_{OC}'s.

These results clearly show that by having R=40 interface layers in both R=10 and R=0 a-Si:H cells which the recombination at the p/i interfaces has been reduced to such a degree that the J_D-V characteristics are indeed dominated by bulk recombination over a wide voltage regime. Consequently, differences in the gap states in the R=10 and R=0 intrinsic layers of solar cells can be evaluated directly from their J_D-V characteristics, and correlations can be made between the various resulting parameters and characteristics with those obtained on the corresponding intrinsic films.

Potential Barriers in i-layers adjacent to the p,n contacts

The effect of the large concentrations of free carriers at the p- and n-contacts in creating potential barriers V_p, V_n respectively has been discussed in April 2003 Report. The nature of these barriers depends on the concentrations of these carriers and the defect states in the i-layer adjacent to the contacts. Both V_p and V_n, even in absence of high densities of defects predicted by the pool model, affect the transport across the cell and limit current injection into the i-layer at high forward bias.

There have been many studies focusing on the effect of p-layers on the performance of a-Si:H solar cells. On the other hand, there have been fewer studies on the effect of n-layers and even in such studies on n-layers the explanations of their role in determining the solar cell performance have been somewhat misleading. This is due to the incomplete characterization of their effect on different cell parameters and

interpretations based on the presence of large densities of defects in the vicinity of these contacts. In order to obtain further insight into the nature of the potential barrier, V_n, in the i-layer at the n contact due to the high density of electrons there[3]. Studies were carried out on identical a-Si:H p-i-n cell structure but with n-a-Si:H and n-μc-Si:H contacts. The n-a-Si:H material has a mobility gap E_μ of ~ 1.80 eV and activation energy of 0.26 eV and the n-μc-Si:H material has a E_μ of 1.1 eV and activation energy of 30 mV. Figure 21 shows the J_D-V characteristics for both the cells. Clearly seen from the figure, there is excellent overlap between the two characteristics up to around 0.8 V before they diverge which indicates that bulk recombination is the same in both cells[4]. The cell with a-Si:H n-layer exhibits lower current at high forward bias than that does the cell with μc-Si:H n-layer indicating some effective series resistance introduced by incorporating a-Si:H n-layer into the cell. However, although the conductivity of the a-Si:H n-layer is lower than that of the μc-Si:H n-layer, it is still much greater than that of the a-SiC:H p-layer so that the bulk resistance of the n-layer is not the limiting factor in the current transport across the cell. Such an effective series resistance then can be only due to the remaining difference between the two n-layers; positions of E_F in the n contact relative to the conduction band (E_c) of the i-layer, which leads to different magnitude of the current limiting barrier V_n. It has been shown that the offsets between the conduction and the valence bands of a-Si:H and that of μc-Si:H are approximately equal[5], so that E_c of n-μc-Si:H is lower than that of i-a-Si:H by as much as 0.35 eV. However, due to this large conduction band offset, even though the Fermi level E_F is closer to E_c in μc-Si:H n-layer than that in a-Si:H n-layer, it is further away from E_c in the i-layer at the n/i interface of the cell with μc-Si:H n-layer than that in the cell with a-Si:H n-layer. Consequently higher electron concentration in the i-layer near the n/i interface in the cell with a-Si:H n-layer results in a V_n which then imposes a larger limitation on the current across the cell at high forward biases.

The absence of any effect on the exponential regions of J_D-V characteristics by V_n seen in Fig. 21 further confirm the presence of small values for barriers at the contacts of the cells in this study. Since these barriers are important at high forward bias, where they affect both the potential distribution across the bulk and current injection, they do have an effect on the FF. This is reflected in the difference between FF's of the two cells. Due to a higher V_n, the cell with the a-Si:H n-layer has a FF of 0.68, much lower than that of the cell with μc-Si:H n-layer (0.73). On the other hand, as expected, both of the cells have the same V_{OC} (0.92 V), since at open circuit condition there is no net current flowing through the cell so that there is no current limiting effect from the barrier at the n/i interface.

In the work reported recently on the effects that a-Si:H and μc-Si:H n contacts have on V_n, where there were no comparisons made between the J_D-V characteristics, quite misleading conclusions were presented based on results of just V_{OC} and numerical modeling[6]. These included that there is no "gain" from replacing a-Si:H n-layer with the μc-Si:H n-layer and, contrary to our results, that due to the large band discontinuity there is a *larger potential drop* at the n/i interface in the cell with μc-Si:H n-layer instead of in

[5] R.J. Koval, A.S. Ferlauto, J.M. Pearce, R.W. Collins, and C.R. Wronski, *J. Non. Cryst. Solids*, **299-302**, 1136 (2002)

[6] Y. Poissant, P. Chatterjee, and P. Roca i Cabarrocas, J. Appl. Phys. **93**, 170, 2003.

the cell with a-Si:H n-layer.. These conclusions are based on the assumption that V_{OC} is determined by the built-in potential, which is only true when the current transport is completely interface recombination dominated. However, there is no supporting evidence from experimental data, such as J_D-V characteristics, for such an argument. In fact, it will be shown later that 1-sun V_{OC}'s can be determined by bulk recombination, thus not being affected by the built-in potential so that no conclusion can be drawn about the built-in potentials in different cells by just comparing 1 sun V_{OC}. The presence and nature of the potential barrier V_n, indicated by the results obtained from J_D-V characteristics consistent with the results on FF, further demonstrate the powerful tool that these characteristics offer in addressing the mechanisms limiting the performance of a-Si:H solar cells.

Bulk Recombination Limitations on 1-sun V_{OC}

In a well designed cell structure with optimized p/i, n/i interfaces and n, p contacts, the current transport in the dark and under illumination are both dominated by the recombination in the bulk of the i-layer. This has been verified with the detailed studies on a series of p-i-n solar cells having R=0 i-layer with different thickness of 0.4μm, 0.8μm, and 1.5μm, respectively. In these cells, the interface recombination has been minimized by incorporating a 200 Å thick R=40 intrinsic layer at the p/i interface. As has been previously reported[7], the J_D-V characteristics of such cells exhibit clear thickness dependence. This is illustrated in Figure 22 together with results that for the *first time clearly* establish the thickness dependence of the 1 sun V_{OC} in these cells. It is worth stressing here the well recognized fact that both the interface recombination and bulk recombination depend on the carrier concentrations in the i-layer. Because these have an exponential dependence on the mobility gap, E_μ, and the subsequently strong dependence of V_{OC} on E_μ, their values must be taken into account when the comparison is made between V_{OC}'s of cells having different i-layers. This unfortunately is not generally done and in particularly when "record" values are being reported or limitations on V_{OC} being proposed from "analysis" based on results on different cells.

The results presented are for cells where the R=0 i-layer has an E_μ of 1.78eV obtained from internal photoemission measurements. The illumination levels under which the V_{OC}'s were measured were adjusted for each cell so that the J_{SC} (7.5 mA/cm^2) is the same and is very close to the value under 1 sun illumination. From the figure, it is clearly seen that the V_{OC} decreases with the i-layer thickness due to the higher total recombination current in the thicker cells, which confirms the bulk dominance of the recombination current. It is very important to note here that to obtain the thickness dependence of the V_{OC}, the measurements should not be carried out under a constant illumination level for all the cells as has been done in many studies carried on the thickness dependence of V_{OC}. When the illumination is constant for all the cells the total generation current of a thicker cell is higher, which cancels out its higher bulk recombination current so that it will have a similar V_{OC} as that of the thinner cells. This is a possible reason for the reported absence of thickness dependence of V_{OC} which would lead to the wrong conclusions about V_{OC} not being bulk recombination limited even when the interface recombination has been minimized. For example with i-layer

[7] NREL Annual Report 2002, Penn State University.

thickness of 0.4μm, 0.8μm, in which the thickness dependence of V_{OC} was established here under the condition of constant $J_{SC,}$ have exactly the same V_{OC} (0.906 V) under 1-sun illumination.

The dominance of V_{OC} by bulk recombination in the cells was further confirmed by the light induced changes (SWE) in the i-layers. Figure 23 shows the light induced degradation kinetics of the 1-sun V_{OC} for the cell with 0.4μm thick i-layer. From the figure, it can be clearly seen that a decrease in V_{OC} occurs instantaneously due to the introduction of the light induced defects and corresponding increase in bulk recombination. In addition to confirming the bulk recombination limitation on V_{OC}, the results in Figure 23 indicate that the 1-sun V_{OC} is not limited by the tail states since their densities and thus carrier recombination through them does not *increase* due to SWE. When the 1 sun V_{OC} is limited by p/i interface recombination, as in the case of R=0 i-layer cells with no R=40 p/i interface states, there is a marked delay in the lower 1 sun V_{OC} degradation.

Limitations on FF

Although fill factors are critical parameters for determining the performance of solar cells, they have not been fully characterized due to the complexities associated with the contributions due to the properties of bulk i-layer, p/i, n/i interface regions and n, p contacts. In spite of this, it is still possible to identify and characterize some of the mechanisms determining the FF. In order to investigate these mechanisms an approach has been taken in which carefully designed cell structures are studied under different illumination intensities and some preliminary results are presented here.

For an ideal p-i-n or n-i-p a-Si:H solar cell without any defects and series resistance effects, its FF is only determined by the slope of the light current drop near V_{OC} when the generation current is canceled out by the exponentially growing forward bias current. This slope is determined by both the diode quality factor, n, of the solar cell and the illumination intensity where lower values of n and higher illumination give a higher FF. Consequently, in a cell where n is constant, the FF simply increases with illumination intensity. However, in a-Si:H solar cells, two additional contributions to the FF have to be included: the defect states in the i-layer and effective series resistance. Recombination through the defects reduces the collected photo-generated current and the effective series resistance reduces the carrier collection by reducing the electric field across the bulk i-layer. This effective series resistance can be either due to the bulk resistance of the non-optimized (resistive) n, p contacts, or due to the current limiting barrier formed near the p/i and n/i interface due to the space charge effect, as has been discussed earlier[7].

The effect of illumination intensity on these two contributions is the following. For higher illumination intensities, the increase in quasi-Fermi level splitting results in more gap states acting as recombination centers and the carrier recombination increases by a factor larger than that of the increase in the photo-generated current. At the same time, reduction in the electric field across the bulk caused by the effective series resistance becomes larger as the potential drop across the barriers in the vicinity of the contacts increases due to the higher photo current. Consequently, the observed decreases

of the FF at high illumination levels in a-Si:H solar cells are due to these two factors.Preliminary results shown in Figure 24, where the FF's of the two cells of Figure 1 are plotted versus J_{SC}, indicate the validity of the above discussion and that the approach taken will offer new insights into the factors limiting FF. It can be clearly seen that, as expected, both FF's increase with J_{SC} at the low illumination intensities but decrease with J_{SC} at high illumination intensities. In addition, the FF's for the cell with a-Si:H n-layer are significantly lower at the high illumination intensities than those for the cell with the μc-Si:H n-layer due to the larger current limiting barrier at the n/i interface discussed earlier. These preliminary results indicate that studies carried out in detail on carefully designed cell structures will lead to a clearer understanding of the bulk, contact and interface limitation on the FF in a-Si:H solar cells.

Thermal Annealing of SW Defects at 25^{o}C after 1 sun Degradation

Relaxation at room temperature of light induced defect states created by 1 sun illumination has not been previously observed (reported). This relaxation is readily observed at low forward bias voltages where the currents are determined by bulk recombination in the i-layers. The kinetics and extent of this relaxation in the recombination currents depend on the forward bias voltage at which it is being characterized. The differences are attributed to the increases in the quasi-Fermi level splitting and in the intrinsic carrier recombination both of which occur at the higher voltages. This clearly points to a phenomenon that is directly related to defect states in close proximity to midgap and depends on the carrier recombination that is negligible to that occurring under 1 sun illumination.

This phenomenon occurs in solar cells with both R=10 and R=0 i-layers and, as may be expected, depends on the temperature at which the 1 sun illumination is carried out. The results for 1 sun illumination and the subsequent relaxation at the same temperature of 25^{o}C and 50^{o}C are shown in Figure 25 for a R=10, 0.4μm p-i-n cell. The figure shows the recombination currents, corresponding to a quasi-Fermi level splitting of 0.4eV, normalized to their initial currents upon degradation. A very large, ~50%, decrease can be seen in the figure of the carrier recombination through the states close to midgap. It is also noteworthy that the kinetics of the relaxation at the two temperatures are so distinctly different that it is not possible to consider it in terms of a thermal annealing process with an identifiable activation energy.

The results obtained on this thermal relaxation of light induced defect states close to midgap are highly significant. They introduce even more complexity into the nature of the light induced defects but may offer some additional insight in addressing the mechanisms responsible for creating SWE defects. That the changes found here in light induced defects at midgap are so large maybe somewhat surprising. However that they have not been observed (reported) previously in the extensive studies on either cells or films is because they can be readily detected and characterized only in the presence of small quasi-Fermi level splitting and low carrier recombination.

In view of the above results on cells, a very careful investigation of the 1 sun light induced changes was undertaken on corresponding thin films. In these studies the importance of both quasi-Fermi level splitting and carrier recombination was recognized.

The results confirm this relaxation of SWE at 25°C after 1 sun illumination with photoconductivity measurements and are discussed in Task 4.

Creation of Defect States in i-layers by Recombination of Carriers under Forward Bias

Although the exact mechanisms responsible for the creation of the light-induced defect states are not yet clear, it is generally agreed that the defects are created by the trapping and/or recombination of the electron-hole pairs created under illumination and not the illumination itself. It has been shown that defects can also be created in the cells under far forward bias through double injection and subsequent recombination of the electrons and holes and this has been utilized in some experiments to replace light illumination for achieving degraded states. However, up to now there have been no systematic studies on this alternative approach for creating defects in cells. The possibility of creating SWE type defects in a controlled way by far forward biasing of cells offers a very useful tool in studying the creation and annealing of these defects. It offers a convenient way of creating the defects at different cell temperatures and characterizing them directly with J_D-V characteristics obtained at the same temperature.

A study was carried out on p-i-n cells to establish that in cell structures, which have low recombination in the p/i regions, the kinetics of defect creation with 1 sun illumination can be reproduced with a forward bias dark current having the same value as the 1-sun short circuit current. Results are shown in Figure 26 for the J_D-V characteristics for a p-i-n cell with R=10 bulk i-layer and R=40 p/i interface region obtained during degradation carried out with 1 sun illumination as well as that obtained under forward bias current of 10 mA/cm^2, equal to the short circuit current at 1 sun illumination. It can be seen in Figure 8 that there is excellent agreement between the results obtained with these two defect creation processes for the same degradation times. This shows that equivalence exists between the two methods in creating defect states, in both the magnitude as well as rate of creation. Because of this equivalence of defect creation under far forward bias and light illumination, far forward bias current degradation with appropriate cell structures is being utilized in characterizing the creation, annealing and relaxation studies on SW defects.

Voltage-Dependent Differential Diode Quality Factors n(V)

The results presented above as well as those previously reported[8] show that the distributions of defects across the i-layers are homogeneous without the presence of the large densities of defects at the p/i or n/i interface regions as predicted by the defect pool model. It was further shown that the contributions to the J_D-V characteristics from different parts of the cells, i.e. p/i interface, bulk i-layer, n and p contacts, could be identified and separated. This has created a solid ground for the direct characterization of the bulk i-layer properties through detailed analysis on J_D-V characteristics of properly designed cell structures. It has also been shown that within the voltage range over which the J_D-V characteristics are dominated by the contribution from the bulk i-layer, the

[8] Penn State NREL Annual Report 2002

carrier transport is governed by Shockley-Reed-Hall diffusion/recombination mechanisms. This makes it possible to study the defect distribution in the bulk not only qualitatively but also quantitatively based on the theoretical considerations presented in Appendix A. As a first step here, the diode quality factors n extracted from J_D-V characteristics are studied in detail to illustrate this new possibility.

As pointed out in the previous report, the diode quality factor n of a p-i-n solar cell reflects which part of the cell is dominating the carrier transport. For bulk dominated currents, n has values between 1 and 2; for p/i interface dominated currents, n has values close to 1; for currents limited by carrier injection at n and p contacts, n has values greater than 2. However, in a-Si:H solar cells, which contribution dominates J_D-V characteristics depends on the applied forward bias voltages. In general, bulk recombination dominates at low voltages; p/i interface recombination dominates at relatively higher voltages; carrier injection limited currents dominate at far forward bias and there are no sharp boundaries between these regimes. Consequently in general n is not a constant as has been generally considered but instead is a function of applied voltages. This is also true in a-Si:H solar cells even when the currents are completely dominated by bulk recombination due to the continuous and complex energy distribution of gap states. In such a case the gap state distributions are reflected in the variation of n with voltages. The voltage dependent diode quality factors can now be best represented by "differential diode quality factors n(V)", which are defined as the inverse of $[kT/q][(\ln J_D)/dV]$.

Such differential diode quality factors n(V)'s of three different cells in the annealed state are shown in Figure 27. All of these cells have identical bulk i-layers (R=10, 0.4μm) but different p/i interface layers which include R=40, R=10 and R=0 i-layers. As has been shown in the previous reports, higher values of R at p/i interface leads to lower recombination rate there. For R=40 p/i, the interface recombination is reduced so much that the bulk recombination dominates over a wide range of voltages (up to ~0.8V); for R=10 p/i, the interface recombination becomes non-negligible after ~0.5V; while for R=0 p/i, the interface recombination dominates the J_D-V characteristics down to very low voltages (<0.2V). These observed features from J_D-V characteristics are even clearer from the results shown in Figure 27. For R=0 interface, the values of n remains very low (<1.2) over a relatively wide voltage range (0.4 – 0.65V) indicating the dominance of interface recombination over these regimes. At voltages ≤ 0.4V the contributions from bulk start to increase the values of n where in this case at the lowest voltages contributions from shunts lead to values even larger than 2 (not shown here). At higher voltages, the current gradually becomes carrier injection limited and n finally increases to values greater than 2. For R=10 p/i, n never reaches the values as low as in the case of R=0 p/i, indicating that the contributions from p/i interface recombination are absent over a wide voltage range. For R=40 p/i, n values become even larger indicating further reduced p/i interface recombination. An indication of n(V) for the recombination currents at p/i interfaces can be obtained from he difference in the currents of the cells with R=40 and R=0 p/i interface regions. Clear indications are obtained for a constant n(V) of a value of 1 for this recombination over the voltage range of ~ 0.3 to 0.6V. From the figure it can be also seen that there is good overlap between the n(V)'s of the cells with R=40 p/i and R=10 p/i both at low voltages (up to about 0.45V) where both the cells exhibit bulk dominated currents and at high voltages (above about 0.85V) where the currents in

both cells become carrier injection limited. For the voltages between these two regimes, n is smaller in the cell with R=10 p/i indicating the non-negligible contribution to the currents from p/i interface. Also it can be seen that the n for the cell with R=0 p/i reaches values larger than 2 at voltages lower than that in the case of the other two cells. This is consistent with the fact that the currents in this cell reach carrier injection limitation at a lower voltage due to the higher value of the currents in this cell which has a lower bandgap for the bulk i-layer material.

The relation between n(V) and carrier injection limited currents is more clearly shown with the results in Figure 28 on the cells with different potential barrier V_n, achieved by using two different n contacts, one is the a-Si:H material and the other is the μc-Si:H material. Shown in Figure 28 are the n(V) characteristics for these two cells. It can be seen that the voltage at which n starts to become larger than 2 is smaller in the case of the cell with an a-Si:H n contact, consistent with the results on J_D-V characteristics and the FF's of these cells.

The n(V) characteristics not only help to identify the voltages regimes over which the currents are dominated by the recombination at p/I interface, the bulk or carrier injection limitations but also provides insights of the gap state distribution in the case of the bulk recombination dominated regimes. Shown in Figure 29 are the n(V) characteristics for cells in their annealed state with R=10 and R=0 bulk i-layers in which the p/i recombination is minimized by having R=40 i-layer at p/i interface. In these two cells, the currents are bulk recombination dominated at voltages up to about 0.8V. As has been discussed earlier the n(V) should be a constant with a value smaller than 2 only in the case of a strictly exponential distribution of defects in the gap. However, the n(V) for both the cells drop from a larger to a smaller value at voltages around 0.3V, which is believed not to be due to any artifacts from shunts. This suggests the existence of a distribution of defect states near the mid gap within a relatively narrow energy range. The density of these defect states reach maximum values close to mid gap then drop sharply for energies further away from mid gap. At energies even further away from mid gap the defect densities begin to increase with an exponential-like dependence on energy, which is reflected in the relatively constant values of n(V) for voltages higher than about 0.4V. However in these higher voltage regimes, as can be seen from the figure, there are distinct differences between the n(V)'s of the two cells not only in their magnitude but also in the shape of the n(V) curves – a clear indicator of a difference in the gap states distribution of the R=10 and R=0 intrinsic materials. Although more complex analysis is needed to obtain the exact distributions, there is already a clear indication in these results that the distribution of the states nearest mid gap is broader in R=0 i-layer than in R=10 i-layer for their annealed state from the fact that these n(V) characteristics exhibit higher values in the case of the R=0 cell.

Applying the above analysis to the n(V)'s of the R=10 and R=0 cells after prolonged exposure to 1 sun illumination it is found that the energy distributions of the light induced defects in the two cells are also distinctly different. Shown in Figure 30 are the n(V) characteristics for the cells of Figure 29 after 100 hour's degradation under 1 sun illumination at 25^{o}C. From the figure it can be seen that the shape of the n(V) of R=10 cell becomes similar to that of the R=0 cell in its annealed state. This indicates that the light induced defect states in the vicinity of mid gap have a broader distribution than in the annealed state. On the other hand the shape of the n(V) curve of R=0 cell also

changes significantly from that in the annealed state. The values of n(V) increase monotonically with voltage indicating that the light induced defect state density near mid gap is higher than that further away from mid gap. The changes of the shape of n(V) curves obtained for both cells point to an important fact that the light induced defects are not created uniformly across the energy gap and have different energy distributions in the R=10 and R=0 a-Si:H materials. Currently the distributions of gap states in the i-layers, both in annealed state and after degradation, are being directly derived from the J_D-V characteristics.

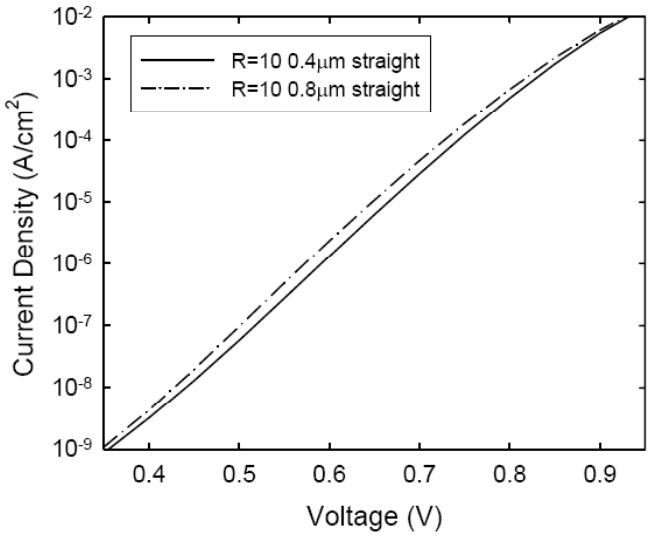


Figure 18: J_D-V characteristics for R=10 a-Si:H cells with two different thickness i-layers.

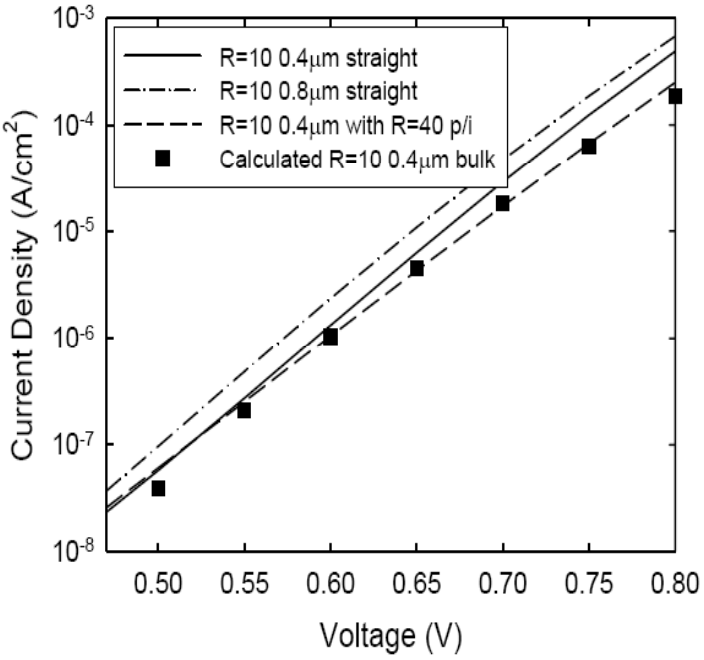


Figure 19: J_D-V characteristics for R=10 cells with and without a p/i interface layer and the predicted result for a R=10 cell structure in which the p/i recombination is negligible.

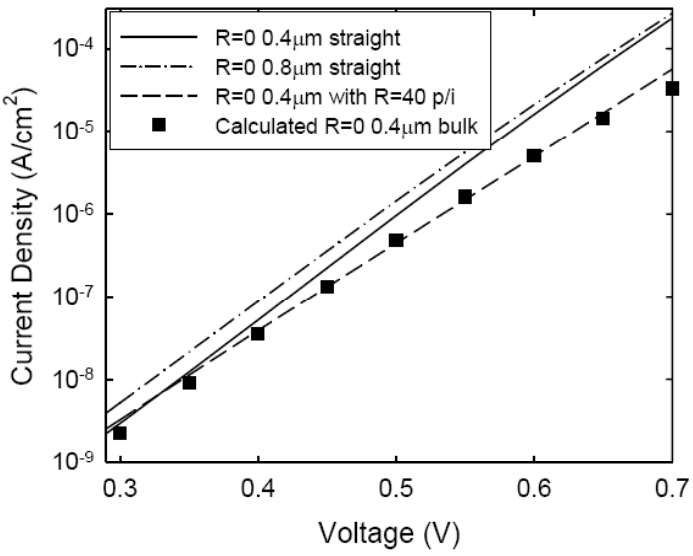


Figure 20: J_D-V characteristics for R=0 cells with and without a p/i interface layer and the predicted result for a R=0 cell structure in which the p/i recombination is negligible.

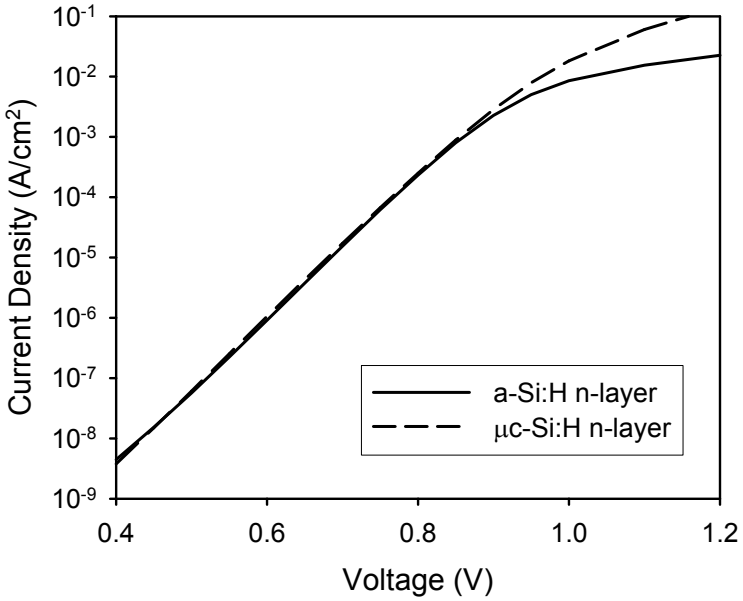


Figure 21: J_D-V characteristics for two p-i-n solar cells having the identical cell structures except one with a-Si:H n-layer and the other with mc-Si:H n-layer.

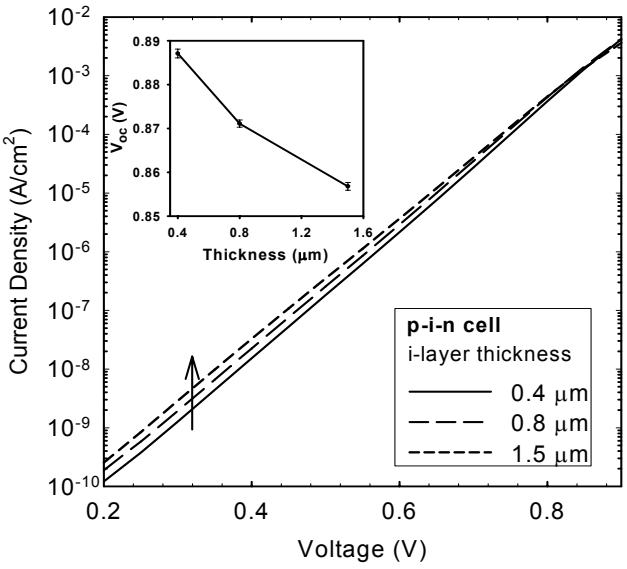


Figure 22: J_D-V characteristics of p-i-n solar cells having R=0 i-layer with different thickness of 0.4mm, 0.8mm, and 1.5mm, respectively. Shown in the inset is the V_{OC}'s of these cells under red light illuminations which induce a constant J_{SC} for all the cells very close to that at 1 sun.

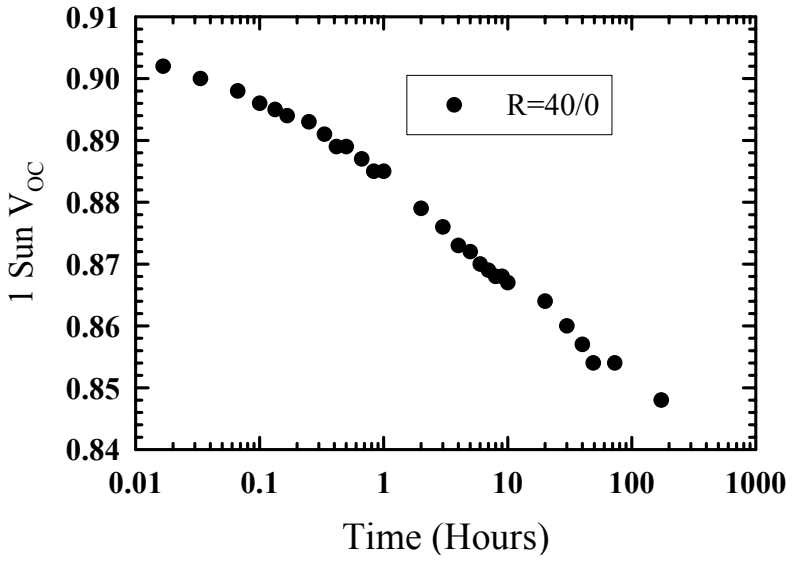


Figure 23: Light induced degradation kinetics of the 1-sun V_{OC} for the cell with 0.4mm thick R=0 i-layer and 200 Å thick R=40 at the p/i interface.

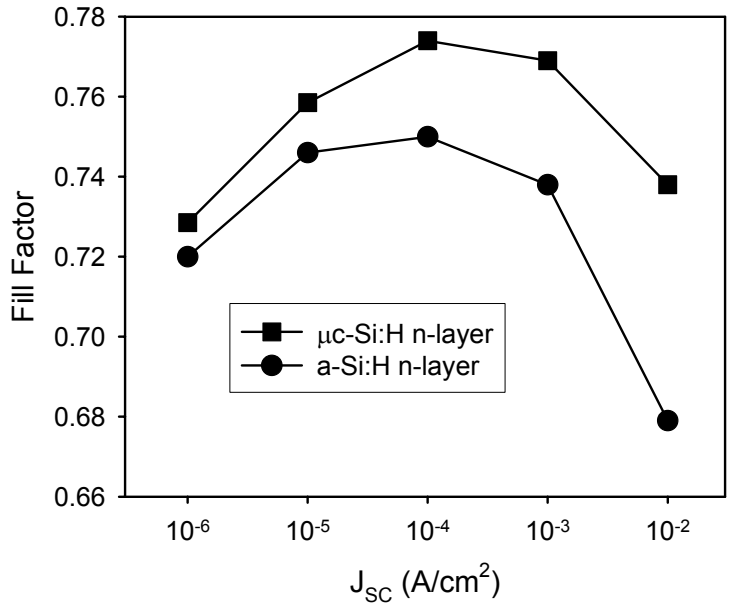


Figure 24: Variation of fill-factors as illumination levels change for the cells in Figure 1.

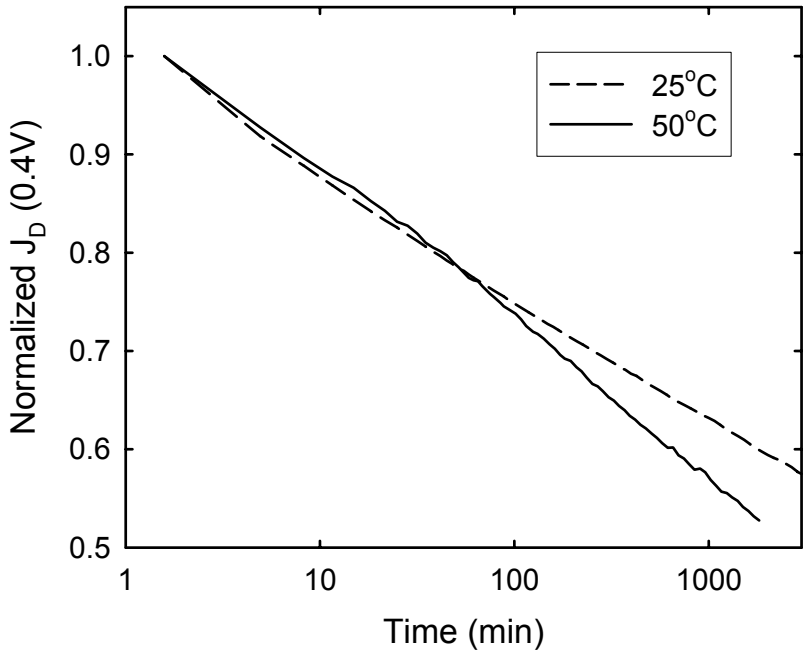


Figure 25: Relaxation in J_D (0.4V) at 25°C and 50°C after 1 sun illumination for 30 minutes at the same temperature.

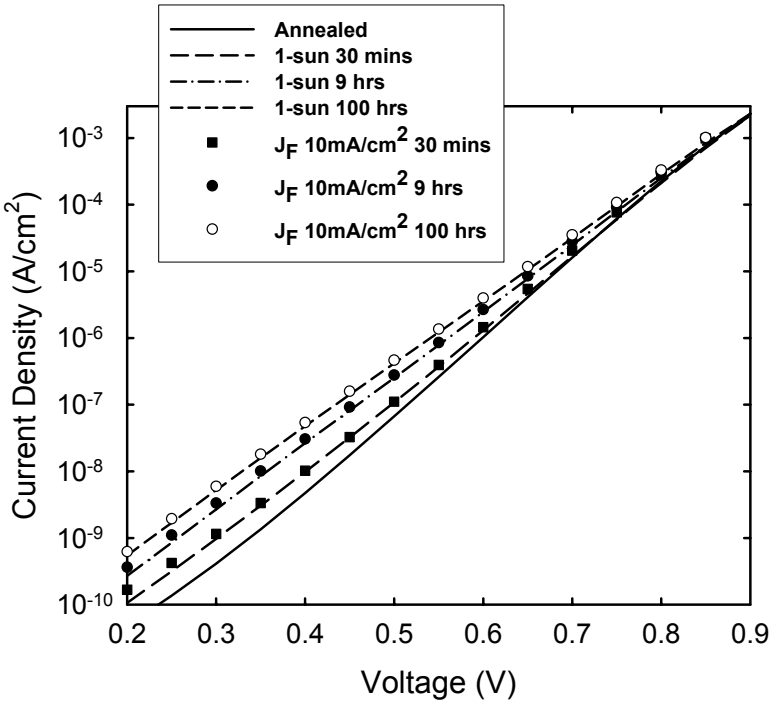


Figure 26: J_D-V characteristics of the p-i-n cell with 0.4μm R=10 bulk i-layer and R=40 p/i interface layer at different degradation times obtained through 1-sun illumination as well as equivalent forward bias current.

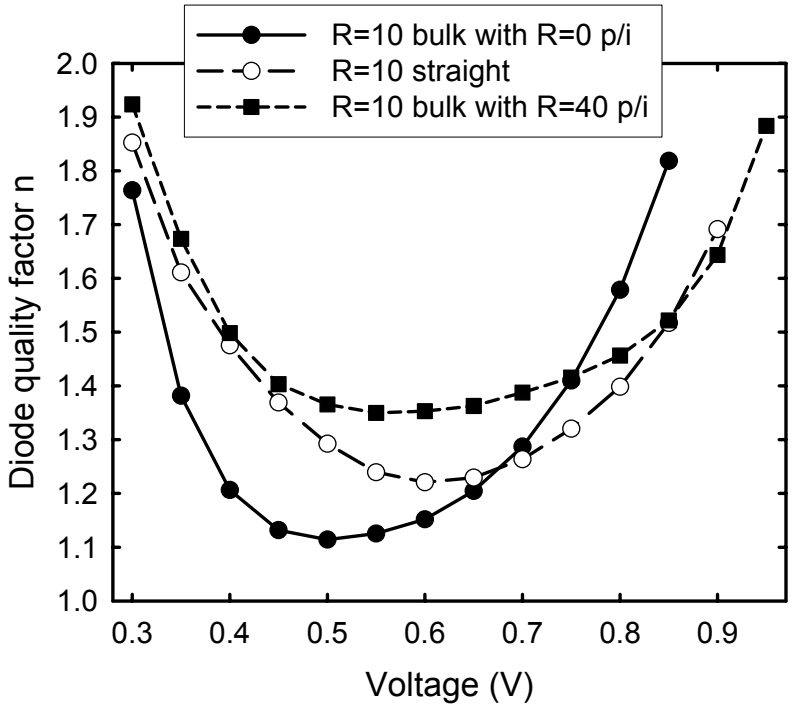


Figure 27: n(V) characteristics of p-i-n cells with 0.4um R=10 i-layers but having different p/I interface layers.

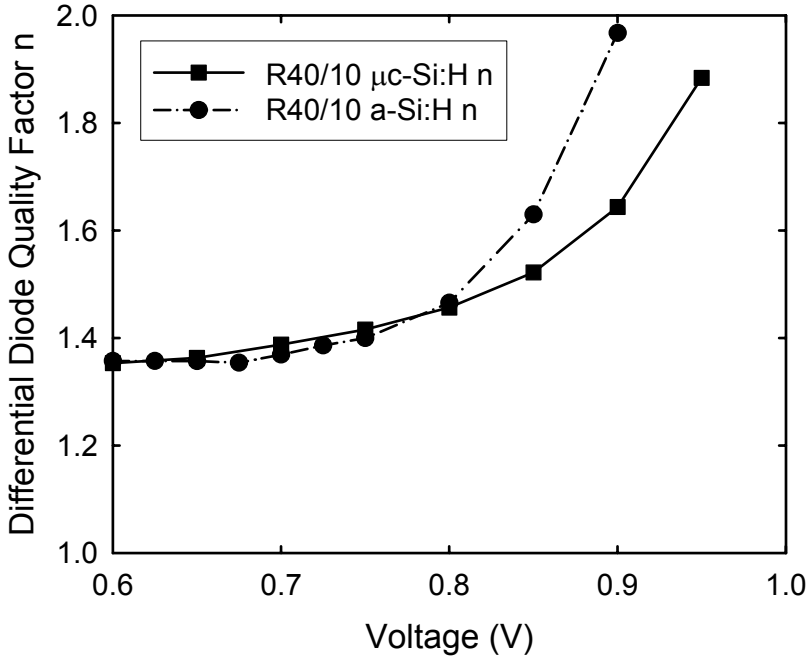


Figure 28: n(V) characteristics of p-i-n cells with 0.4 um R=10 i-layer and 200 Å R=40 i-layer but having different n layers

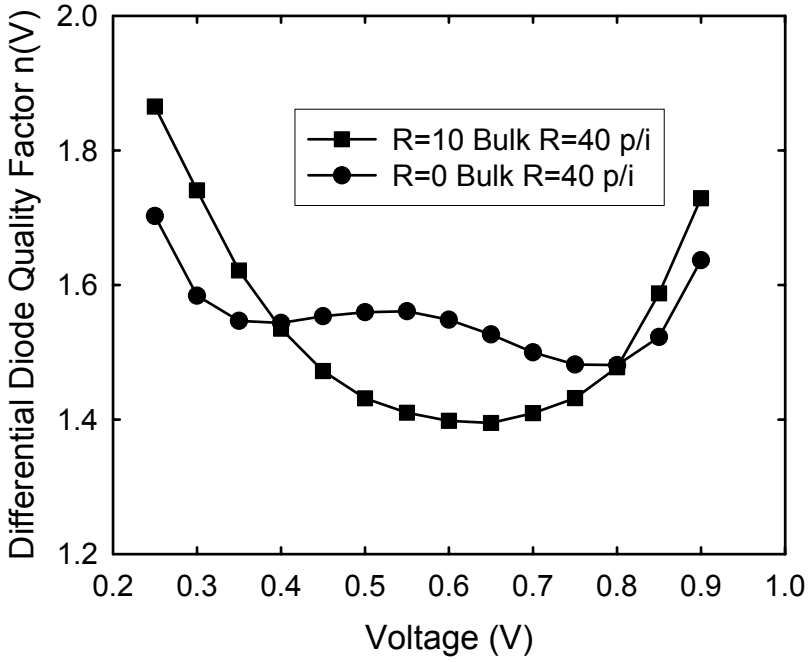


Figure 29: n(V) characteristics of p-i-n cells in their annealed state with R=40 p/i interface layer but having different bulk i-layers.

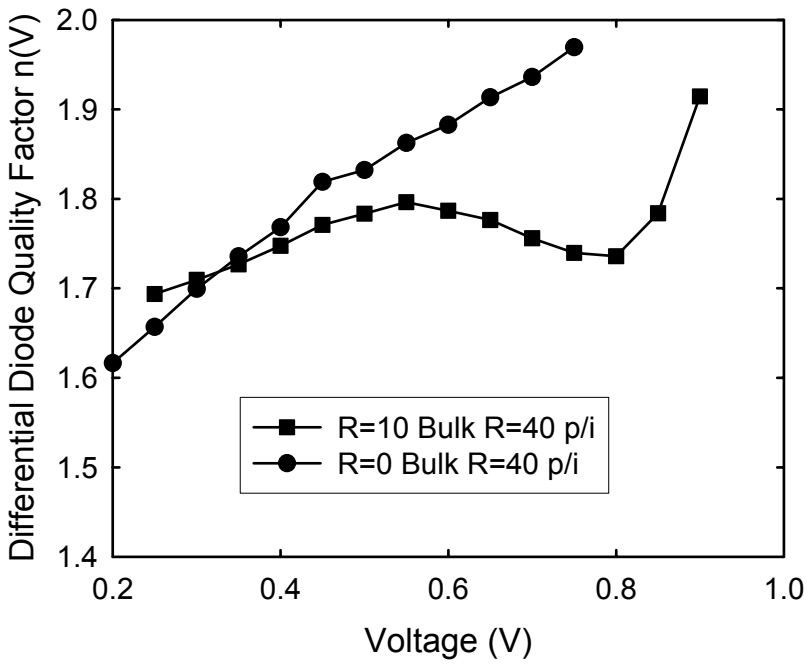


Figure 30: n(V) characteristics of p-i-n cells in their degraded state with R=40 p/i interface layer but having different bulk i-layers.

Task 4

Novel Analysis of RTSE applied to Amorphous-to-Microcrystalline Phase Transition Region

For thin films based on a-Si:H, researchers have established an effective procedure for obtaining optimum i-layers by rf plasma-enhanced chemical vapor deposition (PECVD) for incorporation into the highest performance, highest stability p-i-n and n-i-p solar cells[2,9,10]. In this procedure, the maximum possible H_2-dilution ratio $R=[H_2]/[SiH_4]$ is employed, but without crossing the amorphous-to-(mixed-phase microcrystalline) boundary [a→(a+μc)] that is inevitably encountered above a certain value of R, depending on the other PECVD conditions. Subsequently, it has been found that with this optimization principle, the film microstructure and phase may evolve with thickness and may depend sensitively on the substrate, particularly if the value of R is set too high or the film is grown too thick[2,11]. Because of the possible dependence of the film properties on the accumulated thickness during growth and because of the graded nature of the final film, it is difficult to optimize the deposition procedure by trial-and-error. Under these conditions, real time analysis of film growth is of great utility to the researcher.

In this study, deposition phase diagrams deduced by real time spectroscopic ellipsometry (RTSE) are used as conceptual tools for the optimization of the component layers of a-Si:H-based solar cells. Such phase diagrams are also expected to be useful in the fabrication of the components of μc-Si:H solar cells, since the optimum conditions for these materials are often defined relative to the (a+μc)→μc phase boundary in parameter space[12].

Analysis of the Evolution of (a+μc)-Si:H films

The conventional two-layer [(uniform bulk)/(surface roughness)] optical model used in RTSE data analysis is no longer correct once the film traverses the phase boundary from the single-phase amorphous (protocrystalline) Si:H growth regime into the mixed-phase (a+μc)-Si:H regime. In order to extract the volume fraction of μc-Si:H in the graded mixed-phase regime, it is easiest to track the dielectric function of the top-most growing material throughout the film deposition. This is an ideal application for the virtual interface (VI) approach to RTSE data analysis[13]. Figures 31-33 depict the final results of such an analysis.

---

[9] Y. Lu, S. Kim, M. Gunes, Y. Lee, C.R. Wronski, and R.W. Collins, *Mater. Res. Soc. Symp. Proc.* **336**, 595 (1994).
[10] D.V. Tsu, B.S. Chao, S.R. Ovshinsky, S. Guha, and J. Yang, *Appl. Phys. Lett.* **71**, 1317 (1997).
[11] J. Yang, K. Lord, S. Guha, and S.R. Ovshinsky, *Mater. Res. Soc. Symp. Proc.* **609**, A15.4 (2000).
[12] O. Vetterl, F. Finger, R. Carius, P. Hapke, L. Houben, O. Kluth, A. Lambertz, A. Muck, B. Rech, and H. Wagner, *Sol. Energy Mater. Sol. Cells* **62**, 97 (2000).

[13] H. Fujiwara, J. Koh, C.R. Wronski, and R.W. Collins, *Appl. Phys. Lett.* **70**, 2150 (1997).

Figure 31 compares the (a) real and (b) imaginary parts of the dielectric functions (ε_1, ε_2) for the pure phases obtained in analyses of RTSE data acquired during the deposition of an R=20 Si:H film on a c-Si substrate. This film evolves from single-phase a-Si:H to mixed-phase (a+μc)-Si:H and then to single-phase μc-Si:H throughout growth to 2300 Å in thickness. The dielectric function of the pure a-Si:H phase in Figure 31 was determined by applying the conventional two-layer (uniform bulk)/(roughness) model to analyze the RTSE data collected in the protocrystalline Si:H growth regime $0<d_b<200$ Å, before the onset of the a→(a+μc) transition. The dielectric function of the pure μc-Si:H phase in Figure 31 was obtained from data collected after crystallite contact, i.e., during coalescence ($d_b>1900$ Å). In this latter case, only the top ~200 Å of the film was analyzed, also by applying a two-layer growth model (bulk)/(roughness). In this case, however, the complicated history of the underlying graded layer is buried within a fictitious uniform substrate [or pseudo-substrate] located beneath a fictitious interface [or virtual interface]. The correct surface roughness layer thicknesses -- required in order to extract the (ε_1, ε_2) spectra of Figure 31 -- were determined by applying a global error minimization routine within which the entire VI analysis was embedded. The differences between the two dielectric functions in Figure 31 support an interpretation in terms of phase evolution during film growth. The solid lines in Figure 31 represent best fit analytical models for the two dielectric functions.

Figure 32 shows the evolution of the volume fraction of μc-Si:H in the R=20 film of Figure 31 throughout the growth regime starting from the a→(a+μc) transition and ending near the (a+μc)→μc transition. In the analysis that led to these results, a two-layer VI model similar to that described in the previous paragraph was applied. This model consists of a pseudo-substrate, incorporating the history of graded layer deposition, a ~30 Å thick outerlayer, modeled as a mixture of a-Si:H and μc-Si:H of variable volume fractions $1-f_{\mu c}$ and $f_{\mu c}$, respectively, and a surface roughness layer, modeled as a mixture of the outerlayer material and void with fixed volume fractions of $1-f_{sv}$ and f_{sv}, respectively. The dielectric function of the pseudo-substrate is determined as its pseudo-dielectric function (corrected for surface roughness, but not for the graded structure). The dielectric functions of the two layers are determined from their component volume fractions and dielectric functions via the Bruggeman effective medium theory.

Evidently, the evolution of the surface roughness layer thickness d_s shown in Figure 33(a) for the deposition of Figures 31 and 32 provides higher sensitivity to the presence of microcrystallinity, since it reveals an a→(a+μc) transition at ~300 Å, whereas the μc-Si:H volume fraction in Figure 32 first extends above zero for d_b~700 Å. The solid line in Figure 32 is the result for $f_{\mu c}$ versus d_b established using a cone model of microcrystallite evolution. Figure 33(b) identifies how this microcrystallite cone model is constructed. In this model, it is assumed that all microcrystalline nuclei originate at the a→(a+μc) transition layer thickness [~300 Å, from Figure 33(a)]. The area density of such nuclei is assumed to be N_d, and the nuclei are assumed to grow preferentially at the expense of the surrounding a-Si:H phase with a constant, thickness-independent cone angle, θ. The cones are assumed to be spherically capped whereby the cap radius r evolves with bulk layer thickness according to $r = d_b - d_{b,trans}$. Applying this geometry, N_d and θ can be deduced from the values of $\Delta d_b = d_{b,coal} - d_{b,trans}$ and $\Delta d_s = d_{s,coal} - d_{s,trans}$.

Here, $d_{b,trans}$ and $d_{s,trans}$ are the bulk and surface roughness layer thicknesses at the $a \rightarrow (a+\mu c)$ transition and $d_{b,coal}$ and $d_{s,coal}$ are the corresponding values at the $(a+\mu c) \rightarrow \mu c$ transition. For example, for the deposition of Figures 31-33, values of $\theta = 19°$ and $N_d = 1.1 \times 10^{10}$ cm^{-2} are determined.

Figure 34 presents results for the cone angle θ and the nucleation density N_d plotted as a function of the $a \rightarrow (a+\mu c)$ transition thickness for a series of Si:H films prepared on both c-Si and R=0 a-Si:H substrates under different conditions of H_2-dilution, plasma power, and substrate temperature. Results deduced solely from RTSE using the approach of Figures 31-33 are compared with those from cross-sectional transmission electron microscopy (XTEM) and from atomic force microscopy (AFM). In Figure 34, the solid and open symbols represent results from this work and from Fujiwara et al.[14], respectively. Evidently the nucleation density decreases significantly with increasing $a \rightarrow (a+\mu c)$ transition thickness, yet the crystallite cone angle is nearly constant between 15° and 20°. Figure 34 reveals consistency between the indirect (but real time) optical measurements and the direct (but ex situ) structural measurements, providing strong support for the generality of the cone growth model for microcrystallinity as depicted in Figure 33(b).

SWE Studies on Thin Films

The light induced degradation in a-Si:H is generally associated with the creation of dangling bonds and the emphasis has been on determining their evolution under illumination. Although the neutral dangling bond (D^0) defect density can be directly measured with electron spin resonance the most commonly used method is photoconductive subgap absorption as a function of photon energy, $\alpha(h\upsilon)$. Generally $\alpha(h\upsilon)$ is interpreted solely in terms of, D^0, dangling bond defect states where their densities are directly related to the magnitude, $|\alpha(h\upsilon)|$, typically for $h\upsilon$ 1.1 to 1.3eV. Such an approach has been successfully applied in interpreting a plethora of results on light induced changes as well as the creation and annealing of SWE defects. However, because results have also been reported that point to the presence of other defect states it has become clear that $\alpha(h\upsilon)$ cannot be interpreted in such a simple manner.[15] The approach taken at Penn State is to take into account the contributions to the $\alpha(h\upsilon)$ of multiple defect states by analyzing the evolution of the entire spectra rather than just their magnitude at an arbitrary value.

Any interpretation of $\alpha(h\upsilon)$ in terms of the density and energy distribution of multiple defect states is complicated by the nature of photoconductive subgap absorption, which is determined by N(E), the densities of *electron occupied states and not directly by the total defect density*, N_{def}. Photoconductive subgap absorption is determined from the absorption of photons, which excite electrons into the extended states in the conduction band whose density is then measured as the generated photocurrent. Thus, for any given

[14] H. Fujiwara, Y. Toyoshima, M. Kondo, and A. Matsuda, *Phys. Rev. B* **60**, 13598 (1999)
[15] C. R. Wronski, J. M. Pearce, R. J. Koval, X. Niu, A. S. Ferlauto, J. Koh, and R. W. Collins, *Mat. Res. Soc. Proc.* **715**, A13.4 (2002).

photon energy, α(hυ) is a measure of the number of electrons excited into the conduction band (E_C) which are located within hυ of E_C and is given by [16]:

$$\alpha(h\upsilon) = k(h\upsilon)^{-1} \int N(E)N_{CO}(E+h\upsilon-E_C)^{1/2}dE \quad (1)$$

The integral takes into account that hυ can excite electrons located $E_C - E < h\upsilon$. $N_{CO}(E-E_C)^{1/2}$ is the parabolic distribution of extended states in the conduction band. k depends on the dipole matrix elements for transitions from localized to extended states which can to a good approximation be taken to be constant for the different gap states.[17] In the case of a single type of defect state it is possible to relate N(E) to $N_{def}(E)$ directly because the occupation of these states is constrained by charge neutrality. However, in the case of multiple defect states the electron occupation of each type of state is *determined by the kinetics of carrier recombination* and thus depends not only on their energy distribution in the gap but also on their relative densities and carrier capture cross-sections of the states.[18] Despite these complexities, information can be obtained about the evolution of the light induced defects and in particular their energy distributions. In order to relate α(hυ), which includes the contributions from all the electron occupied states at energies within hυ from E_C, to the energies of the defect states relative to E_C it is necessary to take the derivative of the α(hυ) spectra. In the case when N(E) change rapidly with E, relative to $N_{CO}(E-E_C)^{1/2}$, the effect of the latter on the joint density of states is small. Consequently, the derivative of equation 1 yields:

$$kN(E) = (h\upsilon)d[\alpha(h\upsilon)]/dE - \alpha(h\upsilon) \quad (2)$$

One way of characterizing the evolution in light induced gap states is to evaluate the percent changes obtained by normalizing kN(E) after degradation to that in the annealed state which yields:

$$P(E) = kN_{DS}(E)/kN_{AS}(E) = N_{DS}(E)/N_{AS}(E) \quad (3)$$

A clearer picture of such evolution of the different light induced gap states can be obtained by characterizing the changes in the defect states through the difference between the kN(E) spectra in a degraded state and that in the annealed state. This difference, Z(E), is given by:

$$Z(E) = kN_{DS}(E) - kN_{AS}(E) = k\,[N_{DS}(E) - N_{AS}(E)] \quad (4)$$

---

[16] J. M. Pearce, J. Deng, V. Vlahos, R. W. Collins, and C. R. Wronski, *Proceedings of the 3rd World Conference on Photovoltaic Energy Conversion*, (in press).

[17] W.B. Jackson, S.M. Kelso, C.C. Tsai, J.W. Allen, and S.J. Oh, *Phys. Rev. B* **31**, 5187 (1985).

[18] A. Rose, "Concepts in Photoconductivities and Allied Problems," Robert. E. Kreiger Pub.: New York, 1978.

Whereas, the P(E) spectra readily provide a fingerprint of at which energies the largest changes occur in the electron occupied defect states[19], the Z(E) spectra provide a more direct method of evaluating increases in the densities of the different light induced gap states.

In the studies of α(E) spectra at Penn State the nature of gap states in a-Si:H films was determined using a numerical model, SAM. With SAM experimental results on electron mobility-lifetime products over a wide range of generation rates and α(E) were self-consistently fit using the same "operational" parameters. SAM includes equation 2. Results were obtained that showed that self-consistent fitting can only be achieved in the presence of different gap states. However, there are still many unanswered questions regarding their nature because of the number of unknown and adjustable parameters that are needed to describe these states in the simulations.

In order to experimentally characterize N(E) in any meaningful way it is critical to obtain α(E) spectra with both high accuracy as well as spectral resolution. The construction of a new dual beam photoconductivity (DBP) apparatus, which overcomes several deficiencies of the past one at Penn State, was completed in the last quarter of this phase. Among the key improvements are:

- The range in the spectra of α(E) was extended to 0.5eV. Currently, the signal to noise ratio from 0.5eV to ~ 0.65eV is too low for α(E) to be considered reliable. However, the new DBP apparatus does increase the reliable range from 0.9eV to 0.7eV.
- The computer automation, improved signal to noise, and coupling to the lock-in amplifier, enables the α(E) to be obtained consistently in under 30 minutes.
- Improved data acquisition and monochromator resolution allows high resolution α(E) spectra to be obtained for reliable analysis of derivatives.
- It allows electron μτ products to be measured.
- It allows in-situ controlled light soaking of films.
- It enables the quasi-Fermi level splitting to be accurately controlled. This allows α(E) spectra to be obtained with known quasi-Fermi splitting as well as maintaining them constant during degradation. With bias illumination at constant generation rates, as used in the past, this splitting decreases due to higher recombination and adds a variable in the measurement of the α(E) spectra.

A schematic of this new DBP apparatus is shown in Figure 35.

The correct way of analyzing α(E) spectra was applied to the results obtained with the original DBP apparatus lacking the capabilities outlined above. The limitations on the accuracy of these spectra seriously limited the ability of obtaining reliable Z(E) spectra. Nevertheless the P(E) spectra could be used to both establish the presence of two distinctly different light induced gap states at and below midgap. They also showed that the kinetics in their evolution is not only different but that it also depends on the microstructure of the a-Si:H material.

[19] J. M. Pearce, J. Deng, R. W. Collins, and C. R. Wronski, *Appl. Phys. Lett.*, **83** (18), pp. 3725-3727, 2003.

Studies were carried out on the measurement capabilities of the new DBP system as well as experimental procedures to ensure the reproducibility and accuracy of the measurements and their results. Included in this was a new method of applying the Fourier transforms for eliminating the interference fringes in the α(E) spectra. As in the case of the T&R spectra there are fringes in the subgap region from multiple reflections in the thin film. In order to eliminate these fringes, a Fast Fourier Transform (FFT) is used to filter the higher order frequency components. The method developed by Wiedeman, Bennett and Newton for removing the interference fringes in PDS spectra was utilized here.[20] The FFT algorithm assumes that the input signal is periodic, so the rapid transitions must exist at the start and endpoints to reach a common baseline. This normally distorts α(E) analysis because the start and endpoints are separated by several orders of magnitude. The problem associated with the signal endpoints was circumvented by reflecting the log of the absorption vs photon energy signal about the vertical axis at the start of the signal to give a common baseline to both of the endpoints. The Fourier transform is then taken and the cutoff frequency (1/eV) is established to eliminate the noise component of the signal associated with the multiple reflections by trial and error. After filtering out the noise component the reverse Fourier transformation is taken and the true α(E) signal is obtained with only the first quadrant being saved. The results obtained for α(E) for an R=10 film in the annealed state is shown in Figure 36, which shows the α(E) spectrum and the corresponding kN(E) results with and without inclusion of the α(E) term in equation 2. It can be clearly seen that there is only a minimal contribution to kN(E) by the α(E) term, on the order of a few percent, which is also the case after light induced degradation.

Relaxation of Light Induced Changes at 25^{o}C after 1 sun Illumination

In the numerous studies on a-Si:H films and cells with 1 sun illumination no evidence for recoveries in light induced changes at 25˚C have been reported. The absence of this was expected since the studies with high intensities indicated that there would be far less 'fast' defect states created with 1 sun illumination than with high intensity illumination. The observed presence of the significant thermal annealing of light induced defect states at room temperature after 1 sun illumination, obtained in the studies on solar cells as discussed in Task 3, triggered a *careful* study on a-Si:H thin films. Results were obtained on the kinetics of the photocurrent recoveries after degradation with 1 sun illumination at 25˚C, which are in excellent agreement with the results on cells. These results are the first direct observations of room temperature annealing in photoconductivity measurements after 1 sun illumination since SWE was discovered almost 30 years ago.

The thin film structures were deposited with truly Ohmic n+ a-Si:H rather than metal evaporated contacts which yield Ohmic photocurrents over a wide range of voltages. This included the annealed state which is not the case with metal contacts. The 1 sun degradation at 25˚C and recovery of the photocurrent corresponding to a very low generation rate (G) of 5 x 10^{15}cm^{-3}s^{-1}, and small quasi-Fermi level splitting, is shown in

[20] Wiedeman, S., Bennett, M. S., and Newton, J. L., *Mater. Res. Soc. Symp. Proc.* 95, pp. 145-150 (1987).

Figure 37 for a 0.8μm R=10 film. Using these low G values, and small quasi-Fermi level splitting, the rate of recoveries was shown to be within experimental error for continuous illumination with a G = 5 x $10^{15}cm^{-3}s^{-1}$ and intermittent monitoring of dark thermal anneal at 25˚C. It can be seen in Figure 37 that after the large initial decrease in the photocurrent, the fast changes similar to those observed by Jiao et al.[21], there is a continuous decrease, until the protocrystalline material reaches a DSS after 100 hours. Immediately upon the removal of the 1 sun illumination in this DSS there is a recovery in the photocurrent. This recovery is quite rapid, where it can be seen in Figure 37 that after only an hour the photocurrent recovers to a value equal to that obtained after degradation for ~2 hours (as indicated by the arrow). Thus, this hour of relaxation at 25˚C effectively "erases" the effects of the creation of defects which took over 90 hours of 1 sun light soaking to create. This is a striking and quite unexpected result in view of the extensive studies carried out on light induced changes and SWE. It should also be pointed out here that this relaxation is completely erased with 1 sun illumination for only ~20 seconds.

This room temperature annealing phenomenon is not limited to the DSS in both R=10 and R=0 materials. It is also observed at all times during the room temperature 1 sun degradation and is as illustrated in Figure 38 for a R=10 film. In Figure 38 the normalized photocurrents (i.e. the photocurrent during relaxation divided by the initial values obtained after ceasing 1 sun illumination) are shown for illumination times of 1 minute, 2 hours, and 24 hours. It can be clearly seen that as the light soaking time increases the rate of relaxation, measured as a percent of the degraded state photocurrent, decreases as is highlighted by the arrow in the figure. These results are in agreement with earlier results on similar cells and films after 10 sun illuminations to a DSS at 50^{o}C and subsequent "annealing" at room temperature which showed that the defect states that are created faster also anneal out faster[22].

The results shown in Figure 37 and 32 utilize a generation rate of $5x10^{15}$ $cm^{-3}s^{-1}$ where the Fermi level is estimated to be close to 0.7eV from E_c or 0.2eV from midgap. It is found that with these generation rates the low carrier recombination introduced by the low G has minimal perturbation on the relaxation solely from thermal annealing. Higher carrier generation rates cannot be used in reliably characterizing relaxation in terms of such a thermal annealing process because as the carrier recombination is increased the recombination begins to create defects at a faster rate than those being annealed out as indicated by the results discussed in Task 3. Consequently, such creation of light induced defects with carrier generation rates that are very much smaller than those at 1 sun illumination limits the ability of both detecting and characterizing the nature of the relaxation. This is illustrated in Figure 39, where results with photocurrents of G = 5 x $10^{17}cm^{-3}s^{-1}$ and G = 5 x $10^{18}cm^{-3}s^{-1}$ are shown for the R=10 sample normalized to that obtained immediately after degradation of 1 sun illumination for 2 hours at 25˚C. At these generation rates much smaller than that corresponding to that of 1 sun illumination there is already erasure of any photocurrent recovery. The observation that as the generation rate decreases the relaxation erasure also decreases can thus be attributed to a competition between the thermal annealing and the additional creation of defect states by

[21] Jiao, L., Liu, H., Semoushikina, S., Lee, Y., Wronski, C.R., *Appl. Phys. Lett*., **69**, p. 3713 (1996).
[22] J. M. Pearce, R. J. Koval, X. Niu, S. J. May, R.W. Collins, and C. R. Wronski, *17th European Photovoltaic Solar Energy Conference Proceedings,* **3**, pp. 2842-2845, 2002.

the recombination of photo-generated carriers. As the illumination intensity approaches 1 sun the recovery erasure becomes extremely rapid. It should be noted here, however, that at higher generation rates not only is the carrier recombination increased but also the splitting of the quasi-Fermi levels so that additional states are introduced.

A clear confirmation of the nature of this room temperature 1 sun relaxation observed with the photocurrent measurements just discussed is obtained from the comparison of these results with those obtained for the dark forward-bias I-V characteristics of a solar cell with the same a-Si:H as the i-layer. A comparison is made in Figure 40 between the results obtained for the relaxation in the photocurrent with G = $5x10^{15}cm^{-3}s^{-1}$ and the recombination currents measured at 0.4V forward bias. Since the photocurrents changed by only a factor of 3, there was negligible change in the quasi-Fermi level splitting around 0.4eV. Figure 40 shows the relaxation in the dark current at 0.4V (right axis) as a function of time in a p-i-n solar cell with a 200Å R=40 p/i interface and 3,800Å R=10 i-layer 25°C after 30 minutes of 1sun illumination at 25°C. In this solar cell the thermal annealing of defect states near midgap manifests itself directly in the decreased Shockley-Read-Hall recombination in the i-layer. Because the photocurrents are inversely proportional to the densities of the defect states acting as recombination centers[23], a comparison is made with their inverse to characterize the changes in defect states acting as recombination centers. Accordingly, the inverse of the photocurrents after 30 minutes of 1 sun illumination are also plotted as a function of time in Figure 40 (left axis). A striking similarity between the two results can be clearly seen in the relaxation kinetics which establishes the same phenomenon. It also points to that the results on films with photocurrents under such low illumination levels are also characterizing thermal relaxation. It should be pointed out here that the percent change seen in the cells and the film in Figure 40 is not the same due to a lower quasi-Fermi level splitting in the film.

This newly discovered relaxation in the light induced defect states located near midgap has important implications not only in understanding the nature of these states but also on the results reported in the extensive studies carried out on SWE at 25˚C in which such relaxation was not taken into account. Measurements which are not carried out at the same time even after 1-sun light exposures are characterizing different light induced defect state distributions. For example, this can readily occur in attempting to obtain direct correlations between the subgap absorption spectra measured directly after light soaking and subsequent ESR measurements carried out after a prolonged delay.

In the α(E) studies being carried out on the light induced defects this relaxation is taken into account. Results have been obtained where the contributions of annealing out of defect studies is observed and is being carefully investigated. This and other studies on light induced defects are being carried out in close collaboration with the University of Utah.

[23] Rose, A., "Concepts in Photoconductivity and Allied Problems", (Interscience, New York, 1962).

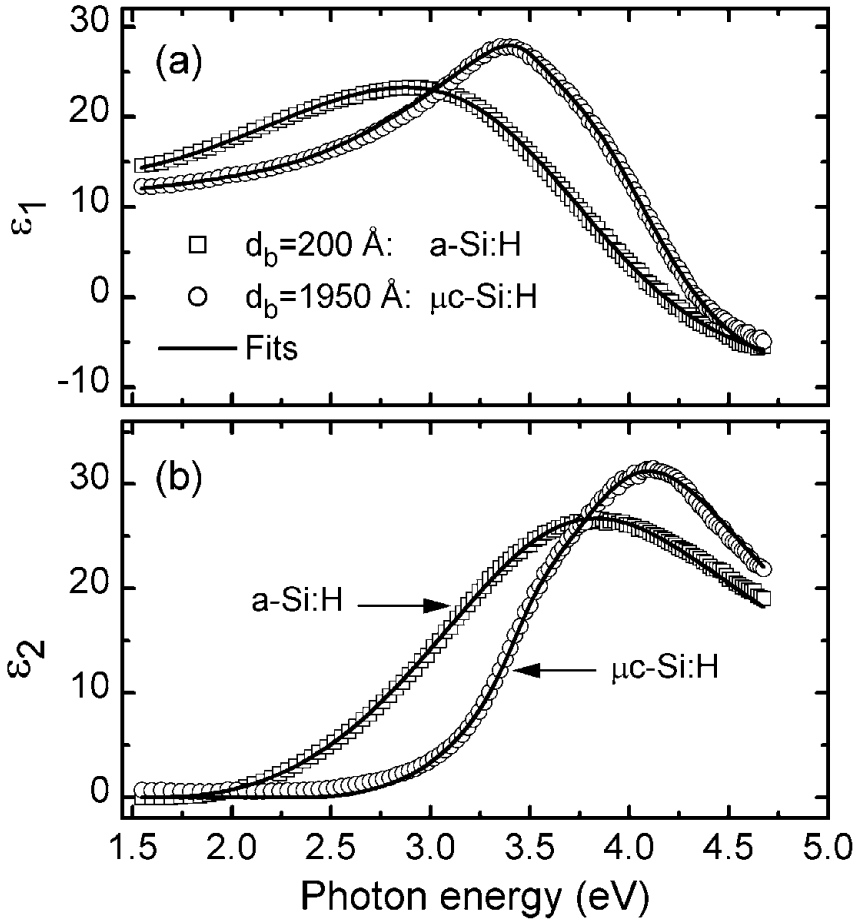
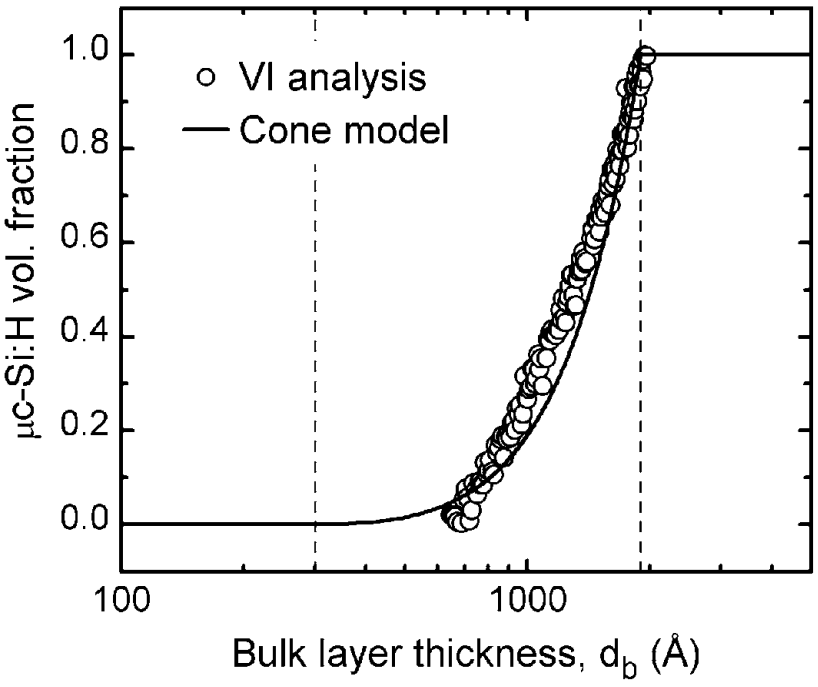


Figure 31: (a) Real and (b) imaginary parts of the dielectric functions of the pure phases for an R=20 Si:H deposition on c-Si. The solid lines are fits using analytical models for the dielectric functions.



:

Figure 32: Depth profile in the volume fraction of the microcrystalline phase throughout the mixed-phase (a+μc)-Si:H growth regime for the R=20 Si:H deposition on c-Si from Fig. 27 (points). In order to extract the volume fraction of μc-Si:H, the dielectric function of the top-most growing material was tracked throughout the film deposition. Also shown as the solid line is the prediction of the microcrystallite cone growth model depicted in Figure 27.

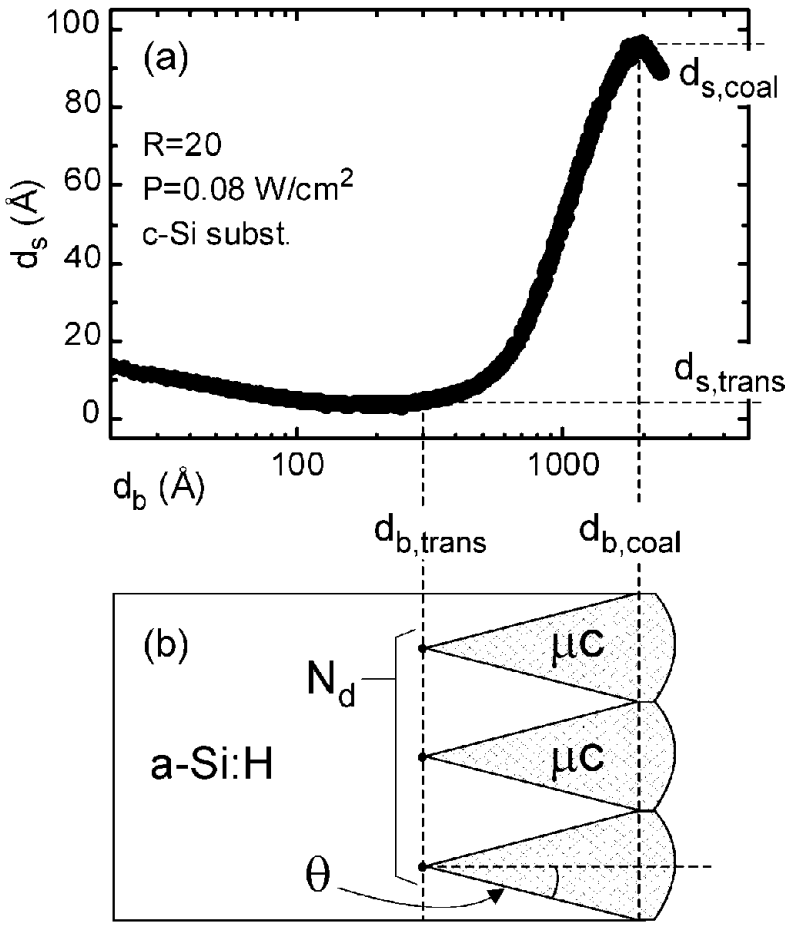


Figure 33: (a) Surface roughness thickness versus bulk layer thickness for the R=20 Si:H deposition of Figs. 31 and 32; (b) schematic of the cone growth model used to estimate the microcrystallite nuclei density and cone angle.

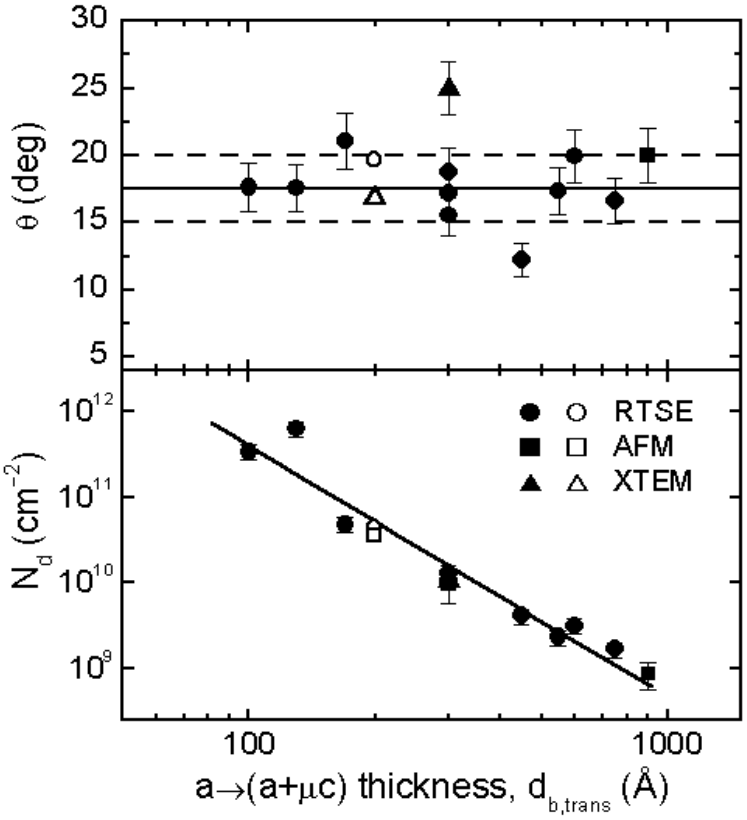


Figure 34: Cone angle θ (top panel) and nucleation density N_d (bottom panel) versus the a→(a+μc) transition thickness $d_{b,trans}$ for Si:H films deposited under different conditions on both c-Si wafers and R=0 a-Si:H. The values for θ and N_d are deduced from RTSE (circles), XTEM (triangles) and AFM (squares).

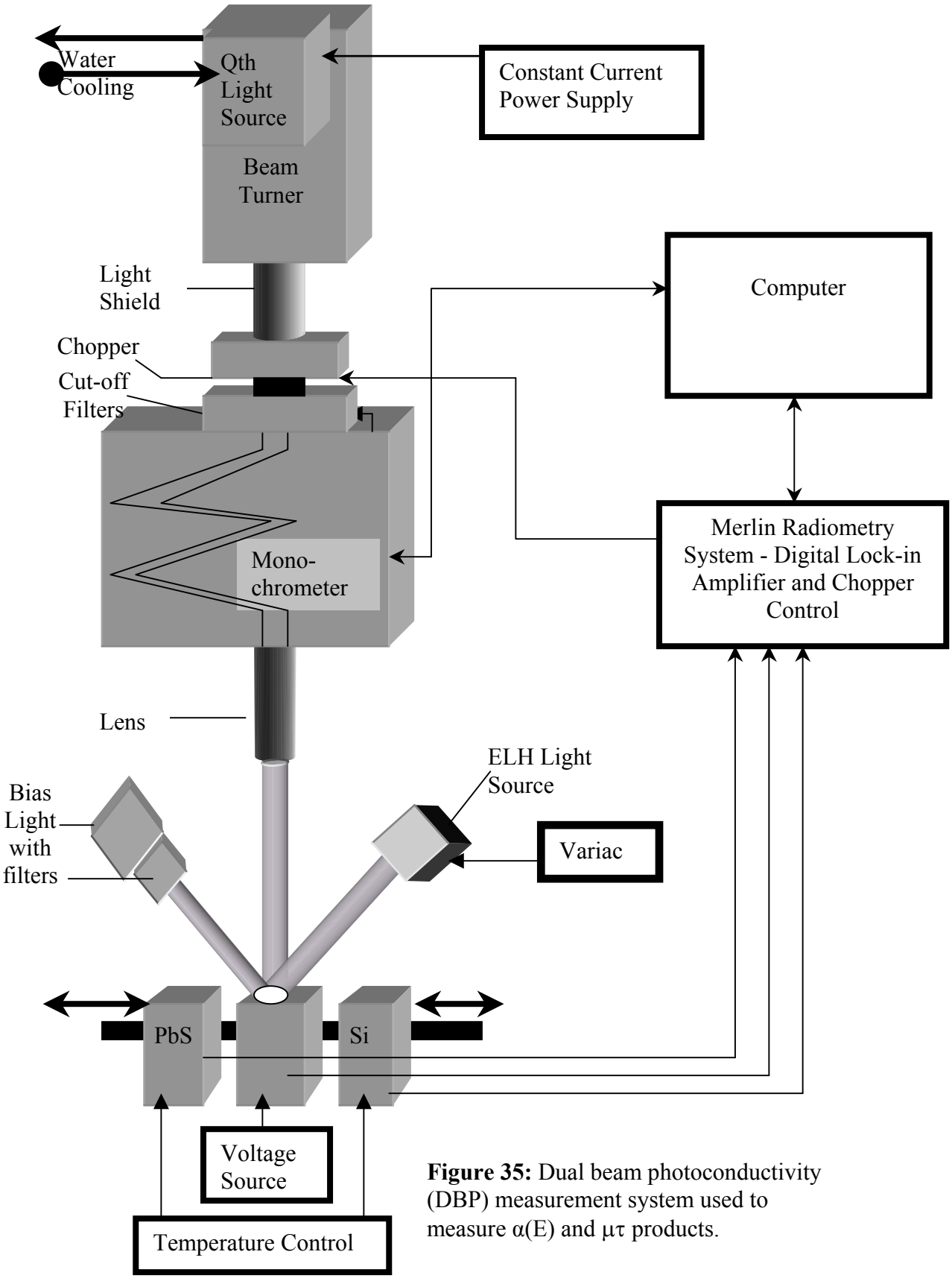


Figure 35: Dual beam photoconductivity (DBP) measurement system used to measure $\alpha(E)$ and $\mu\tau$ products.

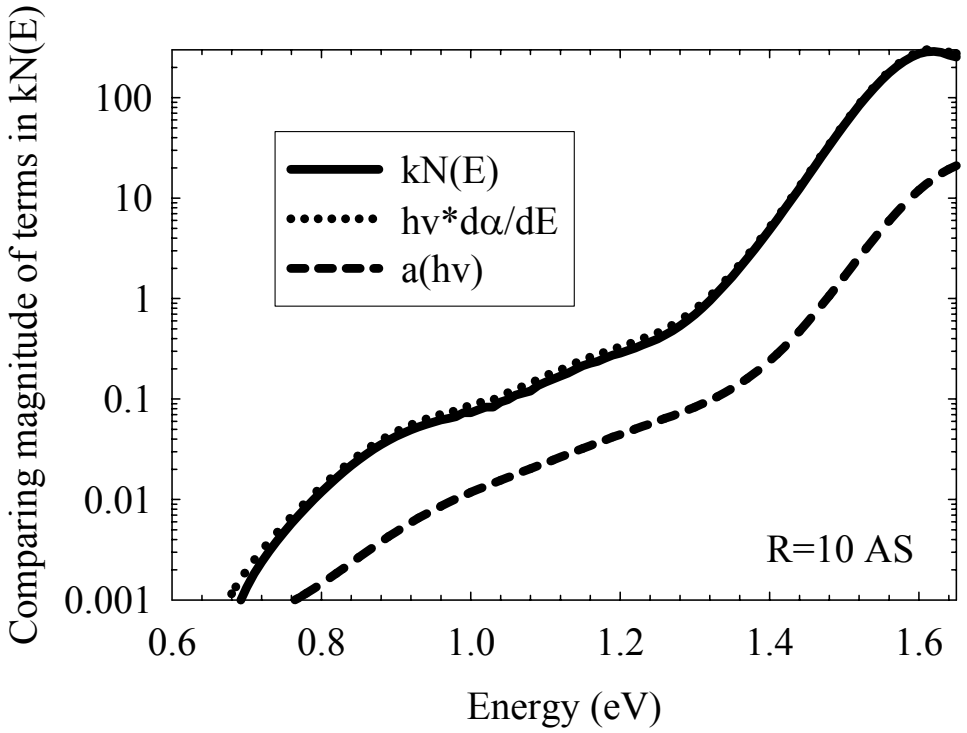


Figure 36: kN(E), hυ*dα/dE, and α(hυ) for an R=10 0.8μm a-Si:H thin film in the annealed state.

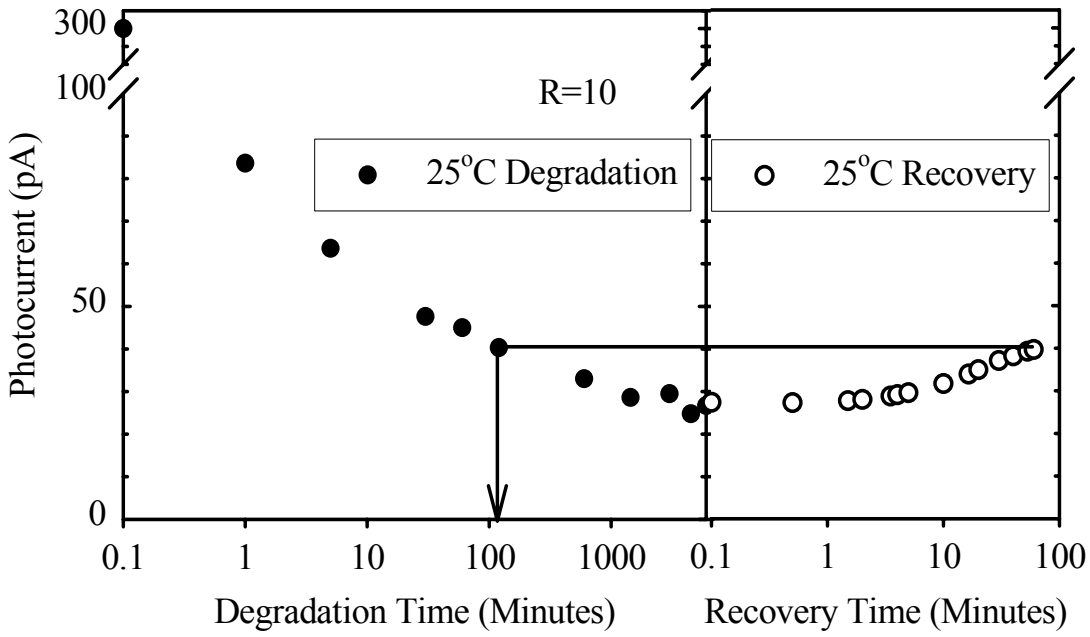


Figure 37: Photocurrent kinetics of degradation for 100 hours and recovery for one hour of an 0.8μm R=10 film at 25°C.

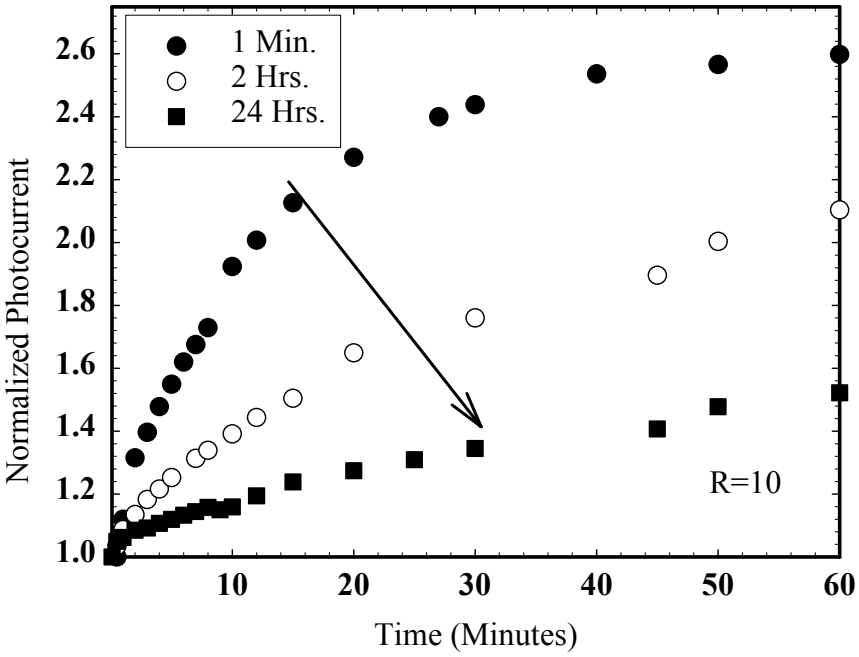


Figure 38: Normalized photocurrent vs. room temperature relaxation time in minutes for a R=10 film degraded under 1 sun illumination at 25°C for 1minute, 2hours, and 24 hours.

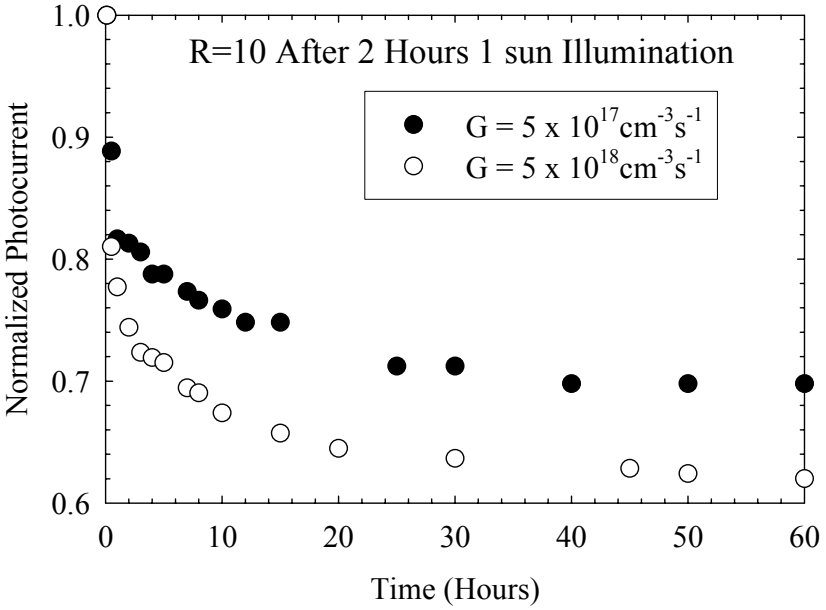


Figure 39: Photocurrent normalized to the 1 sun 25˚C degraded state after 2 hours. The recovery erasure is shown for G = 5 x 10^{17}cm^{-3}s^{-1} and G = 5 x 10^{18}cm^{-3}s^{-1} as a function of time.

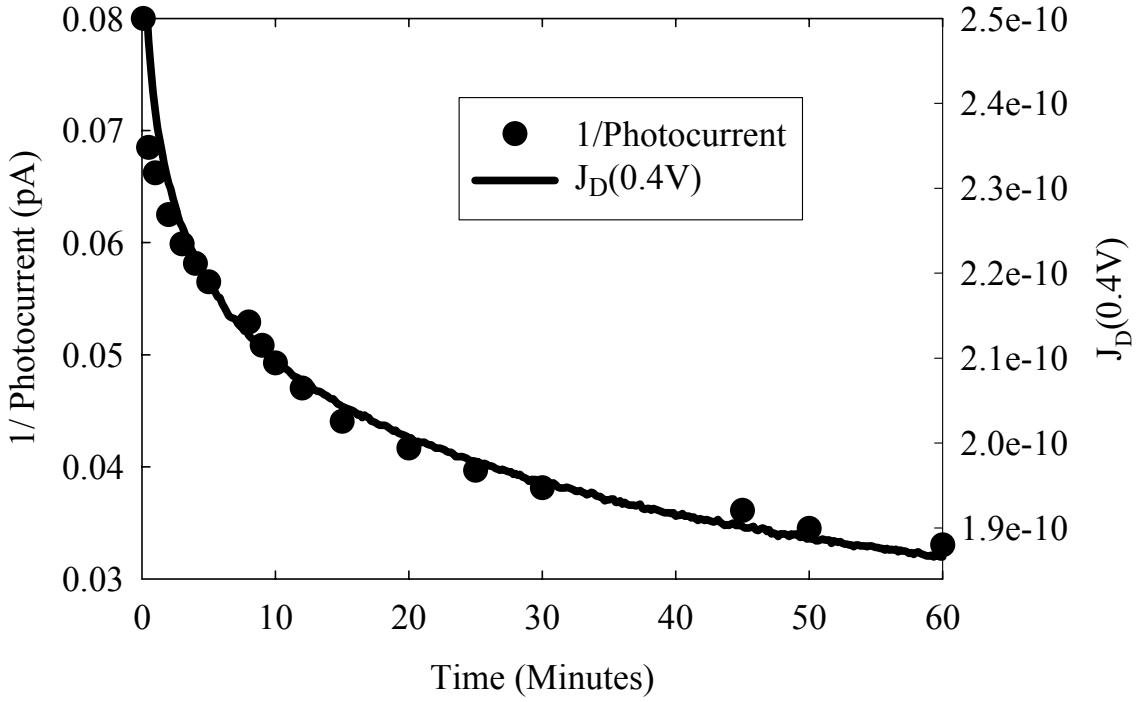


Figure 40: The dark current at 0.4V relaxation at 25°C after 30 minutes of 1sun illumination at 25°C of a p-i-n solar cell with a 200Å R=40 p/i interface and 3,800Å R=10 i-layer on the right axis. One over photocurrent relaxation for a 0.8μm R=10 film under identical degradation and relaxation conditions on the left axis.

APPENDIX A

Theoretical Considerations

The experimental results previously reported (April Report 2003) showed that that there are no large densities of defect states in i-layers adjacent to p, n contacts such as predicted by the defect pool model but instead the distributions of the defects are relatively homogeneous across the bulk. This conclusion greatly facilitates the analysis of the experimental results and serves as a fundamental basis for the correct understanding of the physical mechanisms governing the operation of a-Si:H solar cells.

From the J_D-V characteristics it was clearly seen that extended voltage regions exist in which the currents increase exponentially with the applied forward bias voltages, consistent with the diffusion/recombination model proposed by Lips et al[24]. Furthermore, it has been shown that these currents increase when the density of defects is increased by light induced degradation, which indicates that the recombination process is governed by Shockley-Reed-Hall (SRH) recombination mechanisms in which electrons and holes recombine through the defect states in the gap[25].

The current transport in the dark of these a-Si:H solar cells over an large range of forward bias voltages can be considered in terms of the diffusion of the electrons and holes into the bulk under the forward bias and recombination through gap states which have a relatively homogeneous distribution across the bulk. The recombination rate given by SRH theory is determined by the product of the electron and hole concentrations, n and p respectively, which can be expressed as:

$$r=np/(sn+p)\tau_{no} \qquad (A1)$$

where s is the ratio of the electron to hole capture cross sections and τ_{no} is the electron capture time determined by the density of gap states that act as recombination centers. To facilitate the discussion but without losing generality, an equal electron and hole capture cross section (s=1) is assumed in the following discussion.

Even though the recombination occurring at the p/i interfaces and in the bulk are both described by the SRH recombination mechanism, their contributions to the diode quality factor of the dark current characteristics are distinctly different. Let us first consider the recombination in the bulk. When the carrier transport is diffusive, the concentrations of the electrons and holes in the bulk have an exponential (negative) dependence on the potential difference relative to n and p contacts, respectively. The further away from their respective contacts, the higher potential difference so that these carrier contractions decay exponentially away from their contacts. Under forward bias, the potential difference is reduced across the bulk so that the carrier concentrations increase exponentially. Although n and p both vary rapidly across the bulk, their product is constant and:

$$np=n_i^2\exp(qV/kT) \qquad (A2)$$

[24] K. Lips, Mat. Res. *Soc. Symp. Proc*. **377**, 455 (1995).
[25] W. Shockley and W. T. Read, *Phys. Rev*. **87**, 835 (1952).

where n_i is the intrinsic carrier concentration, determined by the band gap, q the electron charge, k the Boltzman constant, T the temperature and V the applied forward bias voltage.

In the case of a single defect in the mid gap, τ_{no} is a constant. Then according to equation A1, the maximum recombination rate occurs at the location where n+p is the minimum which is achieved only when n=p. At this location, from equation A2, it can be easily obtained that:

$$n=p=n_i\exp(qV/2kT) \tag{A3}$$

Away from this location in the bulk, either n or p increases rapidly so that the recombination rate decreases rapidly resulting in a recombination profile, which has sharp slopes around its center. Combining equation A1 and A3 the maximum recombination rate r_{max} can be obtained:

$$r_{max}=n_i\exp(qV/2kT)/\tau_{n0} \tag{A4}$$

The total recombination current can be obtained by either integrating r across the bulk or equivalently by multiplying r_{max} by the width of the recombination profile. It has been shown that this width is proportional to the local field ε around the center of the recombination profile so the dark current J_D has the form[26]:

$$J_D \sim (1/\varepsilon)n_i\exp(qV/2kT)/\tau_{n0} \tag{A5}$$

Due to the fact that in these a-Si:H cells the n contact is more heavily doped than the p contact, the location where n=p is closer to the p contact. As will be discussed in more detail, the n, p contacts induce a space charge region in the i-layer adjacent to them so that the electric filed ε in the bulk does not scale exactly with the bulk i-layer thickness, neither does J_D. This conclusion has been utilized earlier in explaining the thickness dependence of the J_D-V characteristics. More importantly, since ε is not a fast-varying function of V, equation A5 yields a diode quality factor of 2, which has been well established in the case of crystalline-Si p-n junctions at low forward bias when the recombination in the space charge regions dominates the total current.

In the case of a-Si:H i-layers which have a continuous distribution of gap states between valence band and conduction band, however, τ_{no} is no longer a constant. In SRH type recombination, the gap states that act as recombination centers are those located between the electron and hole quasi-Fermi levels, F_n and F_p respectively, where the separation is equal to the applied voltage. As the applied voltage and the splitting of the quasi-Fermi levels are increased there is a corresponding continuous increase in the number of gap states acting as recombination centers[17], which leads to a decrease in τ_{no} and a corresponding increase in the recombination. In the case of a distribution of states increasing exponentially around mid-gap the increase in the number of recombination centers enhances the current by an exponential term, which then changes the diode quality factor from 2 to a lower value whose offset depends on the specific exponential

[26] C. van Berkel, M. J. Powell, A. R. Franklin, and I. D. French, *J. Appl. Phys*. **73**, 5264 (1993).

form in the energy distribution of the gap states. This has been confirmed both numerically by Hack and Shur[27] and analytically by Berkel et al.[19]. Thus, an effective diode quality factor m of 1.4 to 1.6 seen over an extended voltage region in the J_D–V characteristics of the cells with minimized p/i interface recombination[28], can be explained with just the presence of a continuous distribution of gap states in the a-Si:H i layer. There is therefore no necessity, as has been previously suggested[29], for a spatially varying density of defects in the i-layer predicted by the defect pool model.

However, in the case of a gap state distribution which is significantly different from an exponential form, $d(\ln(J_D))/dV$ does not remain constant so that the diode quality factor changes with the applied voltage. Consequently, there is a voltage dependent differential diode quality factor n(V), which is equal to the inverse of $[kT/q][d(\ln(J_D))/dV]$. In the results obtained for cells having either diluted or undiluted i-layers, where the recombination is dominated by that in the bulk of the i-layers, values of n(V) are present which are approximately constant over an extended region of voltage. This indicates that the distributions of the gap states around mid-gap are similar, although not identical, to that of an exponential form such as the Gaussian distributions suggested by the studies on the corresponding thin film i-layers[30]. It can be pointed out here also that the difference in such n(V) values obtained between the two types of cells is a clear indication of a difference in the energy distribution of the gap states in their respective i-layers.

In the case of recombination at the p/i interface, the concentration of holes adjacent to the p-contact is much larger than that of the electrons and the electrons become the minority carriers. Thus, from equation A1, the recombination rate is determined only by the electron concentration at the p/i interface. The electron concentration n at p/i interface is an exponential function of the applied forward bias voltage V so that the recombination rate at p/i interface is given by:

$$r_{pi}=n/\tau_{npi}=n_{0pi}\exp(qV/kT)/\tau_{npi} \qquad (A6)$$

where n_{0pi} is the electron concentration at the p/i interface in equilibrium and τ_{npi} is the electron capture time at the p/i interface, which is usually smaller than that in the bulk. It should be noted here that n_{0pi} can be controlled by changing the band gap of the p/i interface layers as has been carried out for controlling p/i recombination in the cells studied. The corresponding dark currents can be obtained either by summing up all the recombination in the thin regions adjacent to the p/i interface or by introducing an effective interface recombination velocity, S_{eff}, which gives:

$$J_D=qnS_{eff}=qS_{eff}\, n_{0pi}\exp(qV/kT) \qquad (A7)$$

[27] M. Hack and M. Shur, *J. Appl. Phys*. **54**, 5858 (1983).
[28] J. Deng, J.M. Pearce, R.J. Koval, V. Vlahos, R.W. Collins and C.R. Wronski, *Appl. Phys. Lett.* **82**, 3023 (2003).
[29] M.A. Kroon and R.A.C.M.M. van Swaaij, *J. Appl. Phys*. **90**, 994 (2001).
[30] L. Jiao, Ph.D. Thesis, The Pennsylvania State University, 1999.

Thus, in the case of interface recombination dominated currents, the effective diode quality factors such as m* are close to one[31]. By comparing equation A7 with equation A5, it can be seen that the increase with voltage in the interface recombination currents is much faster than that of the bulk recombination currents. It is therefore not surprising that at the higher bias voltages the p/i interface recombination can readily dominate over the bulk recombination.

To simplify the above discussion, the effects of the space charge that is present in the bulk on the current transport are not considered here. This space charge consists mainly of the trapped electrons and holes, the concentrations of which are higher than those of the free electrons and holes even in the highest quality a-Si:H solar cells. The densities of trapped electrons and holes depend on the positions of electron and hole quasi-Fermi level, respectively. These in turn are determined by the free electron and free hole concentrations where the higher free carrier concentration, the higher the trapped carrier concentration of the corresponding carriers. The presence of the space charge in i-layers affects the electric field distribution across the bulk. Due to the high electron (n_0) and hole concentrations (p_0) in the regions of i-layer adjacent to the n and p contacts, respectively, the space charge densities in these regions are higher than in the bulk. This results in potential drops V_n near the n and V_p near the p contact, which constitute barriers for the injection of carriers from the contacts into the bulk of the i-layer. These potential barriers are included in the schematic band diagram for a p-i-n cell under a forward bias V shown in Figure A.1. In the figure, ϕ represents the potential drop across the bulk region and $\phi=V_{bi}-V-V_n-V_p$, where V_{bi} is the buit-in voltage across the cell. Positive values of ϕ indicate that the carrier transport is diffusive while negative values indicate that the transport is drift-driven as shown by Lips[17] . In a-Si:H solar cells with low defect densities in their intrinsic layers both V_n and V_p are quite small so that ϕ remains positive for biases V up to values close to V_{bi}. This results in the exponential dependence of the diffusive current J_D on V over an extended voltage range so that direct correlations of J_D-V characteristics can be made with bulk dominated recombination and consequently the densities of gap states in the intrinsic layers.

The transport of photo-generated carriers is distinctly different from that of those injected from the contacts since with volume-absorbed light the carriers are created throughout the bulk of the i-layer. They are subject to a drift field, ε, which sweeps them out towards the contacts as a net drift current[32]. In i-layers with low defect densities the space charge that is present has only a small effect on the electric field distribution so that $\varepsilon\cong\phi/L$ where ϕ is the potential drop across the bulk of the i-layer and L its thickness. The photo-current J_L is then determined by the densities of electrons and holes that reach the contacts before recombining, where the probability of undergoing recombination depends on their effective lifetime, τ, and transit time T_{tr}. This current J_L can be written as $J_L=J_G-J_{RG}$ where J_G is the photocurrent created by the generation rate of carriers, G, due to the absorbed photons in the bulk. J_{RG} is the recombination current in the bulk which is determined by T_{tr} and τ. J_G depends only on the intensity of the illumination and is independent on the electric field ε (V) while J_{RG} depends on ε since $T_{tr}\propto 1/\varepsilon$. Under short

[31] J. Deng, J.M. Pearce, R.J. Koval, V. Vlahos, R.W. Collins and C.R. Wronski, *Appl. Phys. Lett.* **82**, 3023 (2003).
[32] D.E. Carlson and C.R. Wronski, *Appl. Phys. Lett.*, **28**, 671 (1976).

circuit conditions the effective transit time $T_{tr} \propto 1/V_{bi}$. In high quality a-Si:H cells J_{RG} is significantly lower than J_G which is reflected by the quantum efficiencies under short circuit conditions of virtually 100% for carriers generated in the bulk. For $J_{RG} << J_G$, $J_{SC} \cong J_G$ which makes J_{SC} directly proportional to the illumination intensity as is observed in high quality cells.

Under a forward bias V across the i-layer, T_{tr} increases as does J_{RG}. At the same time the balance between the drift and diffusive currents from the high densities of n_0, p_0 carriers is disturbed so that the net diffusion currents, J_{diff}, are introduced in the opposite direction to the photo-generated currents, as is illustrated in Figure A.2. J_L then becomes:

$$J_L(V) = J_G - J_{RG}(V) - J_{diff}(V) \tag{A8}$$

Since the mechanism governing this J_{diff} is exactly the same as that for the diffusion current J_D in the dark, as discussed earlier, they increase exponentially with V. For the same diffusive transport under illumination as that in the dark, $J_{diff}(V) = J_D(V)$. Since both J_{RG} and J_{diff} increase with V, J_L decreases until it becomes zero at $V = V_{OC}$, so under open circuit conditions:

$$J_{SC} \cong J_G = J_{RG}(V_{OC}) + J_{diff}(V_{OC}) \tag{A9}$$

which for $J_{diff} >> J_{RG}$ becomes:

$$J_{SC} \cong J_{diff}(V = V_{OC}) = J_D(V = V_{OC}) \tag{A10}$$

At high current densities and forward bias, there are clear deviations from the exponential dependence on V in the dark current. This occurs when V_{bi}-V approaches $V_n + V_p$, which corresponds to ϕ approaching zero. Further increases in V invert the field across the i-layer, which then results in the field driven drift currents[17]. In addition, at high values of J_D the potential barriers associated with V_n and V_p begin to limit the carrier injection from the contacts into the i-layer[33]. The height of these barriers depends on the space charge, which in turn is determined by n_0, p_0 and the defect densities in the i-layers, which are small in high quality intrinsic materials. As a consequence, the effects of V_n, V_p do not become significant until current levels are very high. However, in low quality cells, where these barriers are high due to a large density of defects, their effects already become significant at lower current levels.

As a consequence there is the superposition reported between J_{SC} versus V_{OC} and J_D versus V. This occurs even though the superposition principle is not valid in a-Si:H solar cells for *all* values of V due to the voltage dependent contributions of J_{RG} to J_L.

The absence of superposition between J_{SC}-V_{OC} and J_D-V, however, also occurs if at $V = V_{OC}$, J_{RG} is comparable to or larger than J_{diff}. This can occur at high illumination levels when V_{OC} approaches V_{bi} so that the small values of ϕ and hence ε present across the bulk result in $T_{tr} > \tau$ which lead to large values of J_{RG}. At the same time the high forward bias currents in the J_D-V characteristics encounter limitations on carrier injection imposed by the potential barriers V_n and V_p. Both of these effects can then contribute to a

[33] F.A. Rubinelli, J.K. Arch, and S.J. Fonash, *J. Appl. Phys*. **72**, 1621 (1992).

split between the two characteristics since the limitations of J_{RG} on V_{OC} move the J_{SC}-V_{OC} to lower values of V_{OC}, while on the other hand the limitations on carrier injection move J_D-V to higher values of V. Higher densities of defects in the i-layer result in larger values of J_{RG} as well as V_n, V_p at the n and p contacts so that the divergence between the J_{SC}-V_{OC} and J_D-V characteristics occurs at lower voltages.

As was discussed earlier the potential barriers that limit the carrier injection are determined by both n_0, p_0 as well as the densities of defects in the i-layer contributing to the space charge. Any increase in density of these defects leads to larger V_n and V_p, which then reduces the carrier injection. The contributions to the divergence between J_{SC}-V_{OC} and J_D-V due to the densities of gap states in the i-layer have been confirmed by introducing light induced defects.

Although the presence of the potential barrier V_n and V_p has little effect on V_{OC}, it can have deleterious effect on FF. This is because, as have been discussed above, the presence of these barriers lowers the average electric filed across the bulk and thus reduces the collection efficiency of the photo-generated carriers. This points to a important fact that FF is not merely determined by the defect density in the bulk but also affected by V_n and V_p. Consequently, FF is in general not a parameter directly corresponding to the defect density, so when FF has to be used as a parameter to study the density of defects in the bulk i-layers, it is necessary to make sure that the contributions from V_n and V_p is negligible.

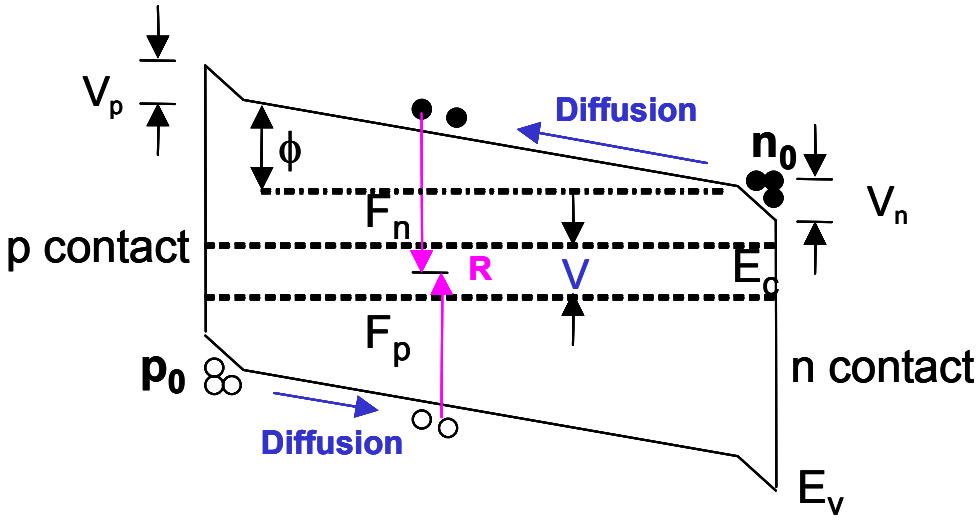


Figure A.1: Schematic band diagram for i-layer of p-i-n cells under forward bias in the dark

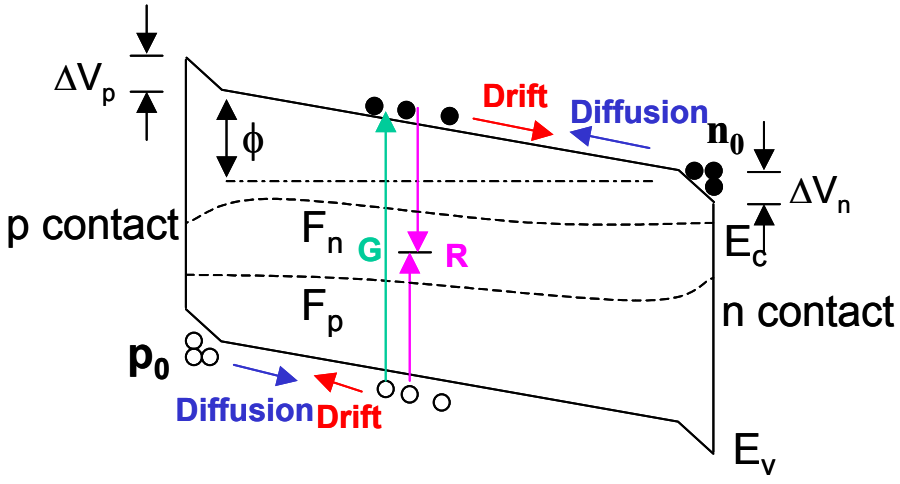


Figure A.2: Schematic band diagram for i-layer of p-i-n cells under forward bias and illumination.

List of Publications

1. J. M. Pearce, J. Deng, R. W. Collins, and C. R. Wronski, "Light Induced Defect States in Hydrogenated Amorphous Silicon Centered Around 1.05 and 1.2eV from the Conduction Band Edge", *Applied Physics Letters*, 83(18), pp. 3725-3727, 2003.

2. C. R. Wronski, J. M. Pearce, J. Deng, V. Vlahos, and R. W. Collins, "Intrinsic and Light Induced Gap States in a-Si:H Materials and Solar Cells Effects of Microstructure", *Thin Solid Films*, 2003 (in press).

3. J. Deng, J. M. Pearce, R. J. Koval, V. Vlahos, R.W. Collins, and C. R. Wronski, "Absence of carrier recombination associated with the defect pool model in a-Si:H i-layers: Evidence from current-voltage characteristics on p-i-n and n-i-p solar cells", *Appl. Phys. Lett*. 82(18), pp. 3023-3025, 2003.

4. J. Deng, J. M. Pearce, V. Vlahos, R. W. Collins, and C. R. Wronski, "Carrier Transport and Recombination in a-Si:H p-i-n Solar Cells in Dark and Under Illumination", *Mat. Res. Soc. Proc.* 762, A3.4, 2003.

5. V. Vlahos, J. Deng, J. M. Pearce, R. J. Koval, R. W. Collins and C. R. Wronski, "Recombination in n-i-p (substrate) a-Si:H Solar Cells with Silicon Carbide and Protocrystalline p-layers", *Mat. Res. Soc. Proc.* 762*,* A7.2, 2003.

6. G.M. Ferreira, R.J. Koval, J.M. Pearce, R. W. Collins, and C. R. Wronski, "Optimization of Silicon p-type Layers for Amorphous Silicon n-i-p Solar Cells", *Journal of Non-Crystalline Solids* (in press).

7. A. S. Ferlauto, G. M. Ferreira, J. M. Pearce, C. R. Wronski, and R. W. Collins, "Analytical Model for the Optical Functions of Amorphous Semiconductors and Its Applications in Thin Film Photovoltaics", *Thin Solid Films* (in press).

8. A.S. Ferlauto, G.M. Ferreira, R.J. Koval, J. M. Pearce, C.R. Wronski, and R.W. Collins, "Evolution of Crystallinity in Mixed-phase (a+c)-Si:H as Determined by Real Time Ellipsometry", *Mat. Res. Soc. Proc.* 762, A5.10, 2003.

9. G. M. Ferreira, A. S. Ferlauto, R. J. Koval, J. M. Pearce, C. R. Wronski, R. W. Collins, M. M. Al-Jassim, and K. M. Jones, "Evaluation of Compositional Depth Profiles in Mixed Phase (Amorphous + Crystalline) Silicon Films from Real Time Spectroscopic Ellipsometry" *Thin Solid Films* (under review).

10. R.W. Collins, A.S. Ferlauto, G.M. Ferreira, J. Koh, C. Chen, R.J. Koval, J.M. Pearce, C.R. Wronski, M.M. Al-Jassim, and K.M. Jones, "Application of Deposition Phase Diagrams for the Optimization of a-Si:H-Based Materials and Solar Cells" *Mat. Res. Soc. Proc.,762,* A10.1, 2003.

11. R.W. Collins, A.S. Ferlauto, G.M. Ferreira, C. Chen, R.J. Koval, J.M. Pearce, and C.R. Wronski, "Kinetics of Silicon Film Growth and the Deposition Phase Diagram", *Journal of Non-Crystalline Solids* (in press).

12. R.W. Collins, A.S. Ferlauto, G.M. Ferreira, C. Chen, J. Koh, R.J. Koval, Y. Lee, J.M. Pearce, and C. R. Wronski, "Evolution of microstructure and phase in amorphous, protocrystalline, and microcrystalline silicon studied by real time spectroscopic ellipsometry", *Solar Energy Materials and Solar Cells*, 78(1-4), pp. 143-180, 2003.

13. J. M. Pearce, J. Deng, V. Vlahos, R. W. Collins, and C. R. Wronski, "Light Induced Changes in Two Distinct Defect States At and Below Midgap in a-Si:H", *Proceedings of the 3rd World Conference on Photovoltaic Energy Conversion*, (in press).

14. C. R. Wronski, R. W. Collins, J. M. Pearce, J. Deng, V. Vlahos, G. M. Ferreira, and C. Chen, "Optimization of Phase-Engineered a-Si:H-Based Multijunction Solar Cells", *National Center for Photovoltaics Program Review and Solar Program Proceedings*, February 2003, NREL/CD-520-33586 pp. 789-792.

15. R. W. Collins, G.M. Ferreira, J. M. Pearce, A. S. Ferlauto, R. J. Koval, and C. R. Wronski, "Real Time Optics of the Growth of Silicon Thin Films in Photovoltaics: Analysis of the Amorphous-to-Microcrystalline Phase Transition", *National Center for Photovoltaics Program Review and Solar Program Proceedings*, February 2003, NREL/CD-520-33586 pp. 772-775.

16. R. W. Collins, G. M. Ferreira, A. S. Ferlauto, R. J. Koval, J. M. Pearce, C. R. Wronski, M. M. Al-Jassim, and K. M. Jones, "Thickness evolution of the microstructure of Si:H films in the amorphous-to-microcrystalline phase transition", *Proceedings of the 3rd World Conference on Photovoltaic Energy Conversion*, (in press).

REPORT DOCUMENTATION PAGE

Form Approved
OMB No. 0704-0188

The public reporting burden for this collection of information is estimated to average 1 hour per response, including the time for reviewing instructions, searching existing data sources, gathering and maintaining the data needed, and completing and reviewing the collection of information. Send comments regarding this burden estimate or any other aspect of this collection of information, including suggestions for reducing the burden, to Department of Defense, Executive Services and Communications Directorate (0704-0188). Respondents should be aware that notwithstanding any other provision of law, no person shall be subject to any penalty for failing to comply with a collection of information if it does not display a currently valid OMB control number.

PLEASE DO NOT RETURN YOUR FORM TO THE ABOVE ORGANIZATION.

1. REPORT DATE *(DD-MM-YYYY)*	2. REPORT TYPE	3. DATES COVERED *(From - To)*
August 2004	Subcontract Report	January 2003 – January 2004

4. TITLE AND SUBTITLE
Optimization of Phase-Engineered a-Si:H-Based Multijunction Solar Cells: Second Annual Technical Report, January 2003 – January 2004

5a. CONTRACT NUMBER
DE-AC36-99-GO10337

5b. GRANT NUMBER

5c. PROGRAM ELEMENT NUMBER

6. AUTHOR(S)
C.R. Wronski, R.W. Collins, V. Vlahos, J.M. Pearce, J. Deng, M. Albert, G.M. Ferreira, and C. Chen

5d. PROJECT NUMBER
NREL/SR-520-36695

5e. TASK NUMBER
PVP45001

5f. WORK UNIT NUMBER

7. PERFORMING ORGANIZATION NAME(S) AND ADDRESS(ES)
Center for Thin Film Devices
The Pennsylvania State University
University Park, PA 16802

8. PERFORMING ORGANIZATION REPORT NUMBER
NDJ-2-30630-01

9. SPONSORING/MONITORING AGENCY NAME(S) AND ADDRESS(ES)
National Renewable Energy Laboratory
1617 Cole Blvd.
Golden, CO 80401-3393

10. SPONSOR/MONITOR'S ACRONYM(S)
NREL

11. SPONSORING/MONITORING AGENCY REPORT NUMBER
NREL/SR-520-36695

12. DISTRIBUTION AVAILABILITY STATEMENT
National Technical Information Service
U.S. Department of Commerce
5285 Port Royal Road
Springfield, VA 22161

13. SUPPLEMENTARY NOTES
NREL Technical Monitor: B. von Roedern

14. ABSTRACT *(Maximum 200 Words)*

This subcontract report entails investigation of engineering improvements in the performance and stability of solar cells in a *systematic* way. It consists of the following four tasks: Task 1—Materials research and device development; Task 2—Process improvement directed by real-time diagnostics; Task 3—Device loss mechanisms; and Task 4—Characterization strategies for advanced materials. The real-time spectroscopic ellipsometry (RTSE) multichamber is near completion, and trial depositions with a-Si:H will begin shortly. Construction of the new dual beam photoconductivity (DBP) apparatus has been completed, and the new capabilities are being used in studies on a-Si:H thin films. A new apparatus is being constructed for in-depth studies on the mechanisms limiting the performance of a-Si:H solar cells and the two track studies (cells and films) of the Staebler-Wronski Effect. The capabilities include the ability to integrate the cell characteristics including the quantum efficiency, at different temperatures on both p-i-n and n-i-p solar cells.

15. SUBJECT TERMS
PV; solar cells; device; real-time spectroscopic ellipsometry (RTSE); dual-beam photoconductivity (DBP); thermal annealing; crystalline; current-voltage; differential diode quality factor; quasi-Fermi splitting; light-induced; photocurrent; density

16. SECURITY CLASSIFICATION OF:			17. LIMITATION OF ABSTRACT	18. NUMBER OF PAGES	19a. NAME OF RESPONSIBLE PERSON
a. REPORT	b. ABSTRACT	c. THIS PAGE			
Unclassified	Unclassified	Unclassified	UL		19b. TELEPONE NUMBER (*Include area code)*